Search for short range new interactions in the submicron range by coherent neutron scattering using V nanoparticle target

September, 2025

Masayuki Hiromoto

A thesis presented for the degree of

Doctor of Philosophy

大阪大学
THE UNIVERSITY OF OSAKA

Department of Physics

Graduate School of Science

The University of Osaka

Supervisor: Prof. Tatsushi Shima

Abstract

Name of the student: **Masayuki Hiromoto**

Degree for which submitted: **PhD**

Department: **Department of Physics, The University of Osaka**

Thesis title: **Search for short range new interactions in the submicron range by coherent neutron scattering using V nanoparticle target**

Thesis supervisors: **Tatushi Shima**

Month and year of thesis submission: **September 2025**

Among the four fundamental interactions in nature, all except gravity are described by the theoretical framework of particle physics known as the Standard Model. In recent years, various extended models that aim to encompass all interactions, including gravity, referred to as Beyond the Standard Model (BSM) physics have been actively studied. Those models often predict unknown interactions akin to gravity through the introduction of new gauge bosons. Experimental tests of such theories involve searching for deviations from the inverse-square law of gravity over various ranges of interaction distances. However, at submicron scales, experimental investigations have been significantly hindered by electromagnetic backgrounds such as van der Waals forces, making it challenging to probe the parameter space predicted by BSM theories.

To address this, we previously conducted small-angle neutron scattering (SANS) experiments using neutrons, which are insensitive to electrostatic forces, and Xe gas atoms. By precisely measuring the angular distribution of scattered neutrons, we successfully placed experimental constraints on unknown interactions at submicron scales. Although the sensitivity limit of this experiment has been improved through subsequent precise measurements using neutron interferometry, the sensitivity is still insufficient by 5 to 6 orders

of magnitude to fully test BSM theories.

In this study, I developed a new experimental method using nanoparticles as targets, which have a size comparable to the submicron scale, instead of Xe gas atoms. With nanoparticle targets, the scattering waves from the many atoms within a single particle undergo coherent scattering, resulting in an amplification effect proportional to the mass of the target particle. For nanoparticles, this sensitivity enhancement factor can reach several million times, promising significant improvement in sensitivity to unknown interactions. This experiment was conducted at J-PARC/MLF/BL05.

The target material was primarily composed of vanadium metal, an element with an extremely small coherent nuclear scattering length, to reduce background from nuclear scattering. Furthermore, to create nanoparticles with near-zero coherent nuclear scattering length, we prepared V-Ni alloy nanoparticles by mixing nickel with vanadium in a ratio that cancels out vanadium coherent nuclear scattering length, using the RF thermal plasma method. Electron microscopy (FE-SEM) confirmed that the synthesized nanoparticles were spherical with a diameter of approximately 40 nm. Composition analysis revealed that these nanoparticles were more uniform and of higher purity than commercially available vanadium nanoparticles. The primary impurity element was oxygen, and improvements in raw materials allowed us to reduce oxidation. We successfully synthesized vanadium nanoparticles with the highest purity among our samples (coherent nuclear scattering length: 0.719 ± 0.023 fm).

Using these target samples, we performed SANS measurements with the pulsed neutron source at the Japan Proton Accelerator Research Complex (J-PARC). To analyze the momentum transfer distribution obtained from the experiments in detail, we also performed small-angle X-ray scattering (SAXS) measurements to determine the particle size distribution of the nanoparticles used as targets. By comparing these data with simulations based on the composition analysis results, we searched for deviations in the momentum transfer distribution caused by unknown short-range forces. The preliminary result on the upper limits on unknown short-range forces suggests significant improvement of the sensitivity of the new exploration method compared to the previously achieved one using the neutron scattering method in the region of $\lambda_{\mathrm{B}} = 2 \sim 10$ nm.

Acknowledgements

First and foremost, I would like to express my deepest gratitude to my supervisor, Prof. Tatsushi Shima. It has been a great pleasure and honor for me to have been able to conduct research together with him for the eight years since I joined to the Research Center for Nuclear Physics (RCNP). I am very grateful to him for giving me the opportunity to try new experiments in fundamental physics research using neutrons.

I am deeply grateful Prof. Kenji Mishima, who is the person-in-charge of the J-PARC MLF/BL05 experimental instrument for giving me many opportunities to participate in experiments and providing me with many discussions and advice on physics.

I would like to address my thanks to all the members of the J-PARC NOP collaboration. In particular, I am grateful to Dr. Christopher C. Haddock, Prof. Masaaki Kitaguchi, Mr. Ryota Kondo, Dr. Rintaro Nakabe, Prof. Hirohiko Shimizu, Prof. W.Michael Snow, Mr. Yuki Yoshikawa, Prof. Tamaki Yoshioka and Prof. Albert Young for their helps. Their contribution of discussion of data, experimental preparation, and advice is very significant and without which the success of this work would be impossible.

I would like to express my supreme gratitude to Prof. Hiroyasu Ejiri for his generous support and for giving me the opportunity to present this research internationally through the support by the Nogami fund.

I would like to thank Dr. Masato Tamura (RCNP, The University of Osaka), Mr. Yoshifumi Sakai from Nisshin enfeneering Co. Ltd., and Mr. Nobuo Tukihara from Aishin Nano Technologies Co. Ltd. for their assistance with the target prototype experiments.

Besides, I would like to express my sincere gratitude to Tech. Staff. Nao Eguchi and Yosuke Murakami from Institute of Scientific and Industrial Research in Osaka university. for your invaluable assistance in the sample analysis process and measurements.

Additionally, I would like to express my sincere gratitude to my family, friends, and everyone who has always supported me in times of need. I am deeply grateful to you all. I would also like to express my deep gratitude to my late father, who gave me so much encouragement and support while he was alive, and who served as a model for how I should live my life.

Last but not least, I have been supported by many people during a doctoral course. I am truly grateful.

Contents

List of Figures

List of Tables

Dedicated to family.

Chapter 1

Introduction

The Standard Model (SM) in particle physics describes physics phenomena acting on microscopic systems by means of a gauge theory, and the results are consistent with the results that have been experimentally obtained.

The SM framework also appears to be successful due to the existence of the Higgs particle discovered at the LHC(Large Hadron Collider)in 2012 [12]. The three fundamental interactions in nature: strong, weak, and electromagnetic interactions are explained in a unified way by the SM, and the gravity is the exception, whose classical theory is given by the General Relativity (GR).

The wave nature of gravity predicted by the GR in 1916 was confirmed by the observation of a gravitational wave by the American LIGO(Laser Interferometer Gravitational Wave Observatory) in 2016, almost 100 years later [13].

However, SM have failed to address the issues of dark energy which introduces the accelerated expansion of the universe, the cosmological constant problem, the weakness of gravity (the "hierarchy" problem), and the asymmetry between matter and antimatter observed in the universe. The theoretical models extended to account for those problems are called the Beyond Standard Model(BSM)s.

We first review the framework of some major BSMs and the current status of experimental search in the world for BSM in the following in Chapter 1.

1.1 BSM(Beyond Standard Model)

Of all the proposed extensions to SM, supersymmetric (SUSY) models are considered the most promising candidate. SUSY requires that symmetry exists between fermions and bosons, and among the quantum corrections related to the vacuum expectation value of the Higgs field, the contributions of fermions and bosons cancel each other out, so the Higgs boson's mass remains close to zero. In this theory, new particles with the spins shifted by 1/2 are introduced to explain the quantum correction that causes a difference of several tens of orders of magnitude between the Planck scale ($10^{19}\,\mathrm{GeV} : l_p = 10^{-35}\,\mathrm{m}$) and the electroweak scale ($246\,\mathrm{GeV} : l_{em} = 10^{-17}\,\mathrm{m}$), which describe the coupling constant between weak interactions and gravity. Specifically, the t and $\bar{\mathrm{t}}$ loops cancel each other out, spontaneously breaking the symmetry, and eventually naturally creating an electroweak scale. Expermintal signatures for SUSY are predicted by many to exist at energy scales achievable in modern particle colliders. Up to now, all experimental tests of SUSY at the LHC have produced null results at center of mass (COM) collision energies of up to 13 TeV [14]. At the time of writing this paper, no supersymmetric particles have been found, and search experiments will resume from 2022 with a COM energy of 13.6 TeV, potentially providing evidence of SUSY in the near future.

Given the current situation where SUSY particles have not been discovered, it will be important to consider physical theories alternative to SUSY. Most of the proposals based on SUSY and string theory predict new particles on the TeV scale. However, there are many phenomena that can be predicted from the existence of fundamental physics at the sub-eV scale. For example, some theories predict the existence of hidden sectors of particles that have only very weak interactions with standard model particles in the visible sectors. Physics on this energy scale is not suitable for exploration through high-energy experiments such as the LHC.

String theory is another popular extension to the SM. In string theory the fundamental constituents of matter are not point like particles as in case of the SM but rather 1D objects whose excitation gives rise to different particle masses. In this framework a spin 2 particle arises naturally as closed strings and can be attributed to the graviton as the gravitational field is known to be a tensor field with the rank 2 [15].
In the next chapter, we will discuss concrete examples of predicted physics at the sub-eV scale and the unknown interaction potentials involved in the exploration in this experiment.

1.2 New Finite-range Forces Predicted at Low Energy Scales

Since SM describes interactions between elementary particles in terms of boson exchange, additional U(1) symmetries naturally appear in theoretical attempts to describe such BSM phenomena. In general, when a new interaction term is added to the SM Lagrangian in efforts to explain BSM physics the term must contain certain symmetry properties or else the Lagrangian as a whole loses its physical meaning. In retaining these symmetry properties, a gauge boson is often introduced, whose mass m_b is determined by the characteristic length of the new interaction $\lambda_c = \frac{\hbar}{m_b c} \frac{0.197\text{eV}\times\mu\text{m}}{m_b c^2}$.

One way to generate such new forces in the supersymmetric extension of SM is to use the baryon number (B) or baryon number minus lepton number (B − L) as the charge[1-4]. The gauge boson associating the additional U(1) symmetry with B or B-L is generally mixed with the Z bosons, yielding a force proportional to the combination of baryon number, lepton number, and hypercharge.

Some of these new particle candidates (Axions, ALPs (Axion-Like Partcies), hidden U(1) gauge particles) have masses in the sub-eV range and can be very light. In recent theoretical studies, it is commonly known as WISP (Weakly-Interacting sub-eV Particles) [16]. These can create new interactions at reachable distances on the order of picometers to millimeters. There are other grounds for studying such sub-eV scale physical phenomena. An example of this is that the mass of a neutrino is less than 2.2 meV, and that the energy density of the vacuum of space is estimated from observations to be on the scale of approximately $\rho_\Lambda = 25\,\text{meV}^4$ (cosmological constant problem). For example, new bosons are predicted in most of the Grand Unified Theories that incorporate SM with relative strength of the coupling $O(0.1)$. These strongly bound bosons would have to be heavier than 1 TeV to be consistent with current observations. Heavier bosons are searched for at the Large Hadron Collider. However, lighter bosons could have gone unnoticed as long as they only weakly interact with matter. Such bosons mediate a finite-range force between two fermions. Alternatively, new finite-range forces may appear in some compact extra-dimensional models, for example due to messenger fields that exist in most of such extra dimensions. The mathematical success of one of the best-known theories postulating extra dimensions, the so-called string theory (M-theory), shows that a theory of gravity consistent with quantum mechanics and other known interactions is possible, but so far there is no direct experimental test of this theory.

One of the remarkable feature of the gravity is the fact that it follows an inverse square law (ISL) famously known as “Newton’s law of universal gravitation.” This law can be

derived within GR in the non-relativistic limit in a weak gravitational field. Its validity has been verified both at cosmological scales, where it theoretically explains complex motions of satellites such as orbital motion and precession due to celestial perturbations, and at short distance scales, where it has been experimentally verified down to distances of less than 1 mm [17]. In quantum theory, the mass of the graviton that transmits the interaction is zero, but the analysis of GW170104 measured by LIGO in 2017[18] reported that the Compton wavelength λ_c of the graviton is greater than 1.5×10^{16} m based on the observation of gravitational waves from the merger of black hole binaries. This is equivalent to $7.7 \times 10^{-23}\,\mathrm{eV/c^2} > m_b$ in mass, therefore a stringent upper limit on the mass. So, the gravitational interaction is experimentally confirmed to be consistent with the ISL at regime of the distance longer than a few mm. However, the nature of gravity at short distances is still not fully verified from an experimental point of view: many alternative theories of gravity only extend to short ranges because they have an additional component of the gravitational interaction that involves the exchange of exotic particles, and several other theories that try to explain the so-called hierarchy problem also add modifications as short-range forces[16].

1.3 Probing BSM Physics with Low-energy Neutron

Low-energy neutrons are useful probes to explore various types of short-range interactions described in the previous Sec. 1.2. Research reactors and accelerator-driven neutron sources provide intensive low-energy neutrons which enable one to make high-precision experiments for fundamental science as well as for engineering Since neutrons have no charge, they can pass through bulk material with little attenuation. Furthermore, their momentum transfer corresponds to the scale of pm $\sim$ μm, making them a probe of new possible interactions on length scales of interest. The properties of neutrons are shown in Table 1.1.

Table 1.1: Properties of Neutrons [8], [9]

Physical Quantity	Simbol	Value
Neutron mass	m_{n}	$939.56542052(54)\,\mathrm{MeV/c^2}$
Electric charge	q_{n}	$(-0.2 \pm 0.8) \pm 10^{-21}\,\mathrm{e}$
Magnetic moment	μ_{N}	$-9.6623651(23)\,\mathrm{J/T}$
Electric polarizability	α_0	$12.5(2.5) \times 10^{-4}\,\mathrm{fm^3}$

As shown in Table 1.1, neutrons have finite rest mass and are electrically neutral, so the electromagnetic background effects are suppressed at least at the lowest order. This is essentially important for experimental searches for violation of ISL at the distance shorter than a few μm. Namely, previous experiment have been performed based on the same experimental principle as the Cavendish's experiment which measures the tiny gravitational force appearing between two test objects separated with a certain distance. However, as the distance becomes shorter, the intermolecular force, or the Van der Waals force between those objects becomes rapidly strong and becomes serious background against new gravity-like forces. The potential of the intermolecular forces acting between electrically neutral normal atoms and molecules can be calculated using Eq. (1.1), which is proportional to the product of the electric polarizabilities of the objects. In the measurement using neutron as one of the two test objects, since the polarizability of neutron is 10^{-18} times smaller than that of atoms or molecules, so the effects of the Van der Waals force can be suppressed by 18 orders of magnitude, leading to high signal-to-noise ratio in the experimental search for violation of ISL.

$$U(r) = -\frac{3\hbar c}{8\pi}\frac{\alpha_0}{r^4} \tag{1.1}$$

Of course, it is difficult to replace one of the two test objects with a neutron because it is almost impossible to make neutrons at rest. Therefore, instead, we employ the method of the small-angle neutron scattering (SANS). In the case of SANS, the Yukawa-like potential of the new gravity-like interaction is detected as its Fourier transform, i.e. the form factor of the target potential [19, 20]. Based on this principle, several experiments by means of low-energy neutrons have been performed to search for unknown interactions at the submicron scale that are hypothesized to be due to the existence of very light bosons and extra dimensions introduced in the previous Sec. 1.2 [21]. Nesvizhevsky et al. [21] reanalyzed existing data of neutron scattering experiments that were originally performed for other purposes and constrained such unknown interactions. It has also been shown that, taking advantage of its spin degree of freedom and the fact that it can be polarized with high efficiency, it is a useful probe for spin-dependent interactions at the mesoscopic scale [22]. For example, measurements of the neutron optical activity in liquid ^{4}He have been used to set upper limits for the parity odd neutron-nuclear interaction of the form $\vec{\sigma}\vec{p}$, where $\vec{\sigma}$ is the neutron spin vector and $\vec{p}$ is the momentum vector of the ^{4}He nucleus. The present work is focused on experimental search for unknown intermediate-range "gravity-like" interactions, i.e. the interactions mediated by the exchange of neutral spin-less bosons, like Nesvizhevsky's study. Such a boson allows the finite range force between two fermions given in the form

$$V_5(r) = -\frac{g^2 Q_1 Q_2}{4\pi r} \exp(-r/\lambda_{\mathrm{B}}) \tag{1.2}$$

with Q_1, Q_2 is the combined charge of the two interacting test masses, separated by r, with g the coupling to the new force mediator and $\lambda_{\mathrm{B}} = \hbar/\mu c$ is the reduced Compton wavelength of the particle (μ is the mass of the scalar boson mediating the interaction). In this study, Q_1, Q_2 are the charges of the two interacting test masses, but in this study they are taken to be masses rather than baryon numbers B. Since these new forces act as short-range corrections to gravity, we parameterize the strength of the new forces by their ratio to gravity, $\alpha = g^2 m_{\mathrm{pl}}^2/(4\pi)$, where m_{pl} is the Planck mass.

The constraints on this modified Yukawa potential have been experimentally explored from the solar system scale (satellite orbit analysis, etc.) to the elementary particle scale by collider experiments. Figure 1.1 shows the region excluded by the experimental constraints with 95% confidence for the case with submicron-scale interaction lengths. As of 2024, the tightest constraints on the hypothetical Yukawa-type terms in the submicron-scale gravitational potential were obtained by Heacock et al. by precisely measuring the structure factor of a silicon single crystal using Pendellösung interferometry [23].

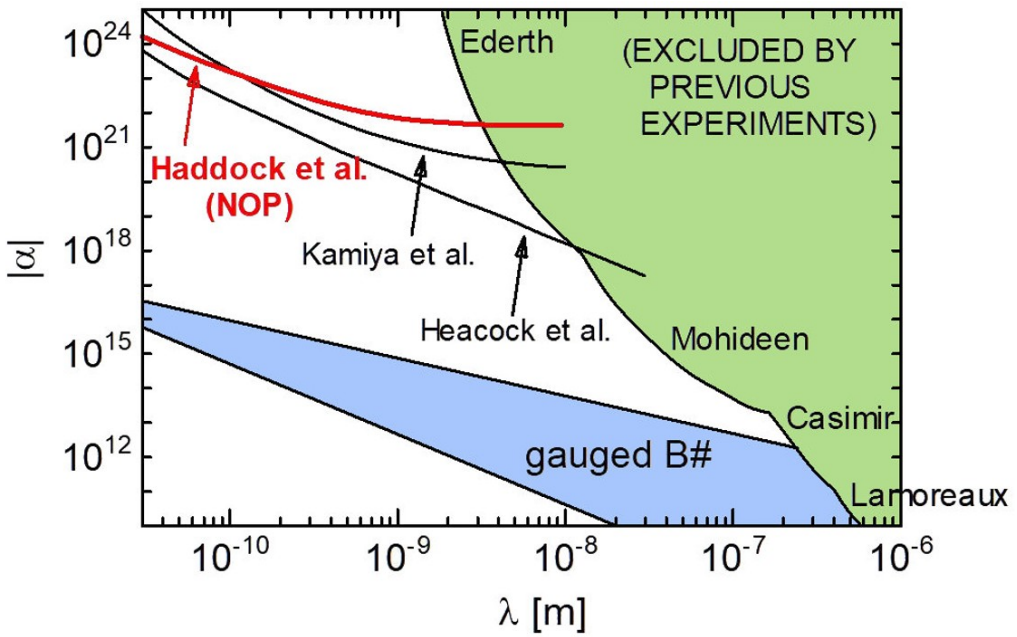

Figure 1.1: Experimental constraints on the submicron-scale Yukawa interaction.(blue area) gauge baryon number model [1], (green area) regions excluded by previous experiments

The search results by Kamiya and our collaborator Haddock shown in Fig. 1.1 are both the results of neutron scattering experiments using noble gas as the target [24, 25]. Searches in this area have not been explored sufficiently compared to more macroscopic regions. For exploration of the submicron region, there is a theoretical prediction of the gauged baryon number model [1], which follows the ADD model proposed by Dimopoulos et al.[26], but the experimental sensitivity is insufficient to probe it. The gauged baryon number model assumes that gauge particles other than gravity can propagate not only in three dimensions but also in the bulk (fourth dimension plus extra dimensions), and the ratio of gauge field to gravity is given as follows when the four-dimensional gauge coupling is g_4^2.

$$\alpha_{\mathrm{g}} = \frac{F_{\mathrm{gauge}}}{F_{\mathrm{G}}} \frac{1}{G_{\mathrm{N}} m_{\mathrm{p}}^2} \tag{1.3}$$

where m_{p} is the proton rest mass. When we consider that the gauge bosons which can propagate through the bulk, the volume of the extra n-dimensions is expanded as follows

$$\frac{1}{g_4^2} = \frac{V_d}{g_{(4+\mathrm{n})}^2} \tag{1.4}$$

As a result, gravity in the bulk becomes overwhelmingly stronger than that in four-dimensional space, and we predict that the gauge force will also become larger through the same mechanism, resulting in unknown interactions on the submicron scale. In the search experiments conducted so far, the experimental sensitivity is insufficient by two to three orders of magnitude to verify the region predicted by theories based on a new bosons in large extra dimensions [1] on the submicron scale, so it is necessary to further increase the search sensitivity. Therefore, in the next chapter of this paper, we will explain a method to further increase the sensitivity using neutron coherent scattering techniques.

1.4 Phenomenological Approach

The purpose of this paper is to describe an experiment that became sensitive to the effects of possible short-range interactions independent of the spin, depending on relative velocity, and relative position between fermions mediated by a single spinless boson, leading to the introduction of a Yukawa-type potential as described in the previous Sec. 1.3.

A phenomenological explanation of the origin of the additional Yukawa-type potential provides insights into this new field, including the search for possible long-range phenomena. To derive the long-range force between two fermions of masses m and m' mediated by a very light particle as shown in Fig. 1.2 [2], we consider a generalized interaction mediated by a single spinless boson of mass m_0.

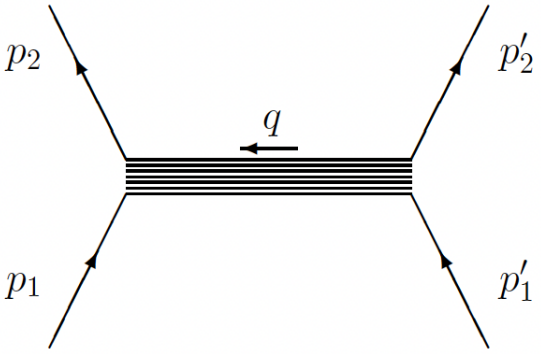

Figure 1.2: Elastic scattering of two fermions mediated by some very light particles represented generically by the horizontal blob of four-momentum q [2].

This amplitude is a scalar invariant formed from the three momenta of the incoming and outgoing fermions, $\overrightarrow{p_1}$, $\overrightarrow{p'_1}$ and $\overrightarrow{p_2}$, $\overrightarrow{p'_2}$, and the spin vectors of the two fermions, $\overrightarrow{\sigma}$ and $\overrightarrow{\sigma'}$. We want to know all possible long-range force forms that can be derived from this

picture so that we can design appropriate experiments to isolate possible new spin-1 boson exchanges. To do this, we need to construct non-relativistic scattering amplitudes using scalar invariants formed from the spins and momenta of the fermions. All possible linearly independent scalars have been identified for this interaction [2]. There are 16 such scalars in total: 1 is spin-independent, 6 involve the spin of one fermion, and the remaining 9 depend on both fermion spins. Of these 16 operators, 10 depend on the relative momentum of the fermions. The operator of interest here is the spin-independent term, identified in the literature as $\mathcal{O}_1 = 1$. The general scattering amplitude in momentum transfer space is given by

$$\mathcal{A}(\vec{q},\vec{p}) = \mathcal{P}(\vec{q}^2)\sum_{i=1}^{16}\mathcal{O}_i(\vec{q},\vec{P})f_i(\vec{q^2}/m^2,\vec{P}^2/m^2) \tag{1.5}$$

where $f_i(\vec{q^2}/m^2,\vec{P}^2/m^2)$ is a dimensionless scalar function, $\vec{q}\equiv\vec{p_2}-\vec{p_1}$ is the momentum transferred to the fermion mass m, and $\vec{P}\equiv\frac{1}{2}(\vec{p_1}+\vec{p_2})$ is the average momentum of that fermion. Taking a Fourier transform gives us the interaction potential in terms of the spatial coordinate.

$$V(\vec{r},\vec{v}) = -\int\frac{d^3q}{(2\pi)^2}\exp(i\vec{q}\cdot\vec{r})A(\vec{q},m\vec{v}) \tag{1.6}$$

Also, as in experiments looking for new macroscopic forces, we exploit the fact that the scalar functions $f_i(\vec{q^2}/m^2,\vec{P}^2/m^2)$ are independent of both $\vec{q^2}$ and $\vec{P^2}$ in the non-relativistic limit.

$$V(\vec{r},\vec{v})_1 = -\int\frac{d^3q}{(2\pi)^2}\exp(i\vec{q}\cdot\vec{r})\mathcal{P}(\vec{q}^2)\mathcal{O}_1 f_1 \tag{1.7}$$

$$\mathcal{P}(\vec{q}^2) = -\frac{1}{\vec{q}^2+m^2}\qquad\text{(standard Lorentz invariant propagator)} \tag{1.8}$$

To simplify the measurement of the strength of this potential, we can simplify Eq. (1.7) as a static potential between nonpolarized objects as follows [27]:

$$V_1(r)\equiv V_5 = f_1^{\mathrm{XY}}\frac{\hbar c}{4\pi r}e^{-r/\lambda_{\mathrm{B}}} \tag{1.9}$$

$$\lambda_{\mathrm{B}} = \frac{\hbar}{m_0 c} \tag{1.10}$$

where XY represent possible fermion pairs, m_0 is the mass of the new boson exchanged. The resulting spin-independent potential is the only potential that is of the well-known Yukawa type and does not depend on the spins of the interacting fermions. The experimental search for such exotic spin-independent interactions has a long history, mostly from the perspective of testing the inverse square law (ISL) of gravity. A common $\alpha{-}\lambda_B$ parameterization found in the literature (Talmadge et al., 1988 [28]) proposes a modified form of the gravitational potential given by

$$V_5(r) = -\frac{Gm_{\mathrm{X}}m_{\mathrm{Y}}}{r}(1+\alpha e^{-r/\lambda_{\mathrm{B}}}) \tag{1.11}$$

where the parameter α represents the strength of the new gravity-like interaction relative to normal Newton's gravity, and λ_{B} the range of the new gravity-like interaction. From the perspective of quantum field theory, such a modification of the gravitational interaction is equivalent to an effect produced by the exchange of a new boson. In the literature, such a Yukawa-like spin-independent interaction is usually called the "fifth force" (Fujii, 1971 [29]; Fischbach et al., 1986 [30]). The correspondence between the two perspectives can be clarified. The exchange of a scalar or vector boson between fermions X and Y can be written as:

$$\alpha = \frac{\hbar c}{4\pi G m_{\mathrm{X}} m_{\mathrm{Y}}}(g_{\mathrm{s}}^{\mathrm{X}} g_{\mathrm{s}}^{\mathrm{Y}} - g_{\nu}^{\mathrm{X}} g_{\nu}^{\mathrm{Y}}) \tag{1.12}$$

Here, $g_{\mathrm{s},\nu}^{\mathrm{X,Y}}$ characterize the vertex-level scalar (subscript s) or vector (subscript ν) couplings that generate the long-range V_5 potential Eq. (1.9), where the range λ_{B} is understood to be the reduced Compton wavelength of the new scalar or vector boson. Equation (1.11) is well suited for phenomenological comparison of various experimental constraints, and theories that drive the search for the ISL violation of gravity and the fifth force are often inspired by the inherent contradictions in general relativity and quantum field theory, such as the proposal by Arkani-Hamed, Dimopoulos, and Dvali (1998, 1999) [26, 31] of extra dimensions compactified to the submicron scale explained in the previous Sec. 1.3, and the existence of dark energy related to the cosmological constant problem.

1.5 Method to Improve the Search Sensitivity

In this section, a new search method using a new technique of coherent neutron scattering is explained. In Sec. 1.5, a method for improving the sensitivity of unknown interactions by applying the principle of coherent scattering is explained. The general description of low-energy neutron scattering and the method of describing the differential cross section using a potential of the scattering system based on the scattering length are explained in the appendix (see Appendix B.1). In Sec. 1.5.1, an expression for scattering due to unknown short-range forces is derived in terms of the scattering length.

1.5.1 Scattering Length due to Unknown Short-Range Forces

Consider the case where there is an unknown short-range potential such as the Eq. (1.11). In the case of low-energy neutron scattering, the scattering amplitude of the unknown neutron interaction is described as follows from the first Born approximation. For detailed calculation methods, please refer to (see Appendix B.1.5)

$$b_{\mathrm{Y}}(q) = -\alpha\left(\frac{2GMm^2}{\hbar^2}\right)\frac{1}{\lambda_B^{-2}+q^2} \tag{1.13}$$

Here M is the mass of the target nucleus, and m is the mass of a neutron. From Eq. (1.13), the scattering amplitude of the unknown short-range force is proportional to the mass of the target. Therefore, the heavier the mass of the target, the greater the scattering probability of the unknown short-range force. For this reason, our collaborator C.C. Haddock conducted a search experiment using a heavier xenon gas target in a neutron scattering experiment [24].

All search experiments using neutrons conducted to date have been search experiments targeting a single atom, regardless of the scattering experiment using noble gas. When competing with other groups using such a search method, the experiment with the better measurement accuracy can place the strictest constraints on the unknown short-range force. Currently, the most stringent constraint on unknown short-range forces has been set by the experiment using neutron interferometers [24], but to verify the region predicted by extra dimensions [32], still more improvement on experimental sensitivity is required, which may be realized with future developments.

Characteristically, the scattering amplitude in Eq. (1.13) depends on q. This differs from the scattering length used to describe the differential cross section of neutron scattering

from nuclear forces, which is expressed as a constant independent of q. The differential cross section of the nuclear force and the unknown short-range force when one neutron is scattered by one nucleus is shown in Eq. (B.33) and Fig. 1.3.

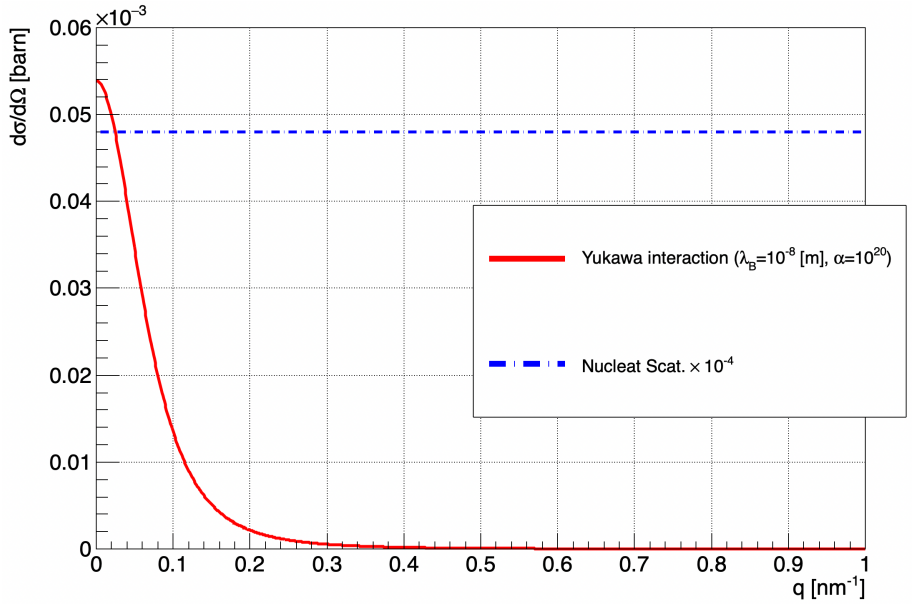

Figure 1.3: Comparison of differential cross sections due to unknown interactions (red line) and nuclear scattering (blue line). The horizontal axis is momentum transfer. Calculations are performed for a Xe target. Nuclear scattering is scaled by a factor of 10^{-4}. Unknown interaction is the calculation result when $\lambda_{\mathrm{B}} = 10^{-8}$ [m] and $\alpha = 10^{20}$.

As an experimental verification method, it can be experimentally verified by analyzing the difference in q dependence between scattering from unknown interactions and nuclear force scattering as shown in Fig. 1.3.

The next Sec. 1.5.2 explains a method for increasing the search sensitivity by using coherent neutron scattering off many atoms.

1.5.2 Coherent Scattering Techniques With Use of Nanoparticle Targets

In order to increase the scattering amplitude of the unknown short-range force, we use a technique based on neutron coherent scattering. In this technique, when the target is composed of many atoms, the scattered waves from individual atoms interfere with each other, thereby increasing the number of atoms that contribute to the scattering of the unknown short-range force. In this case, the potential of the entire scattering system in the presence of the unknown short-range contribution is described as follows from Eq. (B.36).

$$V(r) = \frac{2\pi\hbar^2}{m}\sum_i \left(b_i \delta(r - R_i) + G\frac{\alpha M m}{(r - R_i)} \exp(-(r - R_i)/\lambda_{\mathrm{B}}) \right) \tag{1.14}$$

A recent paper provides a theoretical explanation of how to increase the scattering intensity of unknown interactions in this way [33]. However, our group has been working on preparing experiments using these nanoparticles since 2019 [34].

Next, as shown in Eq. (B.29), if the position distribution of the potential $V(r)$ can be decomposed into the direction of the scattering point and the position dependence of the potential of each scattering point, the cross section can be described by the Fourier transform of the potential. If only the term that contributes to the characteristic coherent scattering shown in the first term of Eq. (B.42) is shown as the differential cross section, the following equation is obtained.

$$\begin{aligned} \frac{d\sigma_{coh}}{d\Omega}(q) &= \left(\frac{m}{2\pi\hbar^2}\right)^2 \left| \int V(r) \exp(iqr) dr \right|^2 \\ &= \left\{ \left(\overline{b_{\mathrm{coh}}} + b_{\mathrm{Y}}(q) \right) \left| \sum_i^n \exp(iq \cdot r_i) \right| \right\}^2 \end{aligned} \tag{1.15}$$

where,

$$b_{\mathrm{Y}}(q) = -\alpha \left(\frac{2GMm^2}{\hbar^2} \right) \frac{1}{\lambda_{\mathrm{B}}^{-2} + q^2} \tag{1.16}$$

$\overline{b_{\mathrm{coh}}}$ is the average value of the coherent nuclear scattering length of multiple atoms contained in the sample. In case the inverse of the momentum transfer in the neutron scattering becomes large, not single but many nuclei become contributing to the scattering coherently, since the phase difference between the waves scattered by different nucleus becomes small. This is the case of the coherent neutron scattering.

Here, the second line represents the gravitational form factor of the target material, which is nothing but the Fourier transform of its mass density distribution. n is the number of nuclei contained in a region whose size is characterized by the inverse of the

momentum transfer. The scattering cross section is enhanced by a factor n^2 compared to the scattering cross section from a single nucleus. Of course, in a real measurement, the number of target particles for a given amount of target material is reduced by a factor n, and the net enhancement factor in the scattering measurement is $n^2/n = n$. It should be noted here that for nanoparticles with diameters of tens of nm, n is as large as 10^6, which is comparable to the range of unknown interactions investigated in this work.

Next, the atomic density contained in the scatterer can be expressed using $\rho_n(r)$, with the scattering length b corresponding to the nuclear scattering and the unknown interaction, as $\rho(r) = \rho_{\mathrm{n}}(r)(\overline{b_{\mathrm{coh}}} + b_{\mathrm{Y}}(q))$. This is generally called the scattering length density. The exponential term in Eq. (1.15) is called the shape factor, and let us consider a nanoparticle of radius R as shown in Fig. 1.4. Based on general diffraction phenomena, from the overview diagram shown on the right of Fig. 1.4 , the path difference between a neutron diffracted by the atomic plane at the bottom and that diffracted by the atomic plane at the top can be expressed as $2d\sin(\theta)$, where d is the atomic plane spacing. Considering

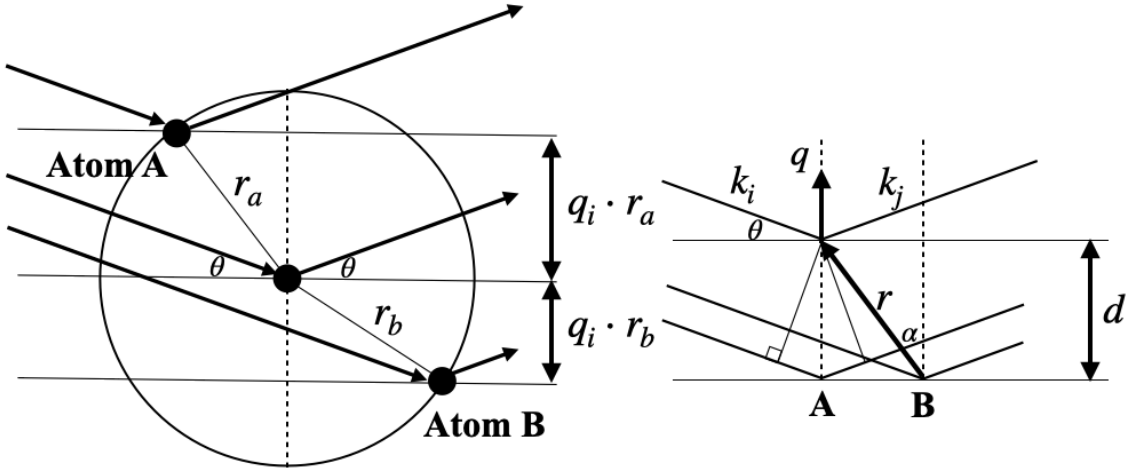

Figure 1.4: The relationship between the path difference of the scattered waves of atom A and atom B in the case of a spherically symmetric particle.r_a and r_b are the distances of atoms A and b from the center of the scatterer. d is the atomic spacing.

a general diffraction phenomenon, the path difference between neutrons diffracted by the upper atomic plane and the lower atomic plane in the schematic diagram shown on the right of Fig. 1.4 can be expressed as $2d\sin(\theta)$, where d is the atomic plane spacing. At this time, d can be expressed as $d = |r|\cos(\alpha) = \vec{q}\cdot\vec{r}$, which is the inner product of the momentum transfer vector q and vector r at a distance r from point B. Next, considering the path difference of scattering by atoms in a particle as shown on the left of Fig. 1.4, when the waves are superimposed for all atoms in the particle, the following equation is

obtained using the scattering length density $\rho(r)$.

$$
\begin{aligned}
F(q) = \sum_{i}^{n} \exp(-iq \cdot r_i) &= \int_0^R \rho(r) \exp(-iq \cdot r) dV \\
&= \rho \int_0^R \int_0^\pi \int_0^{2\pi} \rho(r) \exp(-iqr\cos(\theta)) r^2 dr \sin(\theta) d\theta d\phi \\
&= 4\pi \int_0^R \rho(r) \frac{\sin(qr)}{qr} r^2 dr \\
&= \frac{4\pi\rho}{q} \int_0^R r \sin(qr) dr, \qquad (r < R : \rho(r) = \rho) \\
&= \frac{4\pi\rho}{q} \left\{ -\left[\frac{r}{q} \cos(qr) \right]_0^R + \frac{1}{q} \int_0^R \cos(qr) dr \right\} \\
&= \rho \frac{4\pi R^3}{3} \frac{3[\sin(qR) - qR\cos(qR)]}{(qR)^3}
\end{aligned}
\tag{1.17}
$$

Here, the density is assumed to be constant within a particle of radius R. The Fourier transform of the scattering length density calculated here was obtained as the form factor for spherical particles, but the form of the equation obtained will differ depending on the shape of the particle. The form factor F(q) has a unique q dependence. For this reason, information on the shape and size of the particle is very important when analyzing the q dependence of the Yukawa-type unknown interaction. When performing theoretical calculations, it is necessary to have a good knowledge of these parameters.

1.5.3 Suppression of Coherent Nuclear Scattering

As shown in Eq. (1.15), nuclear scattering is also enhanced by a factor n^2, resulting in a large background for the detection of signals from unknown interactions. The scattering amplitude of coherent scattering is given by the sum of the scattering lengths of the nuclei contained in the coherent region, the size of which is around the reciprocal of the momentum transfer. Therefore, creating a target by mixing different elements or isotopes with opposite signs of the coherent scattering length results in a target with a reduced nuclear scattering cross section. In nature, there are several elements and isotopes that have negative coherent nuclear scattering, such as ^{nat}H (-3.7390 fm), ^{7}Li (-2.22 fm), Ti(-3.438 fm), and V (-0.55 fm). Such techniques to reduce the coherent neutron scattering cross section have already been used in materials science to create sample cells for neutron scattering experiments, and such materials are called "null matrix alloy"[35, 36, 37]. V-Ni alloy is one such commercially available null matrix material.

Next, we will discuss the sensitivity of nanoparticles made from such materials. The differential cross section for coherent nuclear scattering of a spherical particle with a radius of 20 nm is calculated using Eq. (1.17). Figure 1.5 compares natural vanadium and V-Ni alloy nanoparticles containing 5.8 wt.% Ni (10.3 fm).

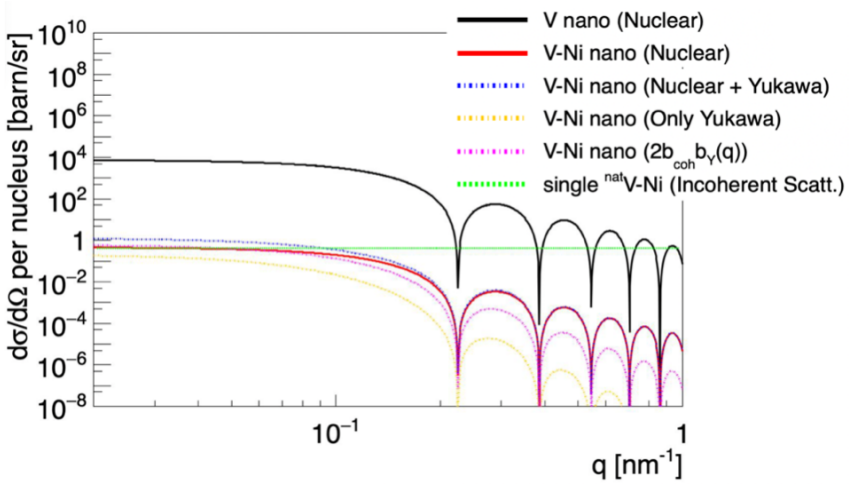

Figure 1.5: Comparison of $d\sigma(q)/d\Omega$ due to coherent nuclear scattering for ^{nat}V and V-Ni alloys. (black line) ^{nat}V with nuclear scattering only, (red line) V-Ni alloy with nuclear scattering only, (blue dotted line) V-Ni alloy with nuclear scattering + Yukawa interaction, (yellow dotted line) V-Ni alloy with Yukawa interaction only, (magenta dotted line) V-Ni alloy with cross-term nuclear scattering and Yukawa interaction, (green dotted line) Incoherent scattering cross section for ^{nat}V

In this case, the differential cross section of the V-Ni alloy nanoparticles is reduced by about three orders of magnitude compared to natural vanadium, resulting in a cross section of the incoherent scattering to similar magnitude. This has the benefit of enabling us to more easily verify deviations from the smaller value of the unknown interaction coupling constant α. Figure 1.6 shows the ratio of the sum of the cross sections for the unknown

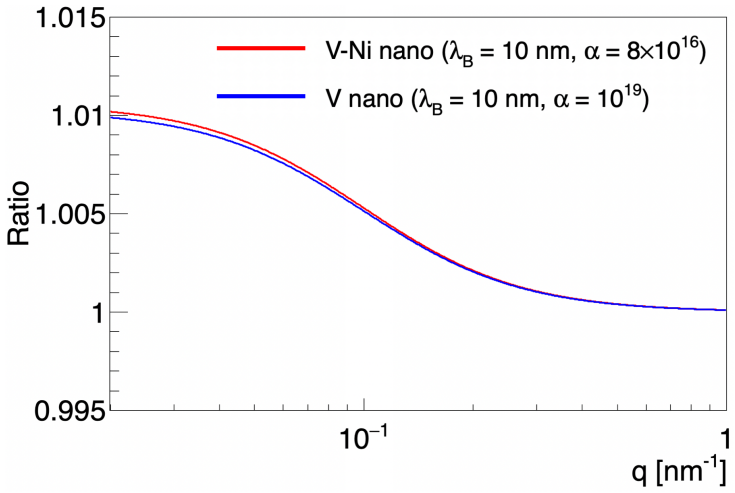

Figure 1.6: The ratio of the differential cross section for coherent nuclear scattering between the nuclear + Yukawa interaction and the nuclear interaction only. For a particle with a radius of 20 nm and $\lambda_B = 10$ nm, the value of α is compared when the ratio is changed by 1 % due to the Yukawa interaction. (blue line) For ^{nat}V, (red line) For a V-Ni alloy.

interaction and nuclear scattering divided by the nuclear scattering cross section. From Fig. 1.6, if the difference in q dependence from unknown interactions can be measured with a verification accuracy of 1 %, comparing the α values when $\lambda_B = 10$ nm, for natural vanadium it is $\alpha = 10^{19}$, and for V-Ni alloy it is $\alpha = 8 \times 10^{16}$, meaning that using V-Ni alloy leads to an improvement in sensitivity of about two orders of magnitude.

In summary, coherent neutron scattering provides a target material with enhanced signals for unknown interactions and reduced nuclear scattering probability, which is the key idea of this study. For these reasons, we adopted nanoparticles made of null matrix alloy as the target material for small-angle neutron scattering to investigate unknown short-range interactions.

Chapter 2

Target Creation

As shown in Sec. 1.5.3, by combining the elements or isotopes with different signs of the coherent scattering length, unnecessary background due to nuclear scattering can be reduced. In this section, we will introduce some of the tests and analysis results to adjust the average coherent nuclear scattering length of a nanoparticle to a small value.

There are two main methods for creating nanomaterials: the break-down method, in which bulk materials consisting of atomic groups are finely processed by mechanical or chemical methods, and the build-up method, in which atoms and molecules are chemically synthesized to create nanoclusters. To create nanoparticles such as those used in this study, it is necessary to mix specific elements in a ratio that makes the coherent nuclear scattering length zero. In an attempt to create such nanoparticles, we conducted test experiments using three methods: chemical precipitation and RF (Radio-Frequency) thermal plasma synthesis as the build-up methods, and jet milling as the break-down method.

The target nanoparticles used in this study were natural vanadium nanoparticles produced by the RF thermal plasma method, as the other two methods could not be used for SANS experiments due to several issues encountered in the production of nanoparticles. The flow of this session will be as follows: firstly, an explanation will be given about the natural vanadium nanoparticles created using the RF thermal plasma method that was adopted as the target, and secondly, the production of the natural vanadium nanoparticles by means of the RF thermal plasma method will be explained. Thirdly, the prototypes created using the chemical synthesis method and the milling method will be shown.

Each of these different methods for creating nanoparticles has its own advantages and disadvantages, and their characteristics are shown in Table 2.1.

Table 2.1: Main methods for producing nanoparticles and their characteristics

Method	Feature	Type
Solid phase method (Milling)	Bulk materials are reduced to nano size through mechanical impact or thermal decomposition. **Advantages:** • Bulk materials with specified ratios can be used. **Disadvantages:** • Equipment contamination. • Metal viscosity may hinder nanoparticle formation.	• Bead mill • Jet mill
Liquid phase method (Chemical precipitation)	Methods for synthesizing nanoparticles using chemical reactions or energy irradiation. **Advantages:** • Stable hydroxides can be produced. • Easy prototype testing. **Disadvantages:** • Size/elemental analysis needed. • Takes time to optimize.	• Sol-gel method • Liquid-phase-reduction
Vapor phase method	Uses chemical reactions or condensation in vapor phase. **Advantages:** • Low contamination. • Mixing ratio control (accuracy: $\sim 0.5\,\mathrm{wt.\%}$). **Disadvantages:** • R&D needed for adjustment. • Oxidation contamination possible.	• Plasma-CVD • RF thermal plasma

2.1 Vanadium Nanoparticle

Vanadium has the smallest coherent nuclear scattering length of all elements, making it one of the best elements to use as a nanoparticle target in this experiment. In the neutron scattering length list provided by NIST up to 2024, the coherent nuclear scattering length for vanadium is $-0.3824(12)$ fm[38]. This value is based on a measurement by the Institut Max von Laue-Paul Langevin (I.L.L.) neutron interferometer in Grenoble published in 1978. Meanwhile, the coherent nuclear scattering length of vanadium was measured at J-PARC/MLF using a new neutron interferometer consisting of an etalon coated with a multilayer neutron mirror. In a paper published in 2023, the new coherent nuclear scattering length of vanadium is $-0.555(30)$ fm[39]. In order to create nanoparticles with suppressed coherent nuclear scattering cross section, it is very important to avoid contaminations by other elements, because they may increases the nuclear scattering cross section.

Usually the contamination in the RF thermal plasma method is smaller than that in other methods such as chemical synthesis Sec. 2.5 and milling Sec. 2.6 method, and the contamination that occurs in the creation process is mainly due to impurity elements contained in the raw materials from the beginning. This feature of the RF thermal plasma method is the key to solve the problems caused by contamination that occurred in the prototype test using the milling method described in the next Sec. 2.6. The RF thermal plasma method is also a suitable method for creating alloy nanoparticles.

In addition to the creation of natural vanadium nanoparticles, this section also explains the results of the prototype production of V-Ni alloy nanoparticles, in which vanadium and nickel are mixed in a ratio giving null coherent nuclear scattering. To create V-Ni alloy nanoparticles, recent coherent nuclear scattering length data for V (-0.555 fm) shows that by mixing Ni, which has a coherent nuclear scattering length of 10.3 fm, with 5.8 wt.%, the average coherent nuclear scattering length becomes 0 ± 0.02 fm.

2.1.1 RF thermal plasma method

Two types of nanoparticles were experimentally created using the RF thermal plasma method: pure vanadium nanoparticles and vanadium-nickel alloy nanoparticles. The production of prototypes using the RF thermal plasma method was commissioned to Nisshin Engineering, Co. Ltd..

The thermal plasma used in this method is the vapor of the material produced by the discharge of RF. In this case not only electrons but also atoms and molecules experience a

high temperature of over 10,000 degrees. The advantage of using thermal plasma is that the process atmosphere can be controlled to a state suitable for material processing.

For example, in addition to argon as an inert gas, an oxidizing atmosphere using air or oxygen, which is useful for organic waste processing, and a reducing atmosphere using hydrogen can be arbitrarily selected. It is also easy to reduce oxygen by using hydrogen as an inert gas. There are three main methods for generating thermal plasma: direct current arc discharge, high frequency induction discharge, and microwave discharge.

The method using Radio frequency (RF) induction discharge used in the nanoparticle creation process is characterized by the fact that thermal plasma is a type of electrodeless discharge, and electrode materials are not mixed into the plasma as impurities. The creation process of the RF thermal plasma method is shown in Fig. 2.1. The entire device

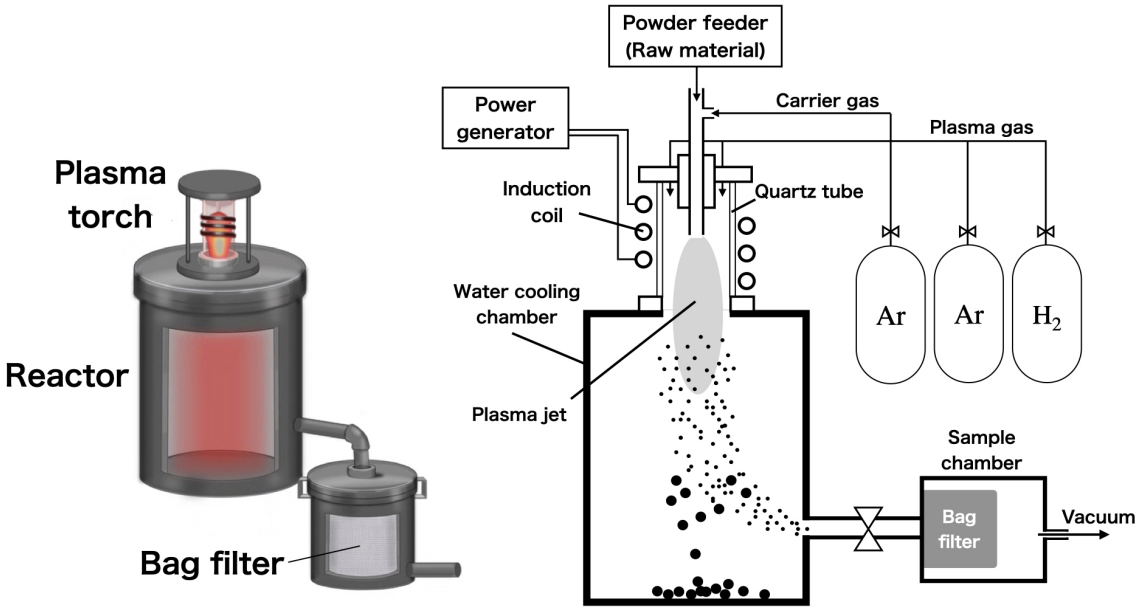

Figure 2.1: Synthesis of nanoparticles by RF thermal plasma method

consists of a RF power supply, a plasma torch, a reactor, and a sample correction filter.

The plasma torch has a solenoid coil (inductive coil) wound around a water-cooled quartz tube, which is an insulating material. A radio frequency of several MHz is applied to the solenoid coil, and Ar gas flowing through the water-cooled tube is excited to generate thermal plasma. The internal temperature of the generated thermal plasma reaches a high temperature of over 10,000 K, and the size of the plasma jet is 5 to 10 cm in diameter. The raw material powder is dropped into the thermal plasma together with the carrier gas using a powder feeder to evaporate the raw material powder. The processed material stays for approximately 10 ms in the plasma. During this time heating and decomposition

reactions occur in the plasma. The evaporated raw material gas flows from the end of the plasma jet into a water-cooled chamber made of stainless style, where it is rapidly cooled down at the rate of 10^{-5} to 10^{-7} K/s.

In a typical evaporation and condensation process, the raw material vapor becomes supersaturated during the cooling process, generating nucleus particles, which then undergo a process of nucleus particle growth as they condense and progress, and a process of particle-to-particle condensation (collision and coalescence) to become nanoparticles. On the other hand, the condensation process between the nanoparticles generated at the same time also occurs simultaneously on the order of a few ms, but the powder carried by the carrier gas is classified by a nano-sized mesh and finally collected by a bug filter. The disadvantage of this production process is that the amount of nanoparticles that can be produced from the raw material input is limited to the amount of raw material powder that does not evaporate and the powder that has condensed into powder larger than nano size must be discarded, so it cannot be used for a mass-production.

2.1.2 Raw Material

In the RF thermal plasma method, a powdered raw material of about a few μm is used to evaporate the material introduced into the thermal plasma. The elements contained in the raw material become vapor, which is cooled and becomes nanoparticles. Impurities contained in the raw material are also contained in the generated nanoparticles. In order to find a better raw material, we analyzed raw materials provided by various suppliers.

Material for 1st Test

Table 2.2 shows the mass concentration of elements in the raw material powder measured by ICP-AES (see Appendix C.2). The pure vanadium powders used as raw materials were pure V powder (particle size: about 75 μm, purity: 99.5 %) manufactured by Nilaco, pure V powder (particle size: about 75 μm, purity: 99 %) manufactured by Kojundo Kagaku Kenkyusho, and pure Ni powder (particle size: about 10 μm, purity: 99.99 %) manufactured by Nilaco. Pure Ni powder was prepared to produce alloy nanoparticles with vanadium. From Table 2.2, it can be seen that the metal contamination in the raw powder was less than 1 wt.%, and metal contamination was not the main source of contamination. In the case of vanadium raw powder, it was found that it contains several to several tens of wt.% of light elements that cannot be measured by ICP-AES.

Table 2.2: ICP-AES analysis of raw powder used in 1st prototype test

Element	$V_{(Nilaco)}$ (wt.%)	$V_{(Kojundo)}$ (wt.%)	$Ni_{(Nilaco)}$ (wt.%)
Mg	0.009	0.0004	—
Al	0.001	0.005	0.0003
Si	0.007	0.034	0.004
Ca	0.007	0.005	0.005
Ti	0.008	0.001	—
V	87.3	96.8	0.01
Cr	0.06	—	—
Mn	0.003	—	—
Fe	0.04	—	—
Ni	0.004	0.002	99.1
Zn	0.01	—	—
Total	87.449	96.8474	99.1193
Metal contamination	0.149	0.0474	0.0193
Unidentifiable	12.55	3.1526	0.8807

Material for 2nd Test

The raw material powder used in the 2nd prototype test was prepared as vanadium raw material with a known low oxygen concentration based on the results of the 1st test. Vanadium powder with a particle size of 100 mesh (150 µm) manufactured by Taiyo Koko Co., Ltd. was used as the vanadium raw material powder for the RF thermal plasma method. Table 2.3 shows the elemental analysis results of the vanadium powder provided by Taiyo Koko Co., Ltd.

Table 2.3: Mass concentration of contaminant elements contained in Taiyo Koko's V raw material powder

Data No.	Analysis	Al	Si	Fe	C	O	N	V	Mo
Product certificate	—	0.001	0.032	0.008	0.001	0.186	0.014	—	0.005

The elemental composition of the vanadium powder provided by Taiyo Koko Co., Ltd. is analyzed before nanoparticle production. The most abundant impurity in the vanadium powder was oxygen, at a concentration of 0.186 wt.%, which is lower than the concentration in the raw material used in the 1st test. The 2nd test was conducted from May 25th to 28th, 2023.

2.1.3 Nanoparticle creation test

The creation test was conducted twice. In this section, the test contents of the 1st and 2nd tests, which changed the raw materials and storage process, are introduced.

Vanadium is a substance that is easily oxidized, and when it comes into contact with air, the surface layer begins to oxidize. Therefore, in the RF thermal plasma method, inert gas is used as the plasma gas to generate nanoparticles.

The flow of the work process is as follows. First, the raw material powder is opened in a glove box filled with Ar gas, and the amount used is weighed. An oxygen concentration meter is connected in the glove box, and the oxygen concentration during the work was about 100 to 1000 ppm. When generating V-Ni alloy nanoparticles, the mixing ratio of vanadium raw material powder and nickel raw material powder is adjusted. This adjustment method needs to take into account the difference in the heat of evaporation of vanadium and nickel and the difference in raw material particle size. The nickel content of the nanoparticles generated from a powder mixed with V and Ni raw material powders in a certain ratio was analyzed and readjusted. The weighed raw material powder is placed in a powder feeder, sealed, and connected to a plasma torch. The raw powder is supplied at a rate of 110 to 120 g/h. A mixture of Ar and H_2 gas was used as the plasma gas. A few percent of H_2 gas is mixed into the Ar gas of the plasma gas in order to reduce the amount of oxygen that adheres to the raw material.

1st Prototype test

Two types of plasma gas were used: only Ar gas and a mixture of Ar and H_2 gas, to investigate the reduction effect of H_2 gas. The samples produced by thermal plasma treatment are packed in glass bottles in a glove box, placed in aluminum bags with silica gel, and vacuum-sealed in the atmosphere. The Ni mixing ratio of the alloy powder is readjusted based on the elemental analysis results of the powder produced. Details of the manufacturing test are shown in Table 2.4. Tested from October 17th to 18th, 2022.

Table 2.4: Conditions for the 1st production test

No.	Raw powder	Weighting	Plasma gas	Corrected powder
S1-1	V-k	100 g	Ar + H_2	3.2 g
S1-2	V-k	50 g	Ar	0.2 g
S1-3	V-n	75 g	Ar + H_2	2.1 g
S1-4	V-n	75 g	Ar	0.8 g
S1-5	V-k + Ni(1.2 wt.%)	50 g	Ar + H_2	0.3 g
S1-6	V-k + Ni(1.0 wt.%)	50 g	Ar + H_2	1.8 g

V-k : Vanadium raw powder of the Kojundo Chemical Laboratory Co.,LTD.
V-n : Vanadium raw powder of the Nilaco corporation.
Ni : Nickel raw powder of the Nilaco corporation.

The nanoparticle creation efficiencies when using only Ar gas and a mixture of Ar and H_2 gas as the plasma gas were $< 1\,\%$ and $3\,\%$, respectively. The composition ratios of the samples prepared in Table 2.4 were analyzed by XRD immediately after preparation. Figure 2.2 shows the XRD analysis results for sample S1-3. The oxide state of S1-3 is $V_{16}0_3$. The oxygen content in this case is equivalent to 5.53 wt.%, and the b_{coh} of oxygen is 5.803 fm. If elements other than vanadium are ignored, $V_{16}0_3$ is calculated to be $b_{\mathrm{coh}} = 0.45$ fm. This value is smaller than the coherent nuclear scattering length of natural vanadium. In this analysis, V powder sometimes ignited when taken out in air, and it is possible that the sample was oxidized in a short time. Therefore, in oxygen analysis, elemental analysis must be performed without exposing it to air.

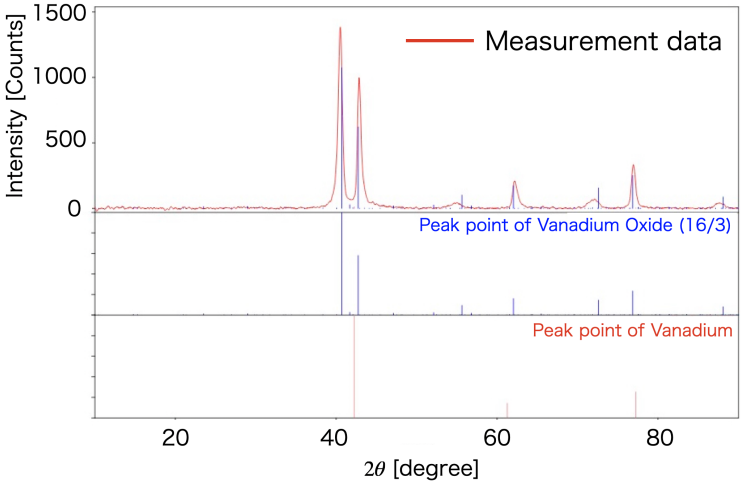

Figure 2.2: XRD analysis of sample S1-3 immediately after creation.

2nd Prototype test

Based on the analysis results of the 1st test, Ar mixed with H_2 gas was used as the plasma gas. The sample powder was stored sealed in an aluminum-coated plastic bag with an oxygen absorber. The rest of the production process was the same as for the 1st prototype. Assuming that it may not be possible to completely remove oxygen, natural vanadium nanoparticles were also produced. Details of the powder produced in 2nd test are shown below in Table 2.5.

Table 2.5: Conditions for the 2nd production test

No.	Raw powder	Weighting value	Plasma gas	Corrected powder
S2-1	V-t	500 g	Ar + H_2	21.6 g
S2-2	V-t + Ni	250 g	Ar + H_2	7.5 g

V-t : Vanadium raw powder of the Taiyo Koko Co.,LTD.
Ni : Nickel raw powder of the Nilaco corporation.
Ni powder content of S2-2 : Ni = 1.9 wt.%

2.2 Analysis using FE-SEM

In this chapter, the characteristics of the V and V-Ni nanoparticles are analyzed using a scanning electron microscope (SEM) (see Appendix C.1). First, in Sec. 2.2.1, commercial V nanoparticles and nanoparticles created by the RF thermal plasma method are photographed and compared using SEM. In Sec. 2.2.2, the main elements contained in the sample particles are identified using EDS analysis. In Sec. 2.2.3, the particle size of the nanoparticles created by the RF thermal plasma is analyzed from the SEM images.

2.2.1 Comparison with Commercially Available Nanopowder

The sample powders (S2-1 and S2-2 in Table 2.5) created by RF thermal plasma are compared with commercially available(C.A.) vanadium nanoparticles. As far as we could find, only one company was found to produce V nanoparticles. The purity and the size of the V nanoparticles published on the website is 99.9 wt.% and 80 $\sim$ 100 nm, respectivel.

To select the best target for the SANS experiment, we analyzed the particle size and impurity concentration. The impurity concentration will be introduced in Sec. 2.3. Fig. 2.3 shows the appearance of the sample powder created in the 2nd test and the commercially available V powder. In general, the smaller the particle size, the less metallic luster it has and the blacker it appears. The color of the C.A. powder looked the same as bulk vanadium.

Figure 2.3: Image of sample powder: (left) Commercial vanadium nanopowder, (middle) Sample powder of S2-1 and (right) Sample powder of S2-2

Next, the size of C.A. powder and created sample powder were compared using SEM at different magnifications, and the results are shown in Fig. 2.4. Only particles with diameters of several tens of microns were observed in the C.A. powder, suggesting that there are almost no nanoparticles in the vanadium nanopowder provided by C.A.

On the other hand, in (d)$\sim$(f) in Fig. 2.4, it is observed that there are boundaries between each particle in the aggregated material. The sample powder (S2-1 in Table 2.5)

was observed at the highest possible magnification (mag.) using an SEM. Figure 2.5 confirmed spherical particles with diameters of $< 50\,\text{nm}$.

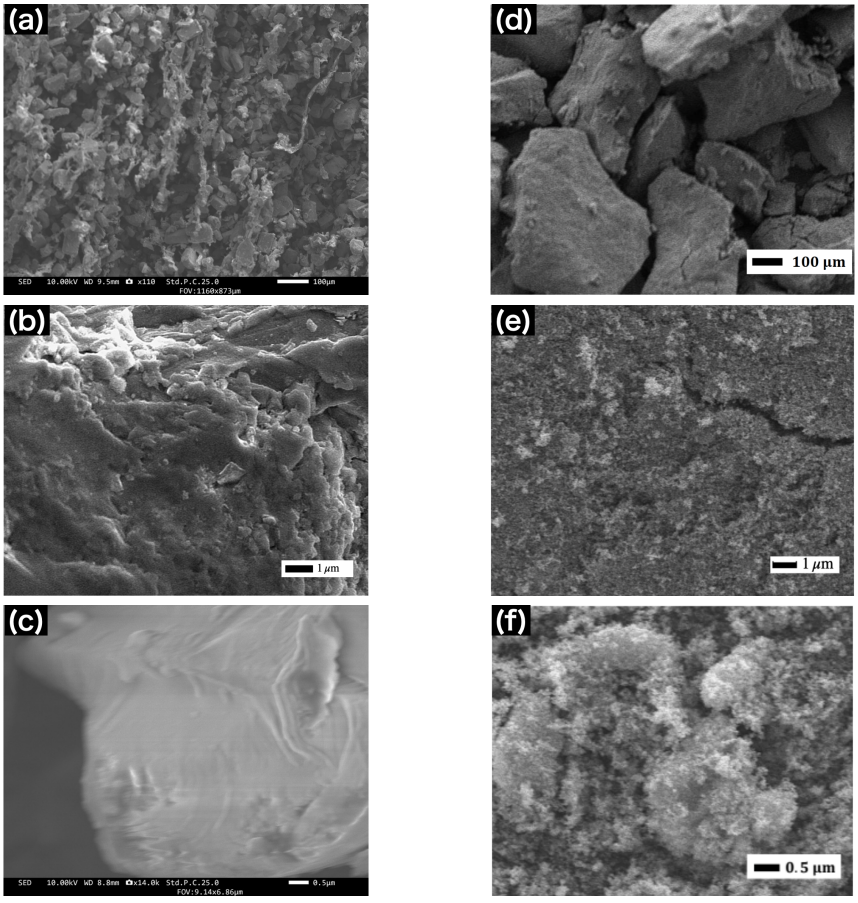

Figure 2.4: Compare the SEM images of C.A. powder with created powder.(left) C.A. powder [mag. of (a)∼(c) image :110×, 9.00k× and 14.0k×], (right) created powder [mag. of (d)∼(f) :95.0×, 8.00k× and 16.0k×].

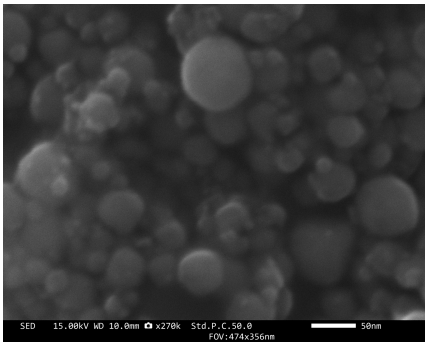

Figure 2.5: High-magnification image of S2-1 powder [mag.: 270k×].

2.2.2 Particle Size Analysis

Figure 2.6 shows SEM images of the sample powders made from the V raw powder (S1-1) and V+Ni raw powder (S1-6) shown in Table 2.4. Both SEM images, made from different raw materials, show nearly spherical particles with diameter of less than 50 nm.

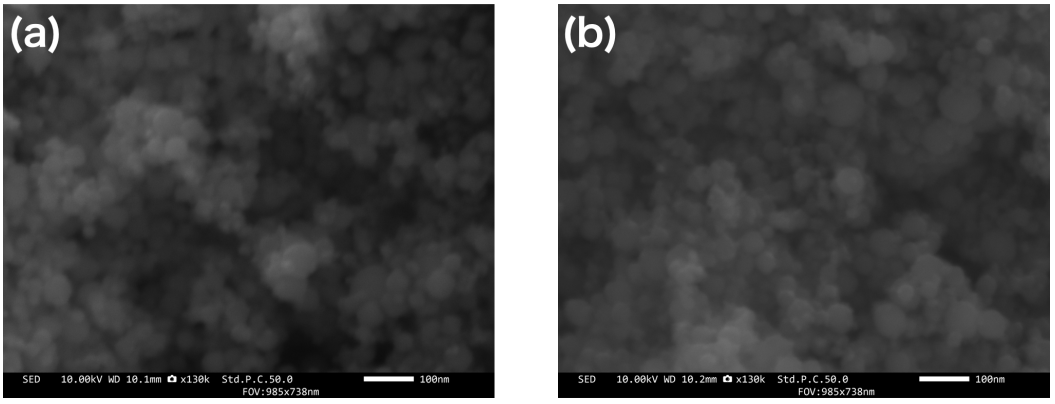

Figure 2.6: SEM image of sample powder created using the different raw powder :(a) S1-1 sample powder and (b) S1-6 sample powder

To analyze the SEM images, we used the free image analysis software Image J Fiji to determine the size of the particles in the image from the scale bar corresponding to the photograph. In order to analyze the particle size using Image software, scribe lines to identify the outer diameter of each particle. The analysis process determines the particle size through four processes as shown in Fig. 2.7.This SEM image is one of the SEM images used for analysis.

Analysis Process

(1) A high-magnification SEM image of the sample powder was taken.

(2) Auxiliary lines are drawn assuming the particle outlines to be circles.

(3) The particles with outlines are filled in and the position of the filled in outlines is shifted so that particles do not adjoin each other.

(4) Image J Fiji to automatically recognize the filled-in particles, and the area of each particle is derived using the scale bar of the SEM image

The particle size distribution was created by deriving the equivalent radius from the area of each particle, which is assumed to be spherical.

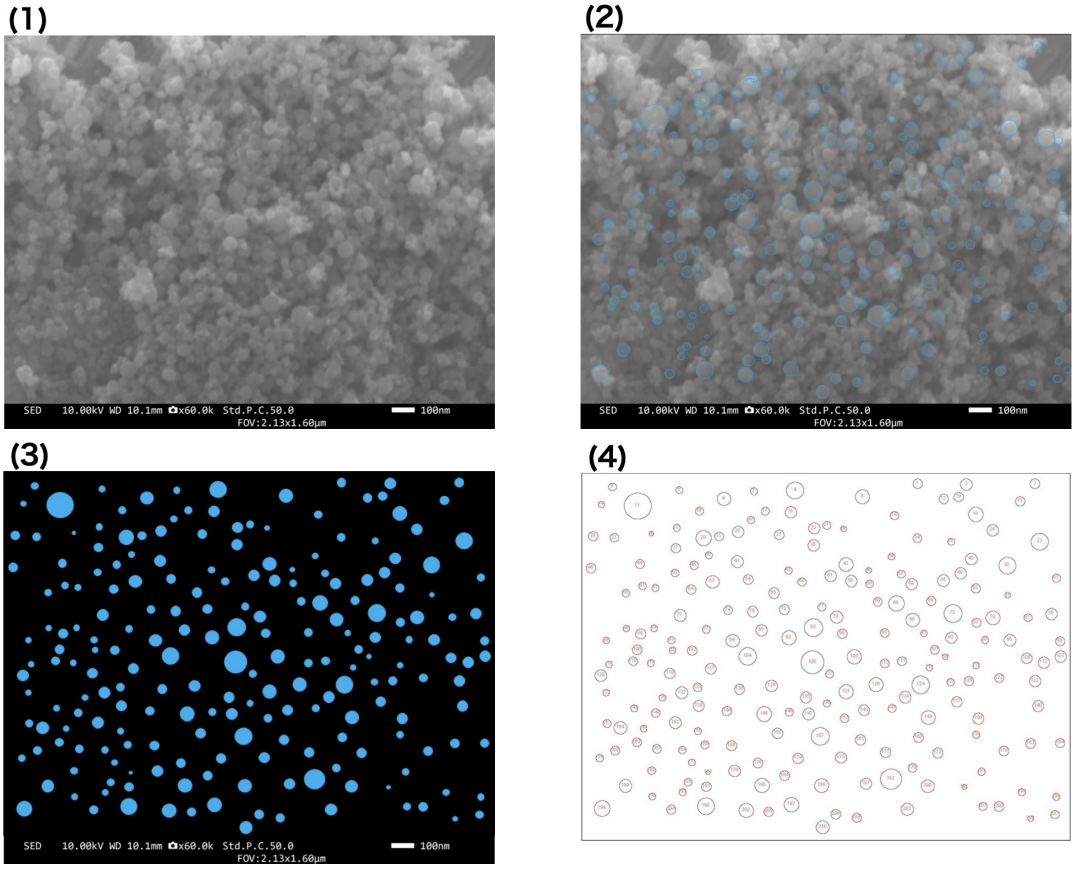

Figure 2.7: SEM image analysis of S2-1 sample powder: (1) is the SEM image used for analysis, (2) is the outline of the analyzed particle in the SEM image, (3) is the image read into the image software after outline processing, (4) is the particle recognized by Image J Fiji.

The particle size distribution obtained by analyzing the SEM image is shown in Fig. 2.8. The number of analysis point of the particle is 1002. In addition, Fig. 2.8 shows the results of fitting the particle size distribution obtained with the log-normal distribution function shown in Eq. (2.1).

$$f(R) = \frac{\mathrm{Norm}}{\sigma R} \exp\left(-\frac{1}{2}\left(\frac{\ln(R) - \mu}{\sigma}\right)^2\right) \tag{2.1}$$

where, R is the radius of the particle. The fit parameters Norm is the normalization factor, σ is the standard deviation, and μ is the median particle size distribution. The average particle size $\bar{x}$ is expressed as $\bar{x} = \exp(\mu + \sigma^2/2)$. The results of each parameter obtained by the fitting analysis were $\mu = 2.997$ and $\sigma = 0.3622$. The average radius of the particles in the obtained particle size distribution is 21.38 nm. The log-normal distribution function used for fitting is a function commonly used in powder technology to represent particle size distribution.

The particle size distribution obtained by this analysis only covers the particle size that can be confirmed with the resolution and magnification of the SEM image. Therefore, if there are particles smaller than the size that can be confirmed in the field of view, they cannot be analyzed.

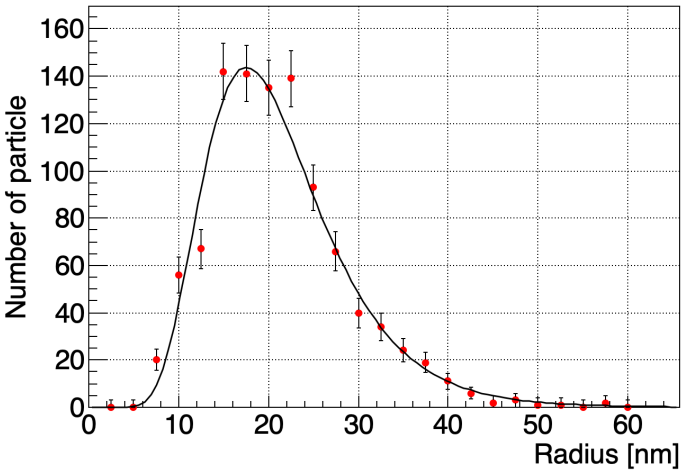

Figure 2.8: Particle size distribution of S2-1 sample powder obtained by the analysis of SEM images

2.2.3 EDS Analysis

In this section, we perform EDS analysis on the powders shown in the SEM images to identify the major elements. The powder samples are fixed on carbon tape or gold foil for analysis. Please refer to the details and methods of EDS analysis (see Appendix C.1). The analytical accuracy of EDS is about 1 wt.%. The elements detected in the sample powder by simple EDS analysis will be analyzed in more detail in the next section.

First, the analysis points and characteristic X-ray distribution of each created powder are shown in Fig. 2.9. And Table 2.6 is the content of elements detected at each point.

From the element analysis table, C and O from the carbon tape are detected outside the powder. Other elements are the same as the main elements of the raw materials.

The quantitative values shown in Table 2.6 are normalized so that the sum of the detected elements is 100 wt.%.

In the S1-6 powder, which was created by mixing Ni with the raw powder, Ni was detected at all points in the point analysis of Spc_008 to Spc_011. The Ni content may vary slightly from particle to particle. The average V and Ni content ratios in the S1-6 powder, excluding C and O, were 94.94 ± 1.43 wt.% and 5.06 ± 1.43 wt.%, respectively. These results are explained in more detail in Table 2.11 in Sec. 2.3.3.

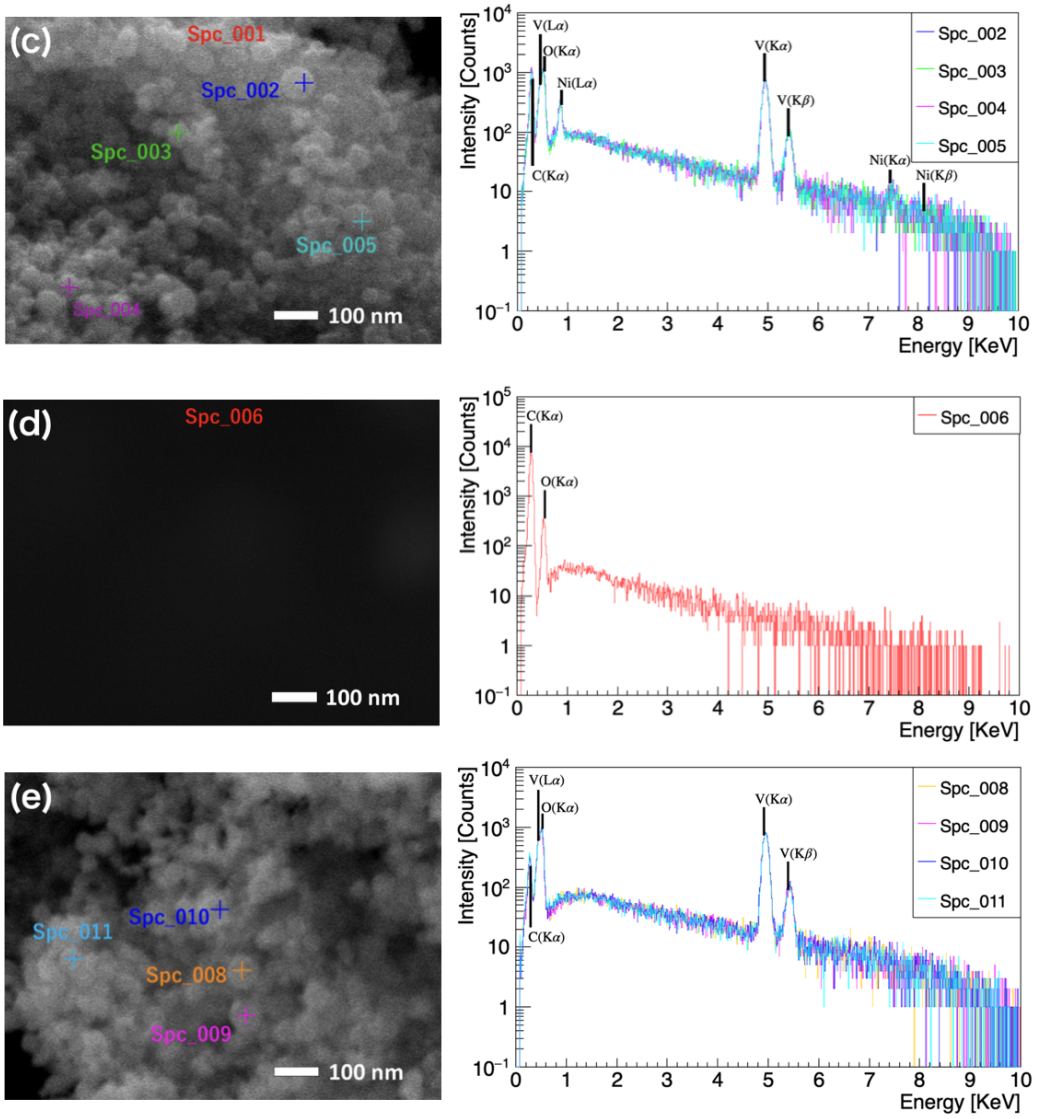

Figure 2.9: Analysis point by EDS and characteristic X-ray spectrum: (c) S1-1 powder(Spc_002 ∼ 005), (d) Carbon tape, (e) S1-6 powder(Spc_008 ∼ 011).

Table 2.6: Element mass concentration of created powder by EDS

Samaple	Data No.	Analysis	C (wt.%)	O (wt.%)	V (wt.%)	Ni (wt.%)
S1-1 (V)	Spc_002	Point	4.30(7)	8.73(35)	86.97(123)	-
	Spc_003	Point	4.14(7)	7.24(33)	88.62(124)	-
	Spc_004	Point	4.18(6)	11.28(36)	84.54(119)	-
	Spc_005	Point	4.64(7)	13.52(38)	81.84(117)	-
Carbon tape	Spc_006	Area	89.53(25)	10.47(25)	-	-
S1-6 (V + Ni)	Spc_008	Point	14.68(11)	15.58(35)	65.53(97)	4.41(84)
	Spc_009	Point	15.24(12)	9.93(32)	70.33(105)	4.50(88)
	Spc_010	Point	14.89(11)	15.37(36)	67.53(101)	2.21(71)
	Spc_011	Point	13.04(11)	14.69(36)	68.83(102)	3.44(79)

The elemental distribution in the S1-6 powder is shown in Fig. 2.10. Vanadium and nickel were detected in the area where particles were visible, and Ni is thought to be uniformly mixed at the atomic level.

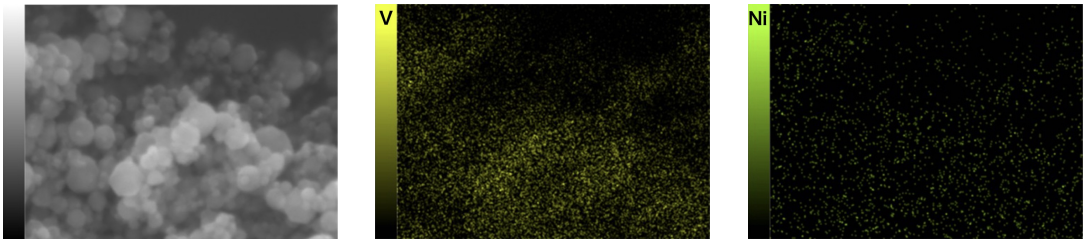

Figure 2.10: Detected position by EDS of each element in the S1-6 powder

Next, the elemental distribution in the C.A. powder is shown in Fig. 2.11. Elements other than V, such as Al, Si, Cr, and Mn, were detected in the powder, and the elemental distribution is different.

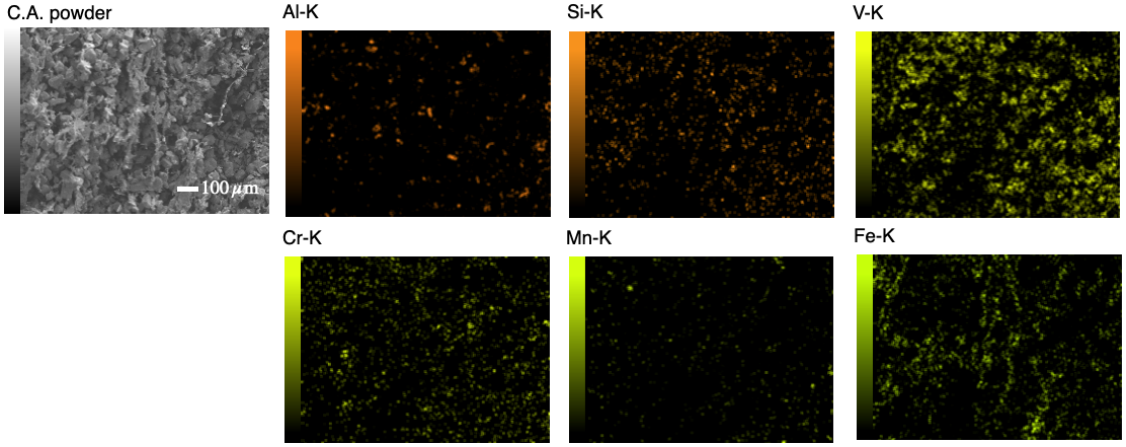

Figure 2.11: Detected position by EDS of each element in the C.A. powder

The content of each element is shown in Table 2.7. Contamination mainly from Fe was detected in the powder. Oxygen may have been contaminated by handling the sample powder in air. In addition, the results of more accurate quantitative analysis of the major elements detected by EDS will be explained in the next section.

Table 2.7: Element mass concentration of C.A. powder by EDS

	C	O	Al	Si	V	Cr	Mn	Fe
C.A. powder	1.43 %	10.9 %	4.15 %	0.30 %	44.52 %	0.89 %	3.41 %	34.41 %

2.3 Nuclear Scattering length of Target

This chapter introduces the selection of targets to be used in SANS experiments and the nuclear scattering length of the target estimated from the elemental content.

Sec. 2.3.1 shows the results of analysis of the oxygen contained in each sample powder without exposure to air. Sec. 2.3.2 introduces the method for determining the elemental content in the target powder. Sec. 2.3.3 introduces the nuclear scattering length of the target calculated from the elemental content.

2.3.1 Oxygen Analysis without Exposure to Air

From the EDS analysis in Sec. 2.2.3, the main elements contained in the sample powders created are almost the same as those in the source material. However, in order to estimate the content of light elements such as oxygen, analysis without exposure to air is required.

Oxygen analysis without exposure to air was conducted by an analytical company (see Appendix C.3). Table 2.8 shows the analytical results of the created powder and the C.A. powder. The values in the table are quantitative values calculated from the powder mass.

Table 2.8: Quantitative analysis of O & H element in the each sample powder

Samaple	Raw material	Plasma gas	No.	O (wt.%)	H (wt.%)
S1-1	V-k	$Ar + H_2$	1st	14.4	0.153
			2nd	14.9	0.164
			3rd	14.6	0.151
			Average	14.6(3)	0.156(7)
S1-2	V-k	Ar	1st	19.8	0.213
			2nd	20.6	0.218
			3rd	20.3	0.224
			Average	20.3(4)	0.218(6)
S1-6	V-k + Ni	$Ar + H_2$	1st	13.5	0.173
			2nd	13.0	0.169
			3rd	13.6	0.166
			Average	13.4(3)	0.169(4)
S2-1	V-t	$Ar + H_2$	1st	6.13	-
			2nd	6.30	-
			3rd	6.02	-
			Average	6.15(14)	-
S2-2	V-t + Ni	$Ar + H_2$	1st	11.4	-
			2nd	11.4	-
			3rd	11.4	-
			Average	11.4(1)	-
C.A.	—	—	1st	4.11	-
			2nd	4.37	-
			3rd	4.14	-
			Average	4.21(14)	-

The analyzed samples were the powder created by RF thermal plasma shown in Table 2.4 and Table 2.5, and the C.A. powder. Oxygen has a positive nuclear scattering length of $b_{\mathrm{coh}} = 5.803\,\mathrm{fm}$. When oxygen contains 6 wt.%, the nuclear scattering length exceeds the value of $^{\mathrm{nat}}$V.

Of the powders created, the S2-1 powder had the lowest oxygen content. This sample powder was created using the raw powder with the lowest oxygen content. The oxygen content of the S2-1 powder is 6.15(14) wt.%. The content error is estimated from three measurements for each sample. The other powders created had an oxygen content of over 10 wt.%. The oxygen content of C.A. powder is 4.21(14) wt.%. Therefore, the candidate targets are the S2-1 powder or the A.C. powder. In the next section, we will perform other elemental analysis results and calculate the nuclear scattering length.

2.3.2 Elemental Content Analysis Process

Calculate the elemental content values from the different elemental analyses. The elemental composition ratios measured by ICP-AES and EDS are normalized by subtracting the oxygen content measured in Sec. 2.3.1 from 100 wt.%. The reason for this is that ICP-AES and EDS measurements are performed with exposure to air. Metal elements are analyzed by ICP-AES (see Appendix C.2), and Carbon is analyzed by EDS. Carbon is analyzed by placing the sample powder on Au foil to prevent elements from the Carbon tape, etc. from being detected (see Appendix C.1).

Detected element by EDS in S2-1 powder is shown by Table 2.9, the content of O is 5.51 ± 0.14 wt.%, which is lower than the 6.15 ± 0.14 wt.% of the oxygen analysis result without exposure to air shown in Table 2.8. This may be because the characteristic X-ray peaks of O and V mentioned above overlap in the energy resolution of EDS, and because the sample powder was taken out into the air before SEM analysis, which may have changed the original O content.

Table 2.9: Composition ratio of elements in the S2-1 powder analyzed by EDS

Samaple	C	O	V
S2-1	0.69±0.01	5.51±0.14	93.79±0.31

Next, Sec. 2.3.3 explains the value of the nuclear scattering length, which is calculated from the elemental composition ratio.

2.3.3 Calculation of the Average Nuclear Scattering Length

Table 2.10 shows the nuclear scattering length value calculated from the composition ratio in each sample particle. The elemental contents were normalized to the content of each element as described in Sec. 2.3.2. Mass concentration errors are standard deviations from multiple measurements. The errors in the scattering length data list are systematic errors.

Table 2.10: Average nuclear scattering length of S2-1 powder and C.A. powder calculated by composition ratio.

	b_{coh} (fm)	σ_{inc} (b)	σ_{abs} (b)	C.A. (wt.%)	S2-1 (wt.%)
C	6.6484(13)	0.001(4)	0.00350(7)	1.93	0.67(1)
O	5.805(4)	0.0000(8)	0.00019(2)	4.21(14)	6.15(14)
B	5.30(4)	1.70(12)	767(8)	0.024(3)	0.0018(28)
Mg	5.375(4)	0.08(6)	0.063(3)	0.021(2)	0.003(9)
Al	3.449(5)	0.0082(6)	0.231(3)	0.633(31)	0.0088(1)
Si	4.15071(22)	0.004(8)	0.171(3)	0.584(44)	0.043(1)
Ca	4.70(2)	0.05(3)	0.43(2)	0.046(6)	0.0036(30)
Ti	-3.730(13)	2.87(3)	6.09(13)	0.009(1)	0.0012(1)
V	-0.555(3)	5.08(6)	5.08(4)	61.4(33)	92.96(1)
Cr	3.635(7)	1.83(2)	3.05(6)	0.117(4)	0.028(1)
Mn	-3.750(18)	0.40(11)	13.3(2)	2.644(296)	0.002(1)
Fe	9.45(2)	0.40(11)	2.56(3)	27.462(3779)	0.084(1)
Ni	10.3(1)	5.2(4)	4.49(16)	0.055(2)	—
Cu	7.718(4)	0.55(3)	3.78(2)	0.158(30)	—
Zn	5.680(5)	0.07(7)	1.11(2)	0.005(1)	0.009(1)
Mo	6.715(2)	0.04(5)	2.48(4)	0.705(62)	—
$P_{\mathrm{C.A.}}$	2.989±0.314	2.85±0.19	4.37 ±0 .26	—	—
$P_{\mathrm{S2-1}}$	0.719±0.023	4.08±0.02	4.64±0.87	—	—

Value of scattering length and cross section par unit particle

$P_{\mathrm{C.A.}}$ is V nanoparticle of C.A..

$P_{\mathrm{S2-1}}$ is nanoparticle of S2-1 sample particle by created by RF thermal plasma method.

Where b_{coh}, σ_{inc} and σ_{abs} are coherent nuclear scattering length, incoherent nuclear scattering cross section, and absorption cross section in the case of thermal neutron. Each value were calculated from the composition ratio of each element detected. Each element was assumed to be uniformly distributed within the particle, and each value was calculated as the average value for one atomic nucleus. The value of b_{coh} of C.A. powder and the S2-1 sample powder were calculated to be 2.989(314) fm and 0.719(23) fm. In the case of S2-1 powder, the value was close to the coherent nuclear scattering length of natural vanadium, −0.555 fm. The S2-1 powder was suppressed to a value smaller than that of other elements, the S2-1 sample particle was adopted as the target for the SANS experiment. The diffuse scattering cross section of S2-1 powder was calculated to be 0.83 b from Eq. (B.42) using the composition ratio.

Next, the ICP-AES analysis results for the Ni content of the V-Ni alloy nanoparticles of the S1-6 powder are shown in Table 2.11.

Table 2.11: Mass concentration of the S1-6 powder

	V (wt.%)	Ni (wt.%)	Other metal (wt.%)	Not detected (wt.%)
S1-6	84.2(15)	5.7(1)	0.147	10.0

The V and Ni content ratios were 93.6(16) wt.% and 6.4(1) wt.%, respectively. This value is the average value for the entire powder and agrees within the error range with the EDS analysis results in Sec. 2.2.3. The alloy content that can be adjusted by the RF thermal plasma method is about 0.5 wt.%, and the target Ni content of 5.8 wt.% was adjusted within the margin of error. However, the Ni content of the particles may vary by about 1 wt.%. The S1-6 powder was not adopted as a target due to contamination by oxygen.

2.4 SAXS Measurement

Manual analysis of particle size distribution using SEM images has a difficulty in increasing number of analyzed particles. Furthermore, the resolution of an SEM is around 1 nm, so there is a possibility that particles of a few nm in size will be overlooked. Therefore, we measured the particle size distribution using SAXS (Small Angle X-ray Scattering). The measurement principle of SAXS measurement is the same as SANS (Small Angle Neutron Scattering), the experimental method in this paper. The momentum transfer distribution obtained by SAXS is determined by the particle size and shape of the targeted particle, so by analyzing the momentum transfer distribution, particle size information of the V sample nanoparticles used in the SANS experiment can be obtained. Since the diameter d of even the largest particle observed in the SEM image is 100 nm or less, the lowest momentum transfer to be measured can be calculated simply as $q = 2\pi/d = 0.06\,\mathrm{nm}^{-1}$.

2.4.1 Aichi-SR/BL8S3

The SAXS measurements were conducted at Aichi Synchrotron, and the experiment was carried out at BL8S3. The accelerator at Aichi Synchrotron Radiation Center (Aichi-SR) consists of a 50 MeV linear accelerator, a 1.2 GeV booster synchrotron, and a 1.2 GeV storage ring. The light source that generates the synchrotron light is generated by an electron storage ring with a circumference of 72 m and stored electron energy of 1.2 GeV.

Next, a schematic diagram from the light source of BL8S3 to the experimental hutch is shown in Fig. 2.12 [3]. BL8S3 uses hard X-rays emitted from a superconducting magnet installed in the storage ring. A single-wavelength beam is extracted using a slit (S1) 10 m away from the light source and a single-crystal X-ray monochromator (SXM). The SXM uses an asymmetric Ge crystal (asymmetric angle 10.5°), and the extracted energy was set to 8.2 keV ($\lambda = 1.5$ Å) by switching between the germanium crystal (111) and (220). The number of incident photons is 3.3×10^{10} Photons/sec when the energy is 8.2 KeV. The X-rays extracted from the spectrometer are incident on a flat focusing mirror (Th-coated Si crystal: M0) at an incidence angle of 4.5 mrad, and are reflected upward, passing through a slit (S2), a shutter (DSS: Down Stream Shutter), and a slit (S3), before being guided to the experimental hutch located 17 m away.

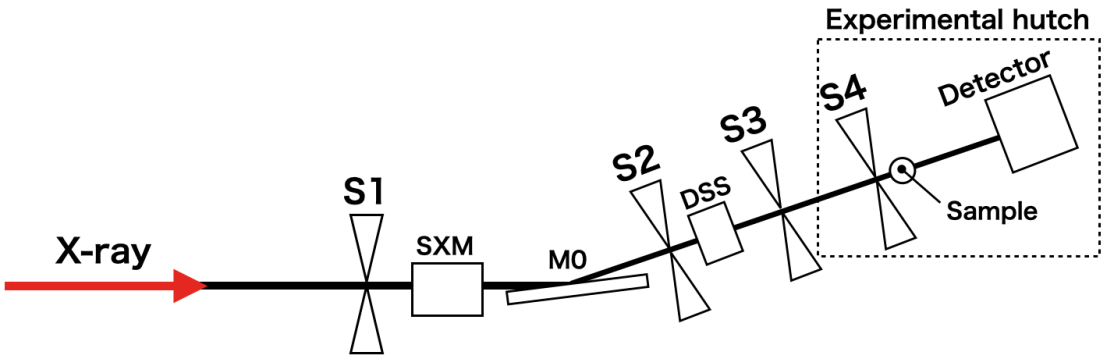

Figure 2.12: Optical axis system at BL8S3 [3]

The layout of the experimental hutch is shown in Fig. 2.13. The configuration after the S3 slit is lined up with a beam shutter, attenuator, S4 slit, sample, ion chamber (IC0, IC1 and IC2) and detector. In principle, the area other than the sample is a vacuum path. The beam intensity monitors IC0, IC1, and IC2 record the X-ray intensity entering the experimental hutch from the light source, the X-ray intensity incident on the sample, and the X-ray intensity transmitted through the sample, respectively. The intensity monitor outputs a value proportional to the current generated by the ion chamber.

At BL8S3, it is not assumed that precise X-ray intensity will be obtained, and the gas species are not strictly controlled, so the count rate of X-ray intensity cannot be obtained. The intensity monitor is used to measure the intensity of X-rays transmitted from a sample relative to the incident X-ray intensity, and to calculate the transmittance of the sample.

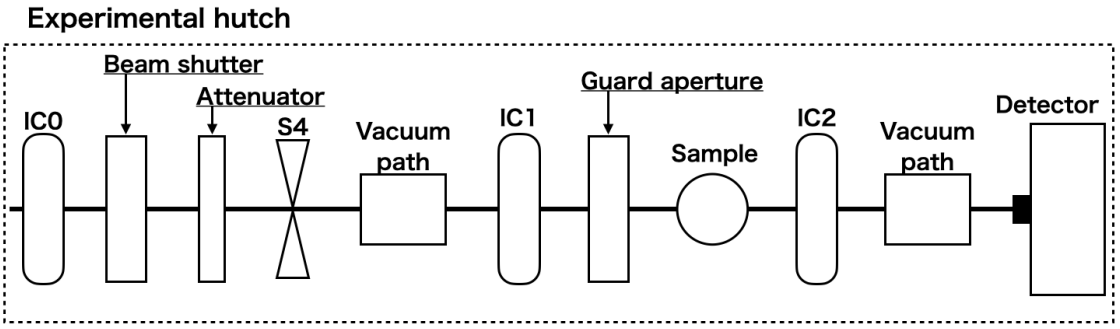

Figure 2.13: Layout of experimental hutch in BL8S3

The detector at the most downstream is used the PILATUS2M [10] as shown in Table 2.12. The light receiving part of the sensor module of the PILATUS detector uses a single silicon sensor (thickness 320 μm).

Table 2.12: Catalog specifications of PILATUS2M detector [10]

Number of modules	$3 \times 8 = 24$
Sensor	Reverse-biased silicon diode array
Pixel size	$172 \times 172\,\mu\text{m}^2$
Module size	$83.8 \times 33.5\,\text{mm}^2$
Format	$1475 \times 1679 = 2476525$ pixels
Intermodule gap	x : 7 pixels, y : 17 pixels, 7.97 % of total area
Dynamic range	20 Bit
Energy range	4.5 $\sim$ 36 keV
Energy resolution	500 eV

One side is a solid electrode on the high voltage side, and the other side is an array of charge collection electrodes spaced 172 μm apart.

Each pixel electrode is connected to an independent charge-sensitive preamplifier, allowing intensity data from one photon to approximately 10^6 (20 bits) to be recorded as an image.

A 6 mm diameter beam stopper (BS) with an embedded photodiode (1mm $\times$ 1mm) is attached to the center of PILATUS2M. The BS is attached to prevent transmitted X-rays from entering the detector and to prevent detector pile-up. The incident X-ray beam size is 1 mm horizontally and 0.5 mm vertically at the sample position (the beam size changes slightly depending on the camera length).

For the setup to measure the V sample nanoparticles, the camera length (distance from sample to detector) was 6365.38 mm, the aperture was 1.5 mm, and the wavelength of the incident beam was 1.5 Å. The measurable momentum transfer range was $q = 0.021 \sim 1.0\,\text{nm}^{-1}$.

2.4.2 Sample Cell

Next, the target cell must be fabricated taking into account the X-ray absorption cross section of the vanadium sample. Figure 2.14 shows the mass absorption curve for vanadium versus photon energy provided by NIST.

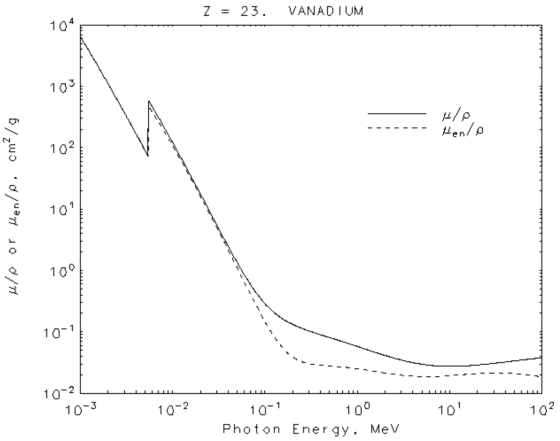

Figure 2.14: Mass attenuation coefficient μ/ρ as a function of photon energy

The polyimide tape was attached to one side of an aluminum plate with a hole of 10 mm in diameter. The corners of the polyimide tape were hardened with Araldite to prevent the intrusion of air and impurities. The sample powder was sealed in Ar gas using a vacuum glove box. To eliminate the effect of scattered light from the polyimide tape, an empty cell was also prepared. The thickness of the polyimide tape was 13 μm, and the transmittance of the empty cell was calculated to be 98 μm for the thickness of two sheets of polyimide tape, 26 μm.

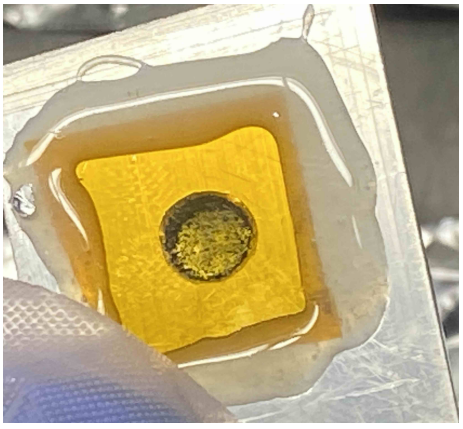

Figure 2.15: V sample powder fixed on Teflon tape for SAXS measurement

2.4.3 Measurement Data

SAXS measurements of V sample powder and an empty cell were performed on August 2, 2023. The details of the measurements are shown in Table 3.1. IC1 and IC2 indicate the X-ray intensity immediately before and after the sample, respectively. The transmittance of each sample is calculated using the IC1 and IC2 values. Air is data measured without placing a sample. Since the sample was placed in the air, this data is used to measure the attenuation of X-rays in the air. The transmittance by air at this time is 65 %. The sample GC (Glassy Carbon) is a standard sample for normalizing the scattering intensity.

Table 2.13: Change in intensity before and after X-rays hit each sample

Sample	Time [s]	IC1	IC2	Transmission
Air	120	2496013	1630121	0.6531
GC	120	2484481	883065	0.3554
V-nano	30	624075	208577	0.3342
Empty cell	30	625033	311076	0.4977

The transmittance of only the V-nano and Empty Cell is calculated from the transmittance of air. $IC1_{sample}$ and $IC1_{Air}$ denote the intensities of the incident X-rays in the measurements of the nanoparticle sample and the empty sample, respectively. The transmitted X-ray intensity is $IC2_{sample}$ and $IC2_{Air}$, respectively.

$IC1_{Air}$ is normalized based on the difference in $IC1_{sample}$ when each measurement is performed. The value calculated for $IC2_{Air}$ using the normalization constant is set as $IC2_{Air(norm)}$. This allows the transmittance to be calculated by calculating the attenuation due to air when each sample is measured. The calculation for this is shown in Eq. (2.2).

$$T_{\mathrm{sample}} = \frac{\mathrm{IC2_{sample}} + (\mathrm{IC1_{sample}} - \mathrm{IC2_{Air}(norm)})}{\mathrm{IC1_{samlpe}}} \tag{2.2}$$

Using the Eq. (2.2), the transmittance of the Empty cell and V-nano sample was calculated to be 84 % and 68 %, respectively. The two-dimensional image of the scattered X-rays from each sample obtained in this measurement is stored as a TIFF file with 32 bit floating point, 1475×1679 pixels. The intensity of X-rays incident on each pixel is determined by the brightness and darkness of the image. The obtained TIFF file is used to calculate the position distribution using the free software Fit2D, and the angular distribution per solid angle is calculated from the coordinates of the beam center. The parameters entered into Fit2D for the calculation were: distance from sample to detector: 6365.38 mm, scale of

one pixel: 172 μm, x and y positions of the direct beam: 684.21 mm and 797.84 mm, and incident wavelength: 1.5 Å. Figure 2.16 shows the angular distribution calculated from the TIFF file of the V-nano sample using Fit2D. The vertical and horizontal lines seen in

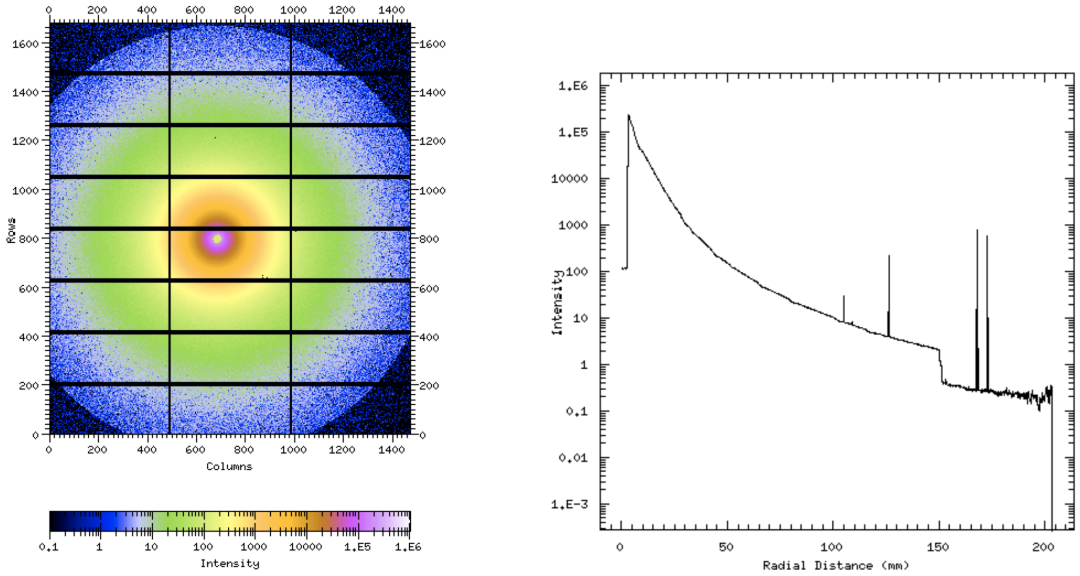

Figure 2.16: SAXS profile of the V-nano sample analyzed by Fit2D. (left) 2D plot of scattered X-rays, (right) the angular distribution.

the two-dimensional plot distribution on the left of Fig. 2.16 are dead gaps (vertical line : 7 pixels, horizontal line : 17 pixels) caused by gaps in the arrangement of the PILATUS2M detector elements. The angle distribution on the right is calculated with the center of the

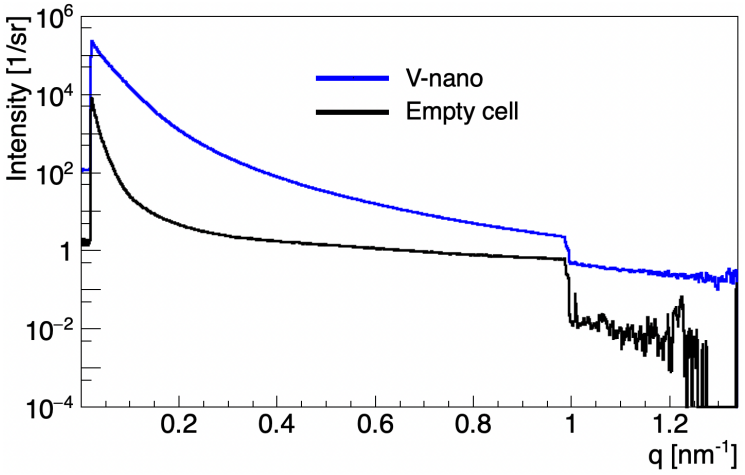

Figure 2.17: q distribution per unit solid angle of V-nano sample and empty cell measured by SAXS(after masking dead gaps and defective parts of detector elements)

circle seen in the two-dimensional distribution as the origin. Some peaks seen in the angle distribution are noise calculated from locations where detector elements are faulty.

The data for masking the dead gaps and the positions of the failed detector elements were provided by the instrument staff, and the momentum transfer distributions of each sample after correction are obtained as plotted in Fig. 2.17.

Next, the free software SasView was used to analyze the particle size distribution from the q distribution of the V sample nanopowder. SasView is an open-source small angle scattering analysis tool used in many neutron scattering facilities and synchrotron light facilities around the world, such asESS, ISIS, ILL, ANSTO, ORNL, NIST and PSI. Analysis of the absolute value of the momentum transfer distribution is not important for determining the particle size distribution. However, it is important to correct for factors that change the shape of the q distribution. The correction method is to compare the effects of instrument-specific factors (detection efficiency of each pixel, etc.) with the theoretical differential cross section of the GC sample, which is the standard sample. Figure 2.18 shows the results of a comparison of the differential cross sections of a GC sample measured with Aichi-SR and a GC (SRM3600) provided by NIST. The measurement results

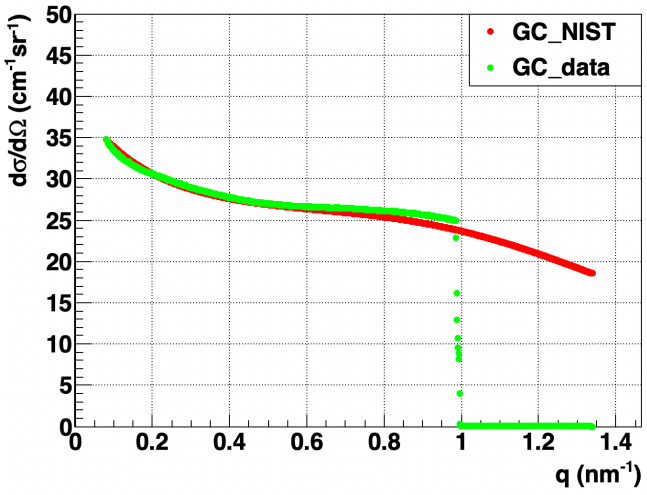

Figure 2.18: Measurement of GC standard samples and comparison with theoretical values [4]. (red line) the theoretical value. (green line) the measured data.

of the GC sample are normalized to the smallest q value in the NIST data list. The GC measurement values have the scattering intensity due to air subtracted. Comparing the theoretical red line with the measured green line in Fig. 2.18, the difference in intensity at each q is corrected for the intensity distribution of each sample as a factor specific to the PILATUS2M detector of Aichi-SR.

2.4.4 Particle Size Analysis

The V-nano sample data used in SasView is as follows Eq. (2.3). Here, $I(q)$ is the input data, $I_{s+c}(q)$ and $I_c(q)$ are the scattering intensities of the V-nano and the empty cell, $T_{s+c}(q)$ and $T_c(q)$ are the transmittances of the V-nano and the empty cell, and $N_{\mathrm{GC}}(q)$ is the correction factor from the GC standard sample.

$$I(q) = \left(\frac{I_{\mathrm{s+c}}(q)}{T_{\mathrm{s+c}}} - \frac{I_{\mathrm{c}}(q)}{T_{\mathrm{c}}} \right) \times N_{\mathrm{GC}}(q) \tag{2.3}$$

This calculation involves correction of the transmittance of the measured data and correction using a standard sample. In SasView, the parameters that determine the particle size distribution function can be determined by fitting the assumed particle shape information, scattering length information and scale factor to the input q distribution data.

The particle shape assumed for the particle size distribution was the sphere shape based on the particle shapes seen in SEM images. The form factor for a sphere shape is shown in Eq. (2.4). Also, scattering length information and other scale factors are not important for determining the particle size distribution, so they are free parameters.

The assumed particle size distribution function was a log-normal distribution Eq. (2.1) fitted to the particle size distribution obtained by analyzing the SEM images. The function to use for fit is shown in Eq. (2.6).

$$F(q,R) = 3V(R)\delta\rho \frac{\sin(qR) - qR\cos(qR)}{(qR)^3} \tag{2.4}$$

$$P_k(q) = \frac{[\mathrm{scale}]_{\mathrm{k}}}{\langle V(R) \rangle} \int [f(R,\bar{R},\sigma)]_k F^2(q,R) dR + \mathrm{background} \tag{2.5}$$

$$P_{sum}(q) = \sum_{k=1}^{n} P_k(q) \tag{2.6}$$

The formula Eq. (2.5) corresponds to the differential cross section. where, scale is a constant that normalizes the intensity, $V(R)$ is the volume of a sphere of radius R, $\delta\rho$ is the coherent electron scattering length, $f(R,\bar{R},\sigma)$ is the particle size distribution function, $\bar{R}$ is the average particle size and σ is the variance. The particle size distribution is determined by determining $\bar{R}$ and σ. Figure 2.19 shows the momentum transfer distribution of the

V-nano sample fitted using SasView.

The horizontal axis of Fig. 2.19 is the q distribution displayed as Å^{-1}. The blue line in the left figure of Fig. 2.19 is the q distribution of the V-nano sample measured by SAXS, and the orange line is the result of fitting using the formula Eq. (2.6). The fit range is $0.002 \sim 0.06\,\text{Å}^{-1}$.

First, the particle size distribution was fitted with a single log-normal distribution based on the information obtained from the SEM image. As a result, the particle size distribution analyzed using the SEM image could be fitted with a log-normal distribution as shown in Fig. 2.8, but the SAXS data could not be fitted in the high q region.

Therefore, to increase the degree of freedom of the particle size distribution, a function consisting of two or more log-normal distributions was used for fitting. By expressing the particle size distribution function as the sum of two or more log-normal distributions, the Eq. (2.6) defined in the analysis with SasView can be converted into a sum function as shown in Eq. (2.7) to obtain information on each particle size distribution. The fitting curve is calculated as the sum of these two or more particle size distributions. The number of added particle size distribution functions was increased to a maximum of five, and the results of fitting are shown in (b) to (e) of Fig. 2.19. The fitting parameters in this case are the scale_k that represents the ratio of each particle size distribution and the corresponding particle size distribution $[f(R, \bar{R}, \sigma)]_k$. Where k is the number of particle size distribution functions to be added.

$$P_{\text{sum}}(q) = \sum_{k=1}^{n} P_k(q) \propto \int \left(\frac{\text{scale}_1}{\langle V_1(R) \rangle} f_1(R, \bar{R}_1, \sigma_1) + \cdots + \frac{\text{scale}_\text{n}}{\langle V_n(R) \rangle} f_n(R, \bar{R}_n, \sigma_n) \right) F^2(q, R) dR \tag{2.7}$$

Figure 2.20 shows the fitting line and the residuals of the measured values obtained from the fitting results using Eq. (2.7). The reproducibility of the q distribution of the measured values by increasing the number of particle size distribution functions was found to be stable when the number of particle size distribution functions was increased up to five. Figure 2.21 shows the particle size distribution obtained from the fit results when using the five particle size distribution functions, which had the best reproducibility of the measured q distribution. Table 2.14 shows the parameters of each distribution obtained when using the five particle size distribution functions. The particle size distribution obtained by fitting is shown on the left side of the Fig. 2.21. A comparison of the particle size distribution calculated from the two particle size distributions with the results of SEM image analysis is shown on the right side of the Fig. 2.21.

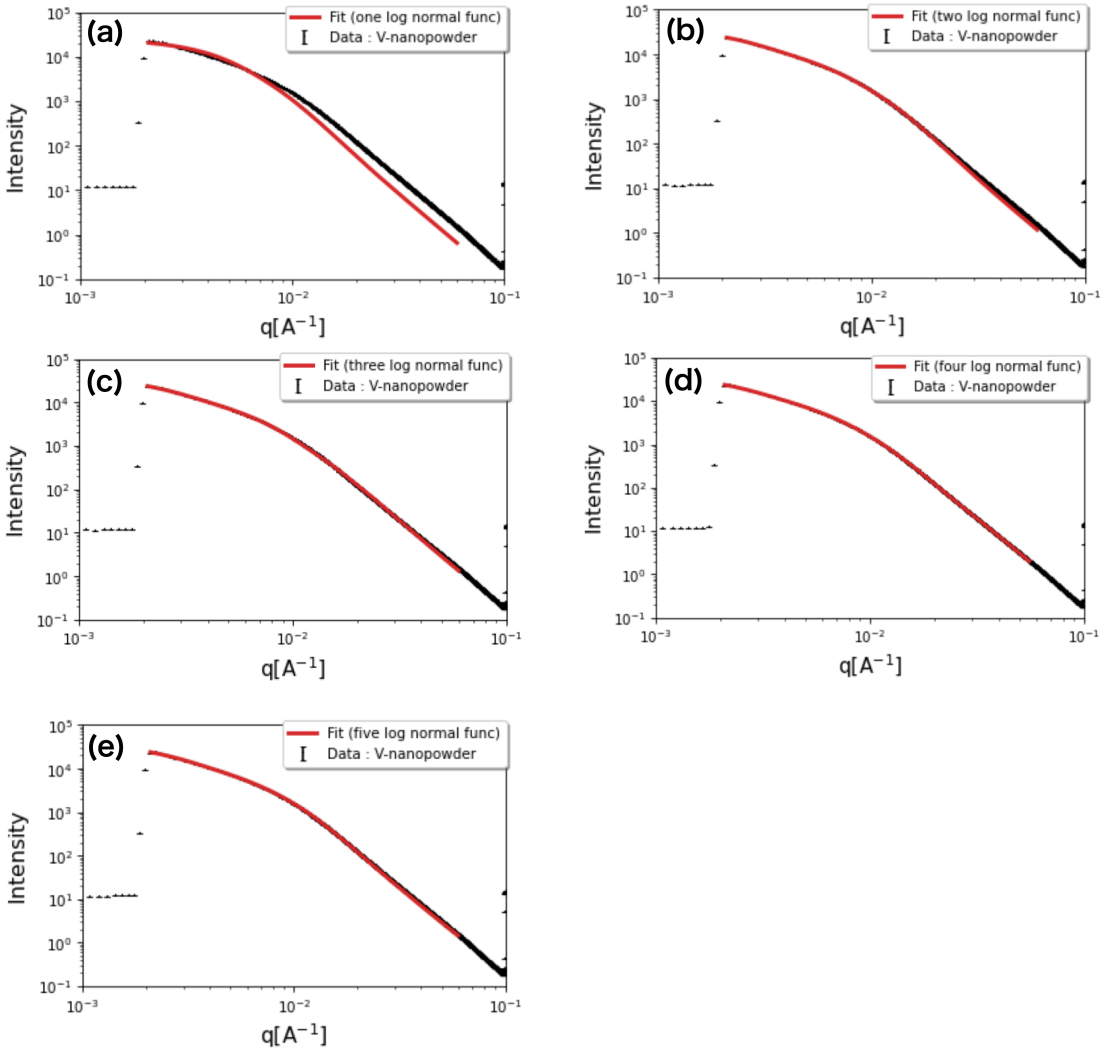

Figure 2.19: Fit results with Eq. (2.6) when changing the number of assumed particle size distribution functions.(black line) data,(red line) fitted curve. (a): Fit with one function, (b): Fit with two functions, (c): Fit with three functions, (d): Fit with four functions, (e): Fit with five functions.

Comparing the particle size distribution data from the SEM image in Fig. 2.21, the peak of the particle size distribution in the SAXS analysis is smaller, and it is thought that there are many small particles of a few nm in size that are difficult to analyze in the SEM image. To calculate the scattering intensity distribution of SANS, a particle size distribution that reproduces the momentum distribution of SAXS is used. The particle size distributions obtained by analyzing the nuclear configuration and electronic configuration of V nanoparticles are basically the same when compared with data obtained from a SANS experiment set up to measure a similar q range.

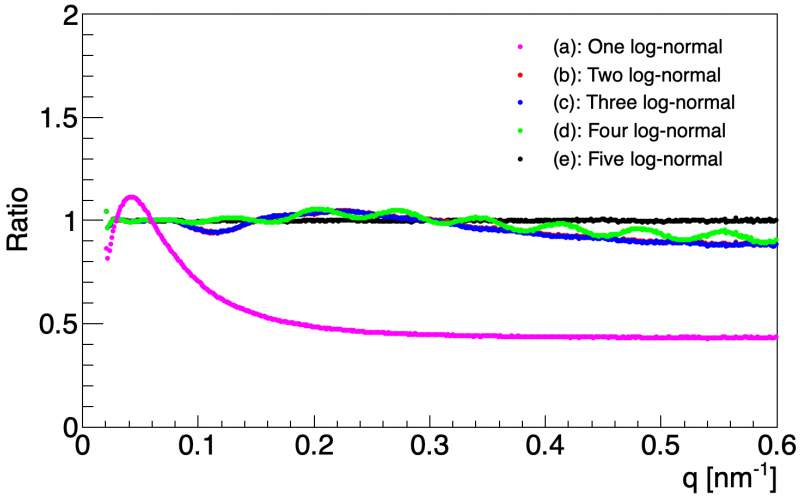

Figure 2.20: Ratio of SAXS data to theoretical curve when particle size distribution function is increased.

Table 2.14: Parameters of each particle size distribution obtained by fitting ((e):five particle size distribution) functions

	scale	R	σ
PSD1	0.0109±0.0003	15.7±0.2	0.562±0.008
PSD2	0.0042±0.0002	13.6±0.1	1.000±0.001
PSD3	0.053±0.001	13.9±0.1	0.408±0.004
PSD4	0.0200±0.0008	5.7±0.1	0.54±0.01
PSD4	0.0023±0.0004	2.3±0.4	0.48±0.07

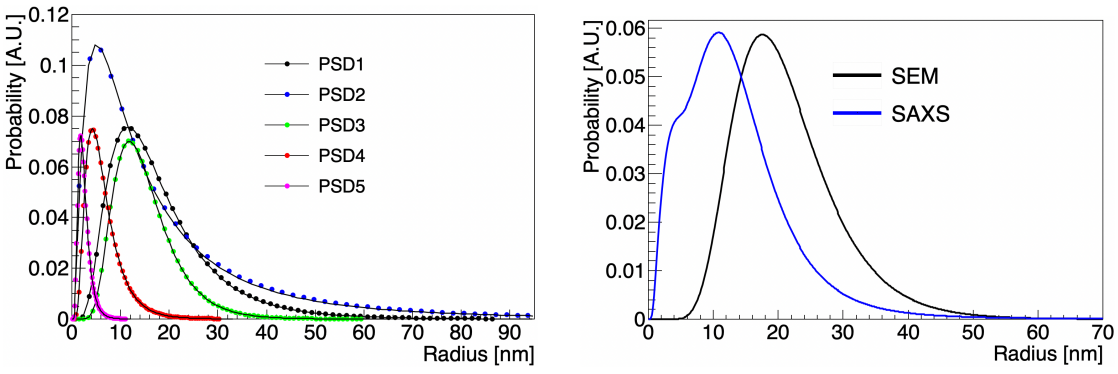

Figure 2.21: Particle size distribution of V nanopowder obtained by SAXS data. (left) Obtained by fitting when assuming five log-normal distributions, (right) blue line: Adding the five log-normal distributions obtained by Fit, black line : Analysis result of the SEM image.

2.4.5 Error of the dσ(q)/dΩ Estimated by SAXS Data

Next, we consider the error of the differential cross section calculated using the particle size distribution in Fig. 2.21. Since SAXS measurements only give the intensity ratio, the statistical error is estimated from the fluctuation from the fit line. The fluctuation of the ratio between the theoretical curve obtained from the fit and the measured data is shown in Fig. 2.22. Next, Fig. 2.23 shows the results of expressing each q value in Fig. 2.22 as a frequency distribution. The standard deviation of the frequency distribution in Fig. 2.23 obtained from the fit using Gaussian is $1\sigma = 0.26\,\%$. In other words, the accuracy of the theoretical scattering intensity calculated from the SAXS data is 0.26 %.

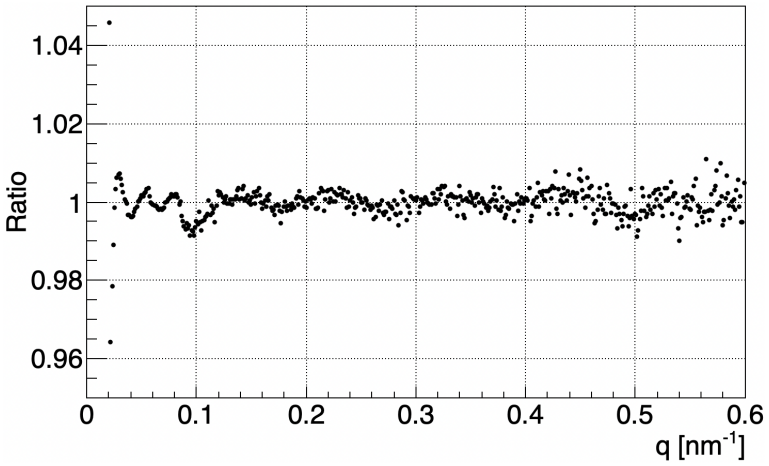

Figure 2.22: Ratio of the theoretical curves and five particle size distributions calculated from the SAXS data.

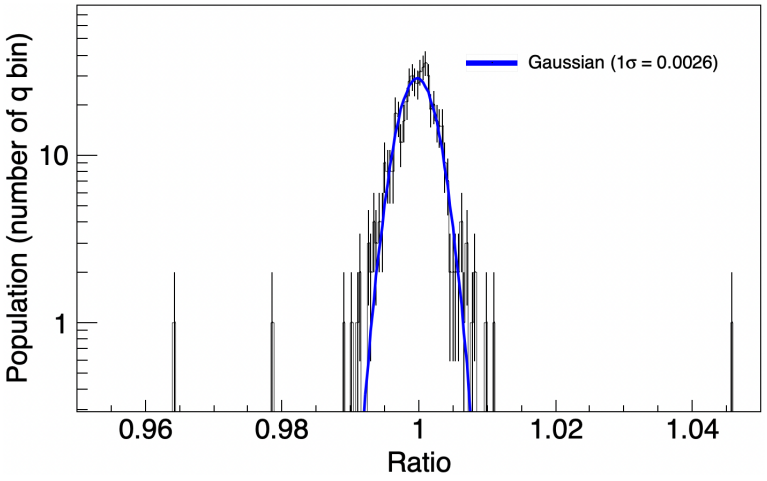

Figure 2.23: Frequency distribution of q based on the ratio of SAXS data to theoretical values

2.5 Test for the Synthesizing Nanoparticle of $Ni(OH)_2$

Chemical synthesis of nanoparticles does not require special equipment compared to other methods, so they can be created and tested relatively easily. The precipitation method (sol-gel method) for synthesizing nanoparticles is used for various substances. One way to reduce the average coherent nuclear scattering length of the nanoparticle target to zero using this method is to replace the elements of the compound with isotopes. One candidate for such a substance is nickel hydroxide. Natural nickel has a coherent nuclear scattering length of $+10.3\,\mathrm{fm}$, but the nickel isotope ^{62}Ni has a negative coherent nuclear scattering length of $-8.7\,\mathrm{fm}$. The coherent nuclear scattering length of a normal nickel hydroxide ($Ni(OH)_2$) is calculated to be $14.4 \pm 0.2\,\mathrm{fm}$ using the coherent nuclear scattering lengths of oxygen and hydrogen, $5.803 \pm 0.004\,\mathrm{fm}$ and $-3.7409 \pm 0.0011\,\mathrm{fm}$. On the other hand, the coherent nuclear scattering length of the $^{62}Ni(OH)_2$ can be calculated as $-4.6 \pm 0.3\,\mathrm{fm}$. Therefore, by producing nanoparticles by mixing $Ni(OH)_2$ and $^{62}Ni(OH)_2$ with the ratio of 0.76 : 0.24, the average coherent nuclear scattering length becomes zero. In principle, this method is rather easy having the material of enriched ^{62}Ni isotope. Nickel hydroxide was synthesized by adding sodium hydroxide dropwise to a stirred aqueous solution of nickel chloride, adjusting the pH by the amount of NaOH [40]. In the experiment, a colloidal solution of nickel hydroxide was even created, as shown in Fig. 2.24. But in real, the use of any nickel compound is restricted with the ordinance

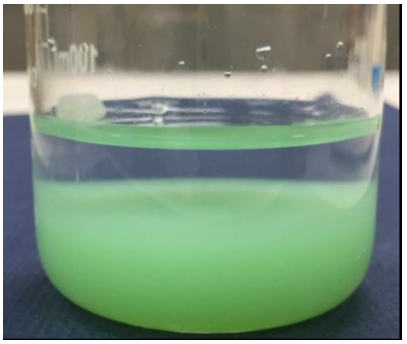

Figure 2.24: Colloidal solutions of nickel hydroxide prepared by chemical precipitation.

on prevention of hazards due to specified chemical substances, and thus it was very hard to be employed. It became necessary to create a prototype using a material that could be easily used in experiments using neutrons, so we changed to using a material that is used in neutron experiments, such as a V-Ni alloy.

2.6 Jet Milling Test

Still another method of creating nanopowder is so-called the "jet-mill" method. This method, classified as a break-down method, mechanically crushes bulk metals to create powder. The principle of a jet mill is shown in Fig. 2.25 (left). Those pieces are carried into the chamber by the jet stream of noble gas such as helium and collide with each other in the chamber to produce nanopowder by crushing. Since the pieces of the raw material are broken by collision with the same material, the risk of contamination is rather small, being the major advantage of this method.

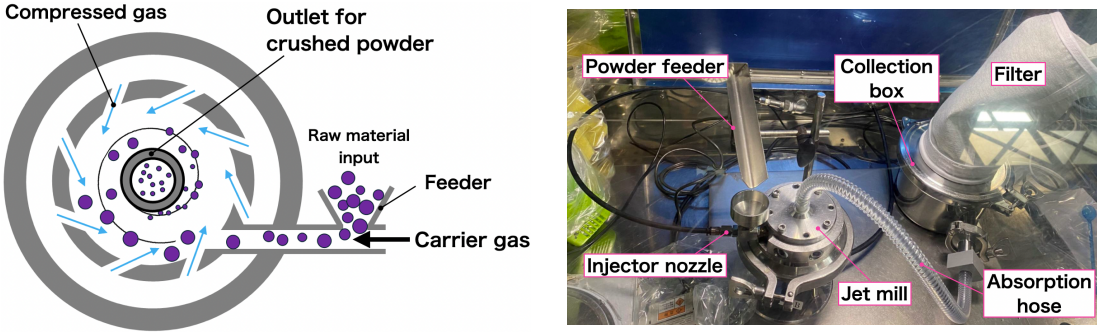

Figure 2.25: Jet mill grinding method and setup :(left) the grinding process inside the Jet mill and (right) set-up of prototype test

The raw materials used for the prototype tests were a V-Ni null matrix alloy, which is usually used for holders in neutron scattering experiments at the J-PARC/MLF, and a natural vanadium. The alloy was prepared with a Ni-4.9 wt.% mixture ratio, which has been reported to minimize the Bragg peak in neutron irradiation tests of alloys [41]. A foil with dimension of 0.25 mmt × 10 mm × 10 mm of V-Ni alloy (Taiyo Koko Co., Ltd., Japna) was prepared as the raw material as shown in Fig. 2.26. The composition ratio of the alloy at the time of production is shown in Table 2.15.

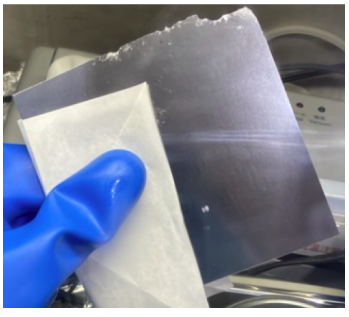

Figure 2.26: V-Ni alloy foil used as raw material

Table 2.15: Mass% composition ratio of each element in V-Ni alloy foil

	V	Ni	Al	Si	Fe	Mo	C	O	N
Foil#	Bal.	4.85	0.002	0.016	0.002	0.001	0.008	0.015	0.013

The $\bar{b}_{\mathrm{coh}}$ of V-Ni alloy foil calculated from the composition ratio is -0.09 fm. For the jet-mill process, the raw material should be prepared as granules with the diameter less than 0.5 mm. Therefore, the V-Ni alloy raw material was cut into small granules using a metal snip in a glove box, and classified using a sieve.

A production test was carried out by Aishin Nano Technologies Co., Ltd. using the jet-mill machine NJ-50 on May 26th and 27th, 2022. The flow-type glove box shown in Fig. 2.25 (right) was used for the test, and nitrogen gas was used as the carrier gas. An oxygen meter was used during the test, and the oxygen concentration was maintained at 0.0 ± 0.1 wt.%. The gas pressure was 2.0 MPa, and the internal pressure was adjusted from 0.5 to 1.5 MPa during testing. First, we tested the production of nanopowder using vanadium foil as the raw material, and found powder with a diameter of approximately 100 nm, as shown in Fig. 2.27 (left). Next, we proceeded with the production of nanopowder from a V-Ni alloy, but most of the particles were a few micrometers in size, as shown in Fig. 2.27 (right). Furthermore, elemental analysis using SEM-EDS revealed that when natural vana-

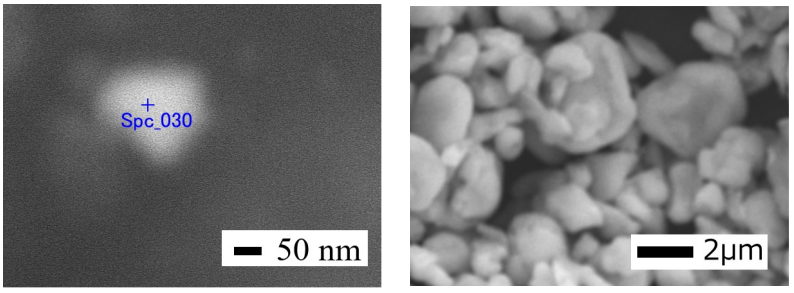

Figure 2.27: SEM images of samples after milling:(left) V and (right) V-Ni alloy

dium was used as the raw material, no metals other than V were detected, but when a V-Ni alloy raw material was used, a non-negligible amount of zirconium, approximately 30 wt.%, was present in the sample. Because V-Ni alloy is harder than pure vanadium, and the inner wall of the jet mill chamber also contains zirconium, it was thought that the V-Ni alloy pieces would collide not only with each other but also with the inner wall of the chamber, scraping off the wall and stripping away the zirconium. Even in the case of natural vanadium, a similar problem can occur if the milling time is extended in order to increase the sample recovery amount. For this reason, we did not use the jet mill method to produce samples to be used in actual neutron scattering measurements at J-PARC.

Chapter 3

Experimental Apparatus

This chapter introduces the J-PARC/MLF/BL05 (NOP beamline) where the SANS experiment was performed and details of the experimental equipment installed at the beamline. Benchmark experiments were performed to validate the accuracy of the proposed method against established existing experimental data.

First, an overview of the J-PARC facility is provided. In Sec. 3.4 and Sec. 3.5, experimental set-up and target cell of V nanopowder are explained. Detail and characteristics of the neutron detector used in this experiment are explained in Sec. 3.3 and Sec. 3.7. Measurement condition is explained in Sec. 3.6

3.1 J-PARC/MLF

At the Japan Proton Accelerator Research Complex (J-PARC), a proton beam is generated from the rapid cycling synchrotron (RCS) at a pulse repetition rate of 25 Hz and irradiated onto a mercury target in the center of the target station in the Materials and Life Science Experimental Facility (MLF) [42].

The proton beam generates neutrons through nuclear spallation reactions, and the proton beam is sent to the MR (Main Ring) at approximately 3 s during operation of the Neutrino Experimental Facility and approximately 6 s during operation of the Hadron Experimental Facility. During the MLF operation period from June 15 to 22, 2023, when the experiment was conducted, the MR cycle was 5.2 s, and the beam supply to the MLF was stopped for 200 ms. At this time, the proton beam power received by the J-PARC MLF was 750 kW.

In addition, the MLF provides three timing signals: a 12 MHz master clock signal, a

25 Hz timing signal generated by dividing the master clock signal and synchronized with the timing of the proton beam injection, and a kicker pulse signal that notifies the user that the proton beam has been injected into the MLF target. These signals are used for timing control of the device and time-of-flight analysis.

Most of the spallation neutrons are generated in the evaporation process of excited nuclei of several MeV. To obtain cold neutrons suitable for neutron scattering experiments, the neutron speed must be reduced. The neutrons pass through a light water premoderator and are then slowed down by a liquid hydrogen moderator. To investigate the structure of materials with high resolution and precision, a narrower and cleaner pulsed neutron beam is required, even if it sacrifices some intensity. There are three types of moderators. One is the Combined Moderator (CM), which is placed below the mercury target and provides a high intensity neutron pulse. The other two, the Separated Moderator (DM) and the Poison Separated Moderator (PM), are placed above the mercury target and provide a lower intensity but narrower neutron pulse. Each neutron beamline is equipped with a dedicated neutron beam shutter, allowing the neutron beam to be switched on and off during measurements and sample changes.

These moderators have the following characteristics:

- **Decoupled Moderator (DM)**
  The hydrogen moderator region is covered with a Ag-In-Cd alloy neutron absorber (decouper). By blocking neutrons that take a detour through the reflector, it is possible to extract pulsed neutrons with a narrow time width.

- **Poisoned decoupled Moderator (PM)**
  A poisoned cadmium plate is inserted in the hydrogen region from the DM. This allows for a narrower pulse width of neutrons than the DM, but the neutron intensity is also reduced.

- **Coupled Moderator (CM)**
  Neutron absorbers or plates are not used, and a high time-integrated intensity is obtained at the expense of a wider pulse width.

These neutrons are then simultaneously supplied to 21 of the 23 beamlines that will be in operation in 2024. A total of 23 neutron beams are extracted from the moderators: 11 beamlines (BL01–BL07 and BL14–BL17) from the CM, 6 beamlines (BL10–BL12, and BL21–BL22) from the DM and 6 beamlines (BL08 and BL18–BL20) from the PM.

3.2 BL05 NOP

In this section, the MLF/BL05(NOP) beamline used for the SANS experiments in this study is introduced.

The BL05 beamline was constructed as a beamline for fundamental physics research at MLF and is called "Neutron Optics and Physics (NOP)". This beamline uses a CM-type moderator to accommodate experiments requiring high statistics, and is equipped with a neutron (m = 2) supermirror guide and bender to efficiently transport cold neutrons ($E_n \leq 100\,\mathrm{meV}$) with long wavelengths suitable for fundamental physics experiments. A supermirror is a multilayer structure of two different materials deposited on a substrate. Neutron interference in the multilayer results in additional reflectivity beyond the critical velocity of the total reflection of monolayers, where the critical velocity is the maximum value of the velocity component normal to the mirror surface. The value m represents the neutron critical velocity of the supermirror and is defined as $m = v_c/v_{c,Ni}$, where v_c is the critical velocity of the supermirror and $v_{c,Ni} \approx 7\,\mathrm{m/s}$ is the critical velocity at the surface of nickel at natural abundance [43, 44].

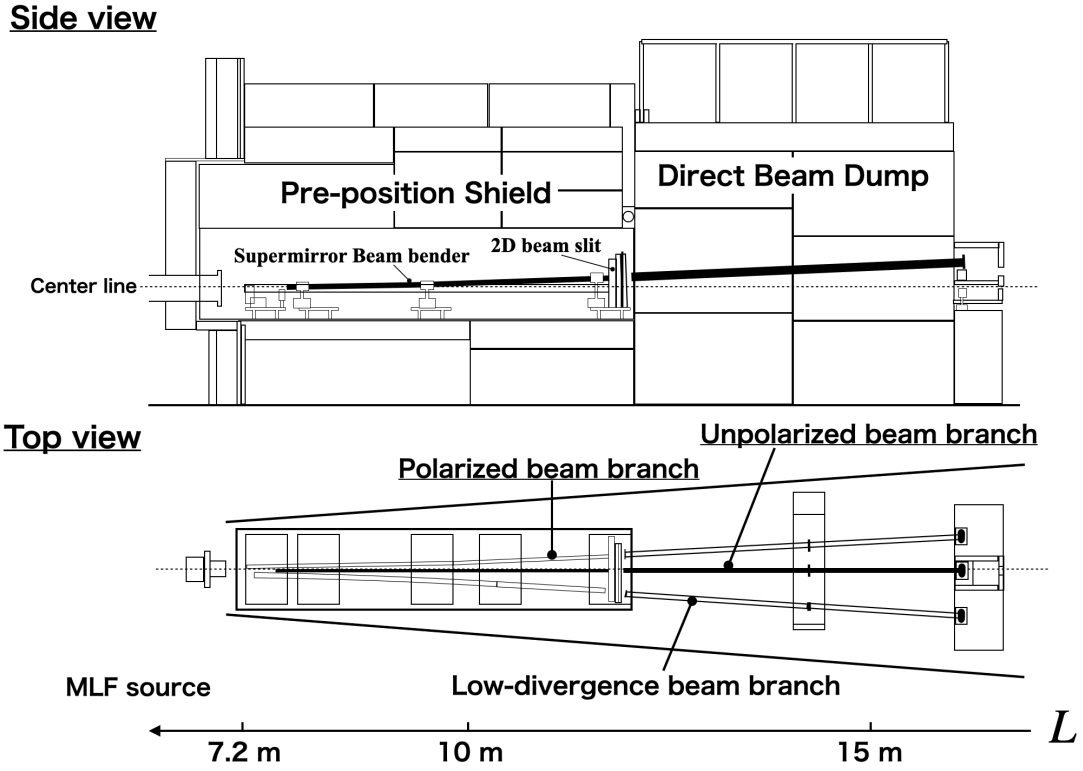

Figure 3.1: Schematic view of the configuration of the BL05 (NOP)

The schematic configuration of the BL05 (NOP) beamline is shown in Fig. 3.1. A beam shutter and a biological shield are in the regions of L = 2.3 m $\sim$ 4.3 m and L = 4.3 m $\sim$ 7.2 m, respectively, where L is the distance from the moderator. To reduce neutron loss during transport to the laboratory, a (m = 2) supermirror guide with inner dimensions of 100 mm(H) $\times$ 110 mm(W), length of 4.6 m, and neutron reflectivity of 90 % or more is placed L = 2.3 m away from the center of the moderator. The neutron beam is transported to the supermirror bender 0.8 m away from the exit of this guide, and distributed to three beam branches suitable for each experimental purpose. The inside of the beam bender is not a vacuum in order to achieve a dense design of upstream. Instead, the inside is filled with helium gas to reduce beam attenuation due to air scattering. Each branch has a four-quadrant slit with neutron absorbing plates located at L = 12 m directly below the bender, allowing the beam to be shaped to any size.

Each beam branches is called, Low-divergence branch, Unpolarized branch and Polarized branch from left when viewed from downstream of the beam. The characteristics of these beam ranches are as follows. The performance show in the Table 3.1.

- **Low-divergence branch**
  This branch is designed simply to minimize beam divergence and loss during transport. Neutrons slower than 1.2×10^3 m/s are transported to the target position, L = 16.2 m away, by two (m = 3) supermirrors offset by 1.9 degrees each. The beam intensity is 5×10^6 cm^{-2} at the exit. The beam divergence is 11 mrad(H) $\times$ 1.1 mrad(W) at L = 16.2 m when the four-quadrant slit is fully open.

- **Unpolarized branch**
  This branch was designed with the aim of transporting as many short wavelength neutrons as possible. The beam is directed 2.6 degrees above the horizontal by a circular arc beam bender with inner dimensions of 50 mm(H) $\times$ 40 mm(W), length of 4 m, and radius of 100 m. The bender is composed of (m = 3) supermirrors, and the inside is divided into five channels with inner dimensions of 10 mm(H) $\times$ 40 mm(W).

- **Polarized branch**
  A beam bender with a magnetic supermirror arranged in a channel shape to generate cold neutrons with spins polarized in one direction is used. Currently, a neutron lifetime measurement experiment is being carried out using a bunched VCN beam produced by a spin-flip chopper.

Neutrons transported from each branch pass through a four-quadrant slit at L = 12 m, then pass through a rectangular vacuum pipe with a length of 4.2 m, and are transported

Table 3.1: Summary of the performance of these beam branches[11]

Branch	Cross secction (X × Y mm)	Beam flux ($cm^{-2}s^{-1}$)	Beam Divergence (X × Y mrad)	Luminance ($cm^{-2}sr^{-1}s^{-1}$)	polarization
Unpolarized	50 × 40	$(3.8 \pm 0.3) \times 10^8$	(m = 2)	-	-
Polarized	120 × 60	$(4.0 \pm 0.3) \times 10^7$	23 × 9.4	$(1.8 \pm 0.1) \times 10^{11}$	94 – 96 %
Low-Divergence	80 × 40	$(5.4 \pm 0.5) \times 10^4$	0.23 × 0.23	$(1.0 \pm 0.1) \times 10^{12}$	-

to the experimental hall at L = 16.2 m. The inside of the vacuum guides of the unpolarized and low divergence branches are fitted with B_4C resin to cut the reflected neutrons which have larger divergence. The fast neutrons are absorbed by a direct beam dump located in the region of L = 12 m ∼ 16.2 m. Only the bent neutrons are transported downstream through a beam hole that passes through the beam dump. The inside of the vacuum pipe is constantly evacuated by a dry pump to prevent neutron loss due to scattering with air molecules, and the pressure is kept below 8 Pa.

3.2.1 Data Acquisition System

In order to analyze the momentum of neutrons due to elastic scattering, it is necessary to record the detection time and position information of the measured neutrons.

The data was acquired using the Nikiglass 16-Input PHA & LIST Module A3100 [45] and 760-PRU06PIK installed in the cabin of the BL05 beamline. The A3100 module is equipped with a memory for LIST and a memory for PHA measurement, and can simultaneously obtain LIST data and PHA measurement data for 16 parameter events. The A3100 is controlled by a business program running on LINUX.

The LIST measurement data is recorded on the PC for each event converted by the ADC for 0 to +10 V unipolar pulse input from 16 channels, with the following information recorded: index, input channel number, AD conversion value of the pulse height, clock time of the peak position, and inverted bit value.

The minimum rise time required for the input pulse is 200 ns and the minimum pulse width is 500 ns. The ADC gain resolution can be selected from the range of 256 to 8192 ch. In the actual measurement, the TSI (Time Stamp Information) mode function was selected to record the elapsed time from the start of the measurement to the time when the signal entered each channel. In addition, the clock time base can be selected in the range of 5 ns – 1 us. During measurement, the ADC gain resolution was set to 8192 ch and the clock time base was set to 1 us.

3.2.2 Signal and Time Information in LIST Data

The method for calculating the TOF of the measured neutrons is explained using a portion of the actual measurement data shown in Fig. 3.2.

The data file lists the results of measurements on each channel in the order they arrived

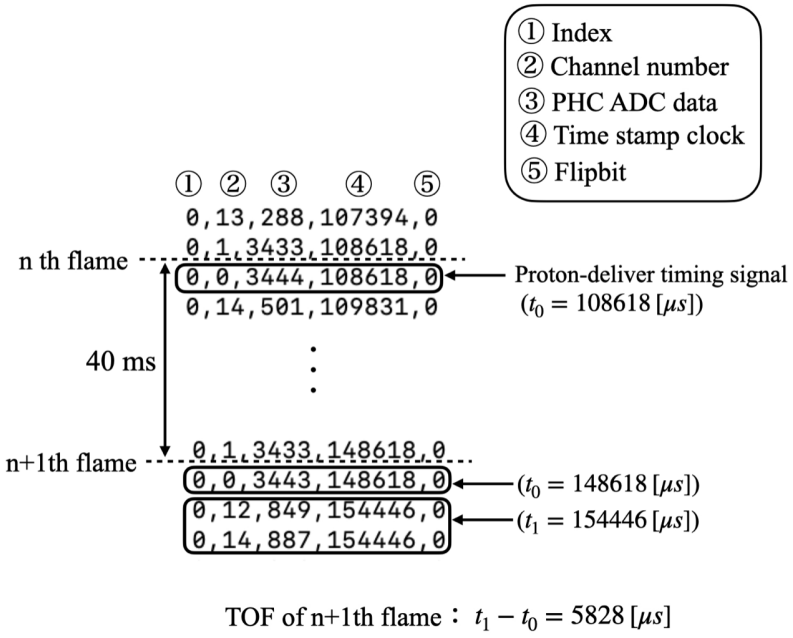

Figure 3.2: List data contents and TOF analysis.
t_0 represents the TOF time origin during analysis.

at the A3100. The first kicker pulse signal when the proton beam is incident on the mercury target after the start of measurement is recorded as the time origin of the clock number. The difference between the clock number of the subsequent detector signal and the time origin is taken and saved in memory along with the AD conversion value and the kicker pulse number up to this point. This operation continues until the next kicker pulse signal, which occurs at 25 Hz, arrives. When the next kicker pulse signal is received, the time origin is reset and the kicker pulse number is added. This operation is repeated until the end of the measurement. The speed of the measured neutrons can be determined from this time information and the distance from the moderator to the detector. To obtain the count rate per unit time, the maximum kicker pulse number is divided by the beam repetition period of 25 Hz to obtain the accumulated measurement time. This value is multiplied by all the measured events to obtain the count rate taking into account the beam stop time due to accelerator trouble, etc. How to obtain position information will be explained in Sec. 3.3.

3.3 Neutron Detector

A flange for connecting the neutron detector is attached to the rear end of the chamber. From Fig. 3.11, the distance from the target to the detector is 920 mm, so the scattering angle when a neutron is detected at a position x mm away from the center of the beam is $\theta \sim x/920$ rad.

In experiments before 2020, a 0.5 mmt aluminum window was installed at the rear end of the chamber, and the BL05's regular neutron detector (called the RPMT detector) was placed in the atmosphere for measurements. The degree of vacuum in the chamber is about a few Pa, so the aluminum window material needed to have a certain thickness so that it would not deform due to atmospheric pressure. As a result, the scattering data from the sample included scattering events caused by the aluminum window material. A neutron detector (called the FRP detector) that can operate in a vacuum environment without using an aluminum window in the beam path was newly introduced in 2020 by a collaborating member from Nagoya University. The RPMT and FRP are detectors that each consist of a two-dimensional readout circuit of a resistively divided photomultiplier tube (PMT) and a neutron scintillator. The position resolution of the RPMT detector and the FRP detector are shown in Table 3.2.

Table 3.2: Position resolution and sensitive area of FRP and RPMT detectors

	Position resolution	Range of detection
RPMT	$0.5 \sim 0.8$ mm	$\phi\,50$ mm
FRP	0.243 ± 0.005 mm	40×40 mm^2

3.3.1 Operating Principle of FRP Detector

The FRP detector was developed using a new general-purpose flat panel multi-anode PMT (H12700) after the production of the two types of PMTs R2486 and R3292 sold by Hamamatsu Photonics that were used in the RPMT was discontinued.

Figures 3.3 and 3.4 shows the appearance and configuration overview of the FRP detector. The diameter of the detector is 55 mm, and the effective detection area is 42 mm × 42 mm. The basic configuration is a light diffusion glass and a neutron scintillator placed on the photocathode of a Multi-Anode PMT (MA-PMT), which is then fixed in place with aluminum foil and insulating tape for light shielding. The dynode of

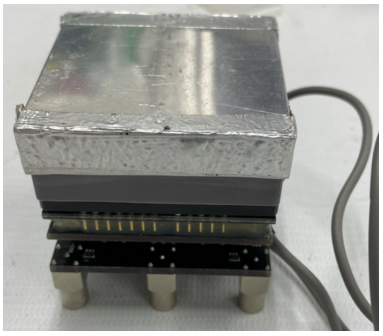

Figure 3.3: FRP detector

the MA-PMT of the FRP detector has a metal channel type electrode structure, and the photoelectrons emitted from the photocathode pass through many fine dynode channels (pathways for photoelectrons and secondary electrons) by the focusing mesh and reach the anode. At this time, the photoelectrons are amplified by 1.5×10^6 times (applied voltage: −1000 V) by the dynode[46]. The features of this structure include its small size and excellent time characteristics, as well as the low degree of diffusion of secondary electrons to adjacent dynode channels, so by combining it with a multi-anode, the incident position of light can be detected precisely.

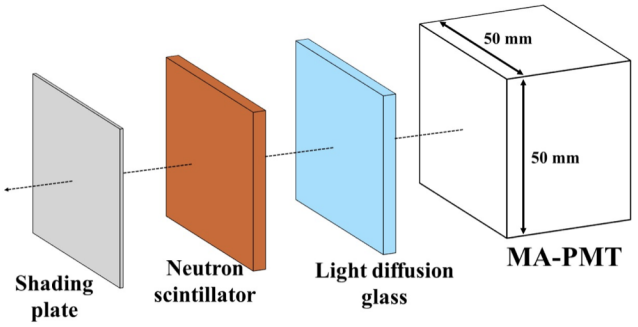

Figure 3.4: Configration of FRP detector

As shown in Fig. 3.5, the FRP uses a matrix-type multi-anode PMT with a total of $8 \times 8 = 64$ channels with a detection surface of 6 mm square.

Table 3.3 summarizes the characteristics of the H12700A.

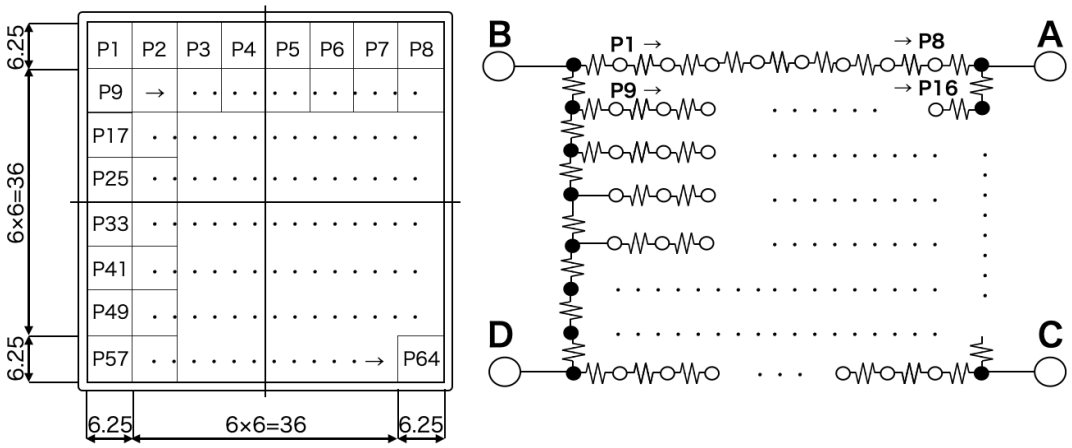

Figure 3.5: Anode structure and readout of FRP detector. (left) matrix type MA-PMT 64 ch anode (H12700A)[5]. (right) 64-channel resistor chain circuit diagram

Table 3.3: Hamamatsu Photonics H12700A catalog specifications

Number of channel	8×8
Dynode structure	Metal channel
Number of dynode stages	10
Photocathode material	Bialkali
Maximum supply voltage	-1000 V
Quantum efficiency	33 %
Amplification factor(Maximum supply voltage)	1.5×10^6
Pulse linearity per channel [2 % deviation]	0.8 mA
Response of rise time	0.52 ns
Response of transit time	4.9 ns

Each anode channel is connected with a resistor chain circuit, and the outputs of 64 channels are aggregated into four, A, B, C, and D. The scintillator light is received on multiple channels using the Anger method Eq. (3.1), and the position where the neutron arrives is determined by calculating the center of gravity of the charge from the ratio of the wave light obtained simultaneously within 1 µs of the total four signal outputs.

$$X = \frac{(B+D)}{(A+B+C+D)}, \quad Y = \frac{(C+D)}{(A+B+C+D)}, \tag{3.1}$$

In the Anger method, the scintillator light is intentinally diffused in each pixel-type PMT and incident on multiple pixels, and the amount of incident light is averaged to improve the accuracy of the detection position. A 2.35 mmt thick borosilicate glass was placed on the photocathode of the PMT as light diffusion glass, as shown in Fig. 3.8. Borosilicate glass contains about 12 % boron, which has an absorption cross section of 767 b for thermal neutrons, and therefore has the effect of absorbing neutrons that pass through the neutron scintillato. Figure 3.6 shows the wiring diagram for the FRP detector.

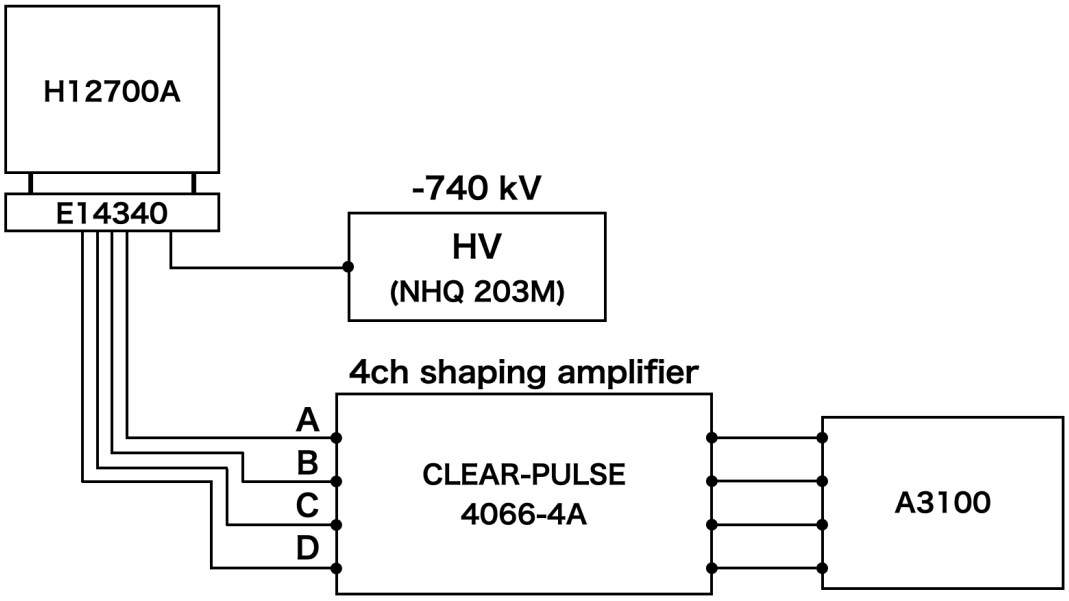

Figure 3.6: Data collection equipment and wiring diagram for FRP detector

3.3.2 Operating Principle of RPMT Detector

As another detector,the resistively divided two-dimensional detector (RPMT [47]) owned by MLF/BL05 was used.

The RPMT was used to measure the neutron detection efficiency of the scintillator used in the FRP detector and to evaluate the effect of the light diffusion glass. The RPMT is a two-dimensional detector based on the photomultiplier tube R3392 manufactured by Hamamatsu Photonics. The diameter of the detector is 127 mm, and the effective detection surface is 90 mm. The configuration of the RPMT detector is shown in Fig. 3.7. The electron amplification mechanism of the R3392 has 12-stage course mesh type dynodes, and the photoelectrons amplified by the secondary electron emission at the dynodes are diffused to 28 cross-wire anodes installed in each of the X and Y directions. The center of gravity position is determined by the charge division method from the pulse height ratio of the output charge, as with the FRP detector. The data collector and wiring diagram used were the same as those of the FRP.

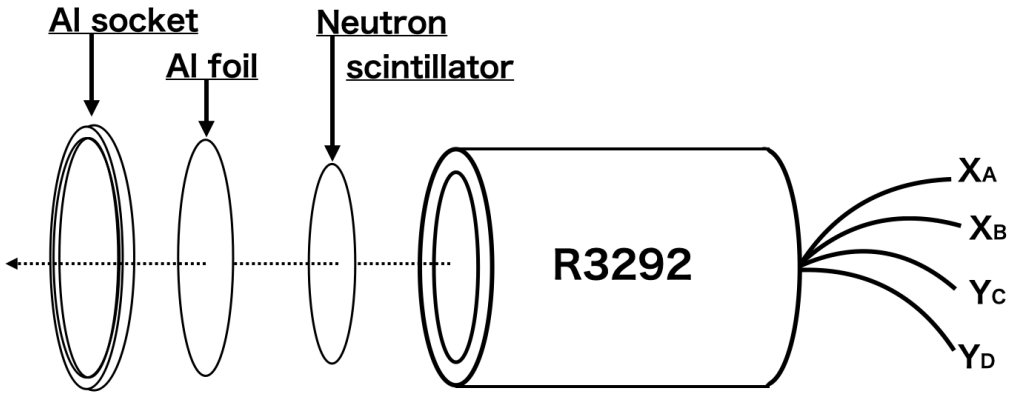

Figure 3.7: Configration of RPMT detector

To calculate the X and Y positions from four channels, use the following Eq. (3.2).

$$X = \frac{X_A}{X_A + X_B}, \quad Y = \frac{Y_D}{(Y_C + Y_D)}, \tag{3.2}$$

3.3.3 Neutron Scintillator

Neutrons doesn't have an electric charge, so they no ability to ionize. Therefore, charged particle obtained by nuclear reactions are used to measurement cold neutrons. The neutron converter used in the both detector of RPMT and FRP uses a scintillator made of ZnS doped with ^{6}LiF. The thermal neutron capture cross section of ^{6}LiF is 940 b, and the reaction formula is shown below.

$$n + {}^6\mathrm{Li} \longrightarrow \alpha + {}^3\mathrm{H} + 4.79\ \mathrm{MeV}, \tag{3.3}$$

The ^{6}Li(n, α)^{3}H reaction releases α paticles (2.06 MeV) and emits scintillation light. The theoretical yield of alpha rays when using ZnS is 10000 phtons per MeV, which is a strong emission intensity, and ZnS is not sensitive to Compton electrons associated with gamma ray rensitivity as a scintillator.

Similar scintillators are used for FRP and RPMT, and AST's scintillator with a thickness of 0.45 mmt and a content ratio of ^{6}LiF : ZnS = 1 : 2 is used. This ZnS-LiF plate is placed on the borosilicate glass as neutron scintillator, as shown Fig. 3.9. An aluminum light shield is placed on top of the ZnS-LiF plate and gap is wrapped with black plastic tape.

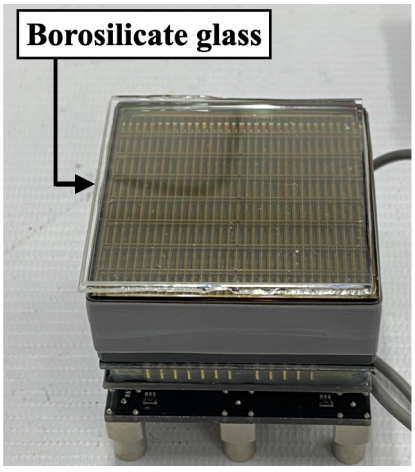

Fig 3.8: Borosilicate glass on PMT

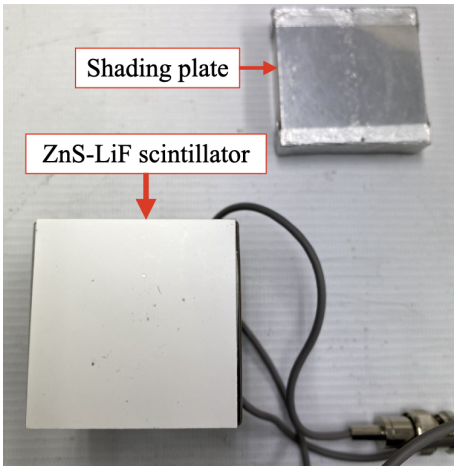

Fig 3.9: ZnS-LiF scintillator and Shading plate

3.4 SANS Setup

In a SANS experiment, a parallel beam must be formed to define the scattering angle, and the beam divergence angle must be kept as small as possible. For this reason, the low divergence beam branch of BL05 was used.

For the beam slit conditions, a line-collimator was used to increase the incident neutron intensity, anticipating a reduction in scattering intensity due to the nanoparticle target. As shown in Fig. 3.10, three line-slits are used on the beam axis. A parallel beam is formed using the 2D beam slit of the low divergence beam branch and two Cd line collimators.

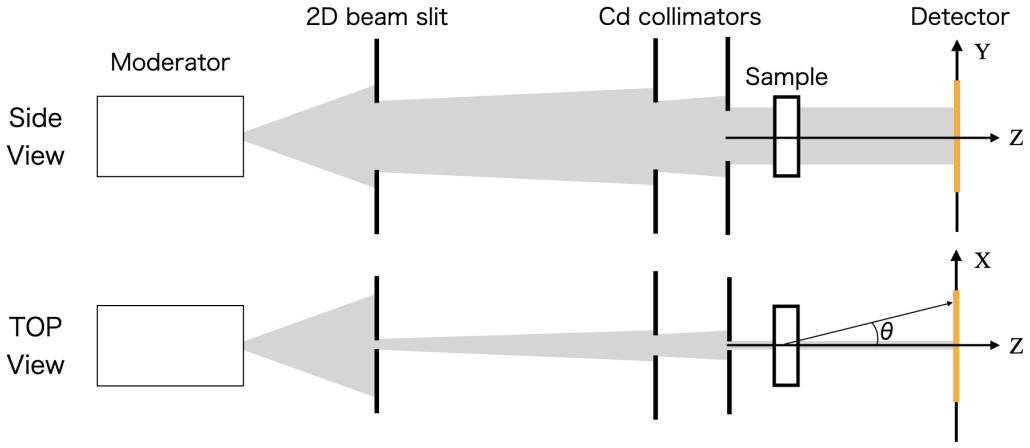

Figure 3.10: Schematic diagram of Line-Collimator setup

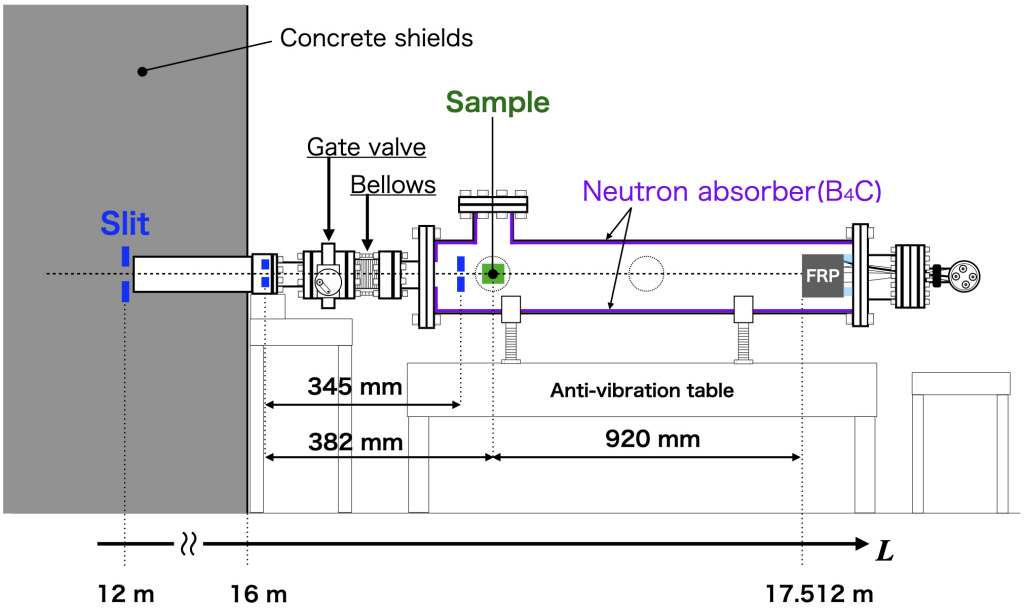

Figure 3.11: SANS setup in the BL05(NOP) beamline

When a Line-collimator is used, the incident neutron intensity can be increased by the amount that a rectangular beam is formed and spreads in the Y direction. In the X direction, the beam width is collimated to about 1 mm, and the momentum transfer distribution is calculated by calculating the angle of the neutrons scattered in the X direction from the center of the beam. However, since the scattering angle cannot be defined from the radial distance from the beam neutral as in the case of a normal pine hole collimator, the calculation of the solid angle from the detection surface becomes complicated. The setup is outlined in Fig. 3.11. The vacuum chamber for SANS is connected to the rectangular vacuum pipe that extends from the moderator to the L = 16.2 m point. The length of the vacuum chamber is about 1.5 m. At the end of the low divergence beam branch, a Pb block with a $25 \times 15\,\mathrm{mm}^2$ hole is placed. Transported neutrons pass through the hole. The beam port is shown in Fig. 3.12.

3.4.1 1st Cd collimator

The first Cd collimator is mounted on the beam port to form a parallel beam. The 1st collimator has a $2 \times 10\,\mathrm{mm}^2$ beam hole and is made of a 1mm thick Cd plate. The mounting position of the 1st collimator was adjusted using a laser that indicates the beam center position. The 1st Collimator is shown in the Fig. 3.13. On the back of the 1st Cd collimator, B_4C resin is attached to the top and bottom ends to provide space for evacuation between the Pb block.

A manual UHV gate valve is connected to the square flange using an ICF144 conversion

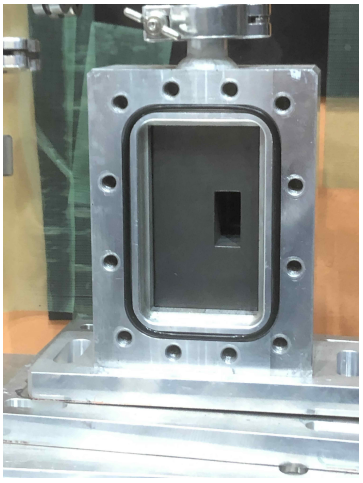

Fig 3.12: Beam port of low-divergence branch

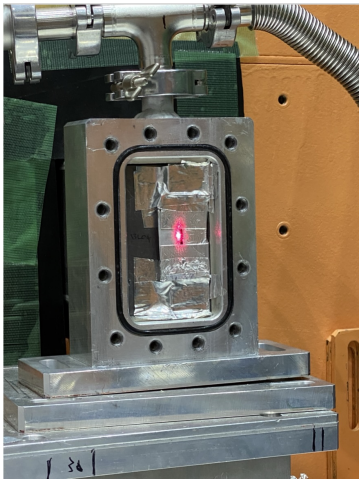

Fig 3.13: Attached 1st Cd collimator on the beam port

nipple, and the VF150 flange for connecting the chamber is connected using a bellows as a

joint. Shown in Fig. 3.14 after nipple connection. The bellows are used to adjust the beam center to the center of the connected detector, since the port hole of the Pb block is to the right of the center of the vacuum pipe when viewed from the downstream side. A 1100 mm wide vacuum chamber as shown in Fig. 3.15 is mounted on the VF150 flange. The inner

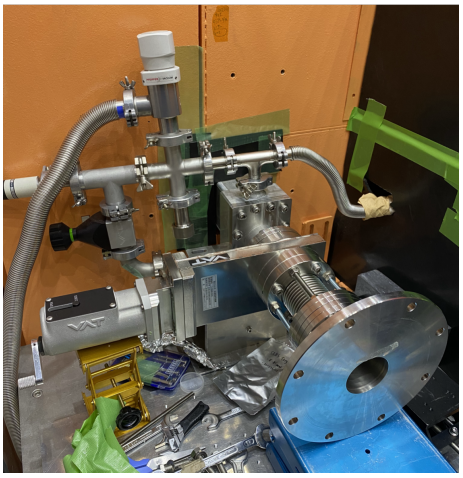

Figure 3.14: Bellows type expansion joint after nipple connector

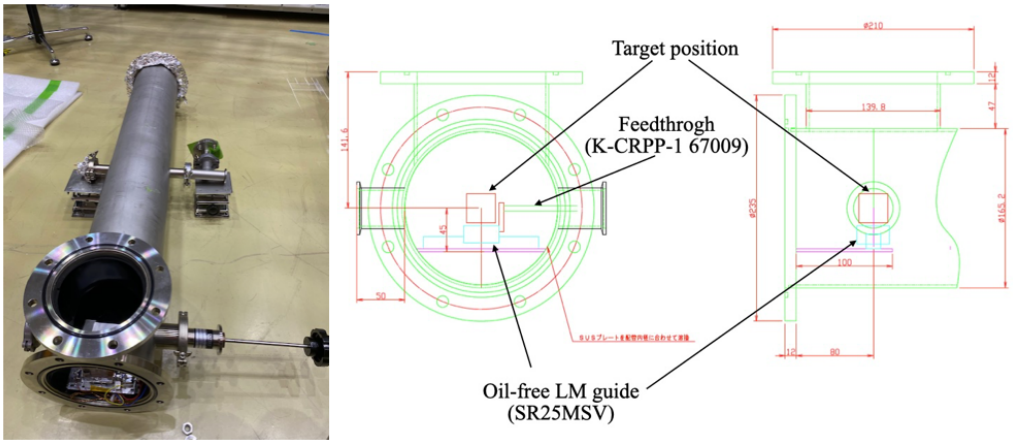

Figure 3.15: Target position in Vacuum chamber[6]

wall of the chamber is wrapped with a 3 mmt thick B_4C resin to prevent scattered neutrons from being scattered again and becoming a BG source. Inside the chamber, there is a 2nd Cd collimator for parallel beam formation and a platform for mounting the target. The chamber is equipped with a jig for fixing the target. A 100 mm × 127 mm SUS plate is welded to the connection of the chamber, and an oil-free LM guide is fixed with an M3 screw. The LM guide (K-CRPP-1 67009) can be moved horizontally even when the chamber is in a vacuum state thanks to the NW40 standard feedthrough (SR25MSV) on the side of the chamber.

3.4.2 2nd Cd collimator

The 2nd Collimator is 37 mm away from the target. The 2nd Cd collimator is a 40 mm × 50 mm × 1 mmt Cd plate with a $1 \times 8\,\mathrm{mm}^2$ hole for the incident neutron beam in the center and tapped holes at the four corners for fixing with screws. The 2nd Cd slit is fixed to a simple motorized linear stage that can be integrated into this chamber. Figures 3.16 and 3.17 show the drive mechanism and its scheme. An L-frame slit support plate is fixed

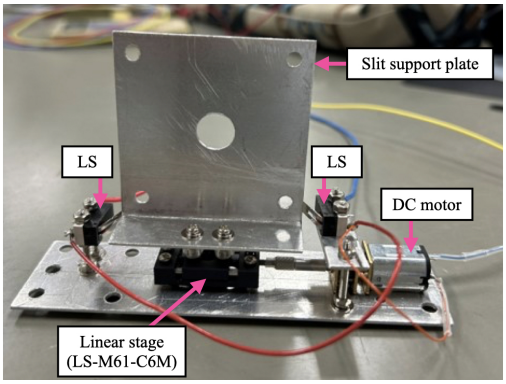

Fig 3.16: Slit drive mechanism

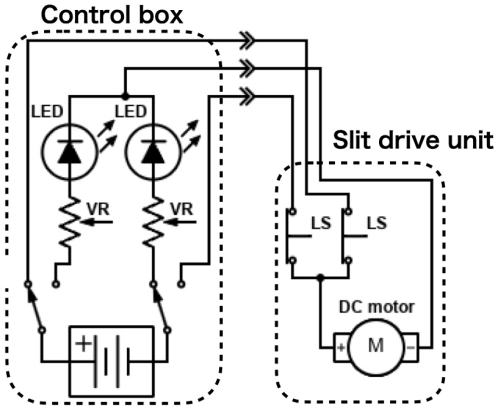

Fig 3.17: Scheme of Slit drive mechanism

to the linear stage (LS-M61-C6M) to fix the 2nd Cd slit perpendicular to the beam axis.

The position of the slit support plate is changed by rotating the rotation axis of the linear stage connected to a DC motor with a heat shrink tube. The DC motor can also be moved in the opposite direction by reversing the polarity of the current sent to it, which is used for beam alignment adjustments. A wiring that connects the lead wire and enamel wire so that it can be used in a vacuum environment is extended to a port in the center of the chamber, and is connected to the control box via a VF20-NW25 conversion nipple with a current input terminal so that it can be operated from outside the chamber. Power is supplied to the DC motor using an interval generator via a LEMO cable, which sends voltage pulses only for a preset time width to adjust the position of the linear stage. In addition, Limit Switch (LS) is attached to both ends of the slit support plate, which automatically cuts off the power supply when the range of motion of the linear stage is exceeded. Figures 3.18 and 3.19 show these slit mechanisms attached to the chamber.

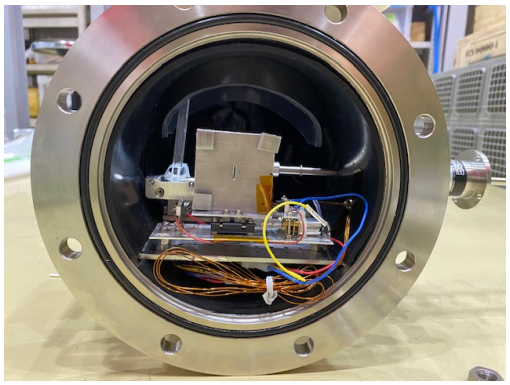

Fig 3.18: 2nd Cd collimator in the vacuum chamber

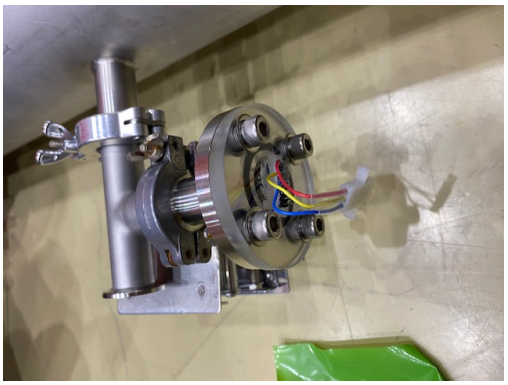

Fig 3.19: Current input terminal for DC motor

3.4.3 Insulation Measures in a Vacuum Environment

The operation of the FRP detector in a vacuum environment has been checked and verified by our previous collaborators by taking sufficient insulation measures [7]. To fix the FRP detector in the center of the chamber as shown in Fig. 3.20, an acrylic jig is used to attach it to the flange that holds the FRP detector. Polycarbonate screws are used to connect to the flange to seal the vacuum and not interfere with exhaust. The wiring is connected with a feedthrough between the SHV cable and the LEMO cable using a VF150-ICF152-NW40 conversion nipple. An insulating O-ring is used between the ICF152 and NW40 to isolate the vacuum chamber from GND. Figure 3.21 shows the setup with the FRP detector connected to the chamber. If the chamber is evacuated while a high voltage is applied to the FRP detector, discharge may occur due to the influence of air molecules remaining on the detector's substrate, so the voltage is applied at a vacuum level of about 100 Pa.

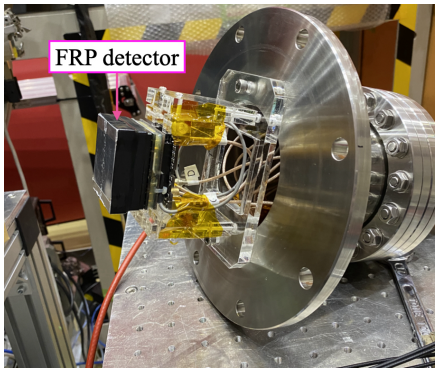

Fig 3.20: Setup for electrical insulation

Fig 3.21: Chamber with FRP detector

3.5 Target Cell for Nanoparticle Sample

Vanadium nanoparticles are a substance that easily reacts with oxygen in the air, and it is necessary to avoid a change in the nuclear scattering cross section due to oxidation.

The sample holder used for packing the nanoparticles was created with a structure that can be sealed with an O-ring of butyl rubber, as shown in Fig. 3.22.

The size of the sample holder is 48 mm × 42.8 mm × 23.8 mm. The powder samples

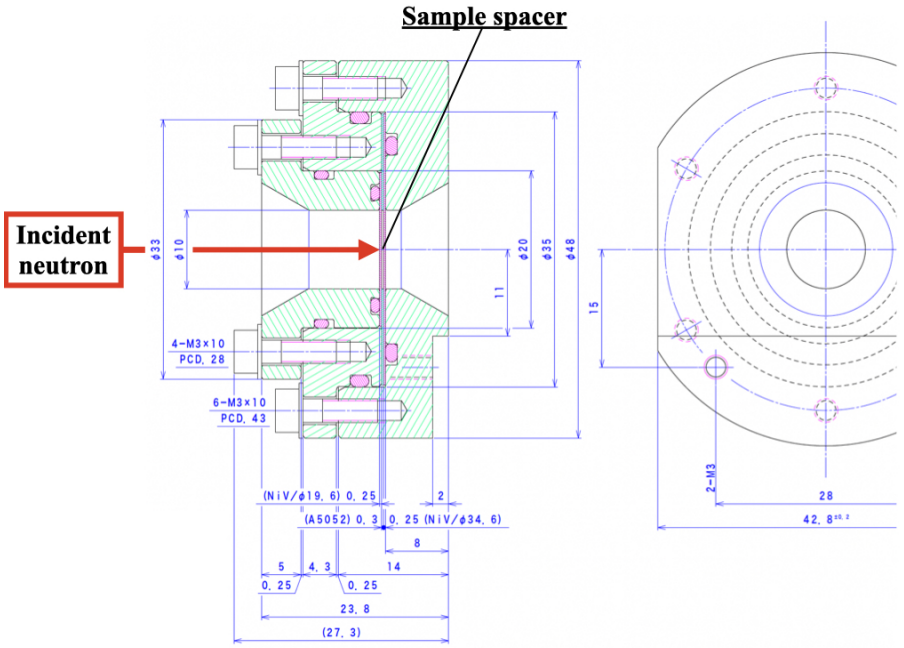

Figure 3.22: Sample holder

are packed into aluminum sample spacers with a thickness of 0.3 mm and a hole with a diameter of 10 mm. The encapsulated nanoparticles are held in place by the upper and lower windows. The windows are sealed by an aluminum frame with an O-ring and a through-hole M3 screw to prevent loosening even when vacuumed. The window material was used the V-Ni alloy foil described in Fig. 2.26. The window through which the neutrons enter consists of two V-Ni alloy foils with a thickness of 0.25 mmt and Ni content of 4.85 wt.%. The windows with diameters of ϕ19.6 mm and ϕ34.6 mm are used. The larger ϕ34.6 mm window is fixed in the aluminum frame before the powder is injected. After the powder is injected, a window of ϕ19.6 mm holds the powder and seals it. The size of the sample holder is specially designed to fit the SANS experimental chamber, as shown in Fig. 3.23.

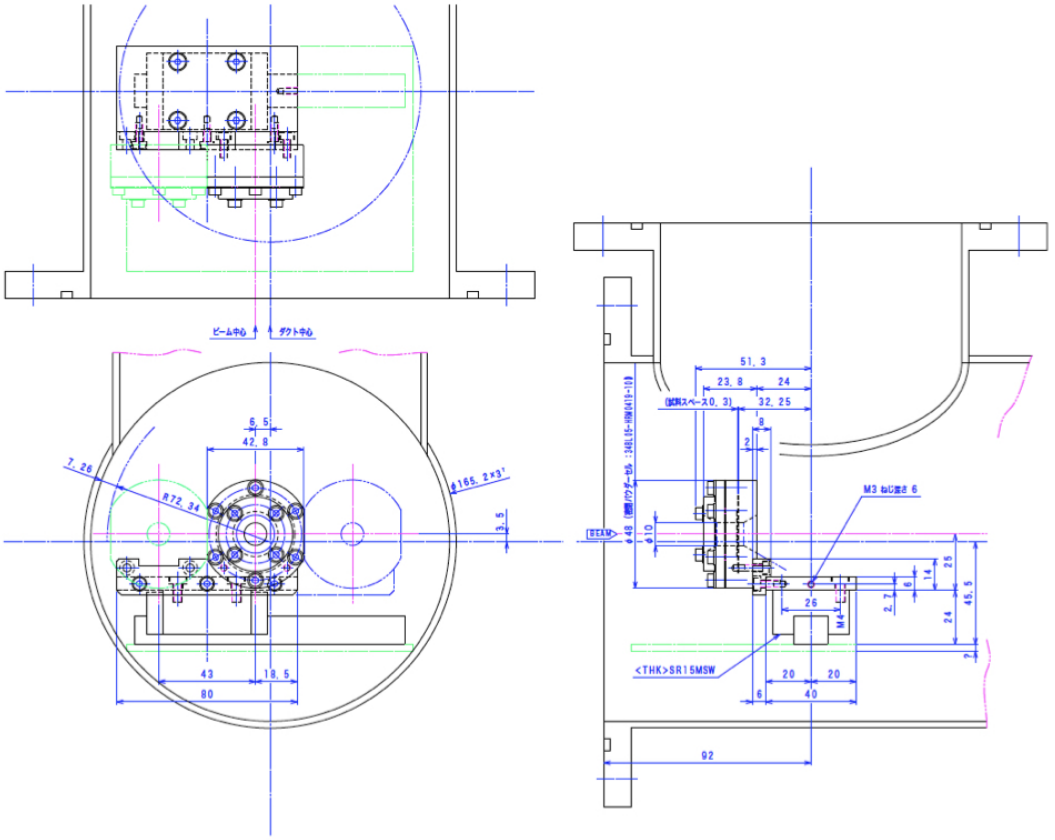

Figure 3.23: Diagram of sample holder placement in chamber

The two sample holders can be screwed to the LM guides in the chamber, and the feedthrough allows the beam axis to be adjusted to the center of each sample. To confirm the reduction in scattering intensity due to the V-Ni window material used in this sealed holder, we measured the scattering intensity due to the window material using the same SANS setup at the MLF/BL05 beamline in June 2022. To compare the scattering intensity, we also measured the sample holders with two 0.2 mm-thick aluminum windows used in the past. Figure 3.24 shows each sample holder. Figure 3.25 shows the results of comparing the angular distribution of scattered neutrons using an FRP detector. The integrated scattering intensity normalized by the sample thickness showed that the use of the V-Ni window material reduced the background from the sample cell by a factor of about 5.2.

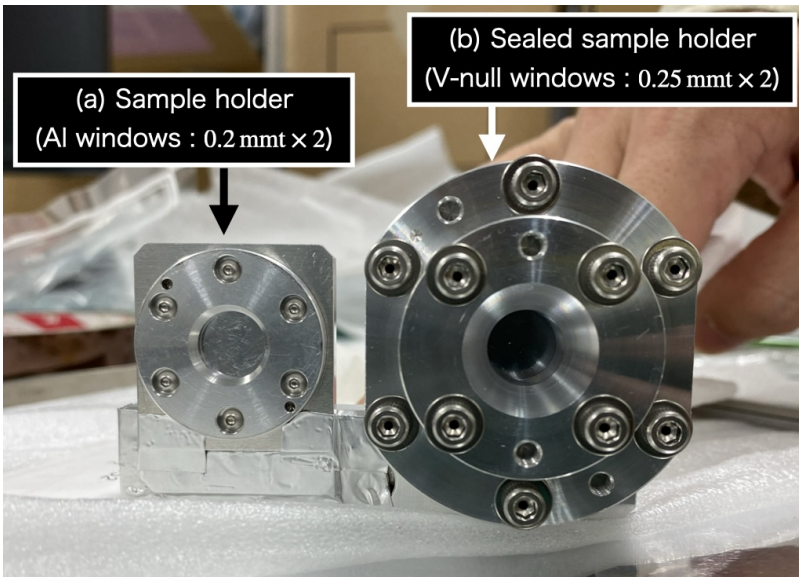

Figure 3.24: Sample holder. (a) picture of previous sample holder used the Al windows. (b) picture of sealed sample holder using V-null windows.

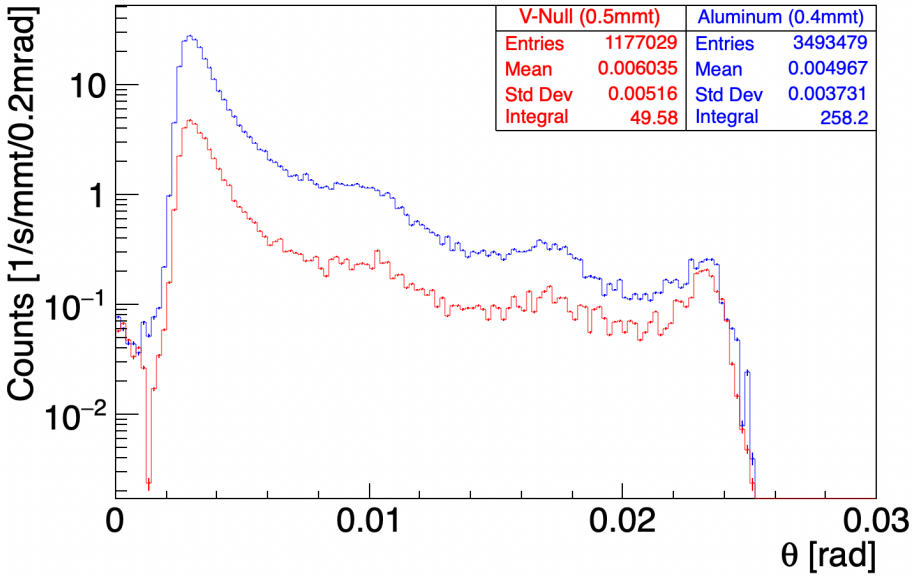

Figure 3.25: Angle distribution of scattered neutron by the sample holder (normalyzed by the sample thickness). (blue line) Aluminum window of old holder, (red line) V-null window of new holder.

3.5.1 Fabrication of Sample Cell

The vanadium nanoparticles were packed into the sample holder in a vacuum glove box filled with Ar gas. The glove box was used a UNICO UN-650F, located at the West Laboratory of the Research Center for Nuclear Physics (RCNP). Figure 3.26 shows in the vacuum glove box. The inside of the main box was evacuated with a rotary pump

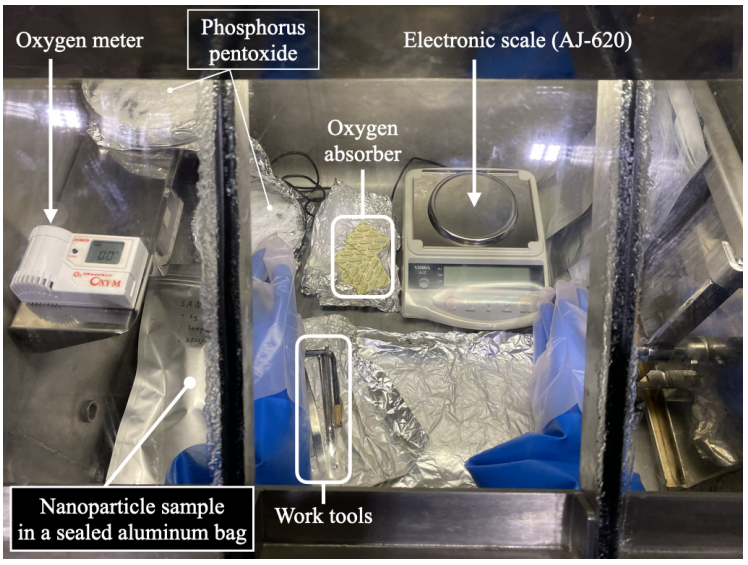

Figure 3.26: Work space in the Main box

beforehand, and then replaced with high-purity Ar gas (6N).

The tools were evacuated to a vacuum level of less than 0.001 MPa through a pass box equipped with a Bourdon tube vacuum gauge, and then replaced with Ar gas and moved to the main box filled with Ar gas. The vacuuming and replacement with Ar gas were repeated three times to remove moisture from the surfaces of the tools before moving them to the main box. An oxygen analyzer was also placed in the main box to check for leaks during the work. The oxygen concentration meter used was the OXY-1-M manufactured by JIKCO Co., Ltd. The resolution of the oxygen concentration meter is 0.1 wt.%. As this meter is not guaranteed to operate in a vacuum environment, the inside of the pass box was replaced with flow replacement before being moved to the main box. The amount of air flowing in by flow replacement was adjusted to about 30 min by adjusting the flow rate of Ar gas to 7 L/min for the volume of the pass box V = 17 L. The air density at this time is about 4 ppm. To prevent moisture from adhering to the nanoparticle sample in the atmosphere, a petri dish containing phosphorus pentoxide was placed in the main box together with the tools, and dehydrated overnight. The work was carried out within a dew point of -38.0 ± 2.0 Cdp.

3.5.2 Powder Filling Weight Measurement

An electronic scale was used to measure the powder filling amount. The electronic scales used were the GR120 made by A&D and the AJ -620 made by Shinko Denshi Co., Ltd., but the powder filling weight was determined using the GR120, which has better measurement accuracy. The minimum display of each is 0.1 mg and 1.0 mg. The AJ -620 was used to check the weight of the powder in the main box. The AJ -620 is not guaranteed to work in a vacuum environment, but it has been confirmed that there is no problem with mass measurement in a vacuum environment, so it was used in the main box after evacuation through the pass box.

The weight of the powder packed into the sample holder was determined in the following steps.

(1) Weigh the empty sample holder in air using the GR120.

(2) Place an empty sample holder in the pass box, evacuate, and then fill the pass box with Ar gas. Then move the empty sample holder into the main box.

(3) Check the dew point inside the main box, pack the nanoparticles into the sample holder and weigh sample holder with AJ-620.

(4) Fill the powder into the sample holder and seal the inside of the sample holder using the M3 screws and the holder flange.

(5) The sample holder is moved to a pass box and removed into the atmosphere.

(6) The weight of the sample holder with the powder inside is measured using the GR120.

(7) The sample holder containing the powder is sealed in Al bag with an oxygen absorber.

After confirming that the oxygen concentration in the atmosphere was 0.0 %, the glass bottle containing the sample powder was removed from the sealed aluminum bag. The sample nanoparticles in the bottle were sealed in the sample holder whose weight had been measured using a dispensing spoon as shown in Fig. 3.27(a). The sample powder is placed on the spacer in the sample holder, the powder is light pressed to flatten it using a V-null window material. This process was repeated until the powder was uniformly flat so that the V-null window material on the bottom was no longer visible as shown in Fig. 3.27(b). Next, the sample holder is weighed three using the AJ-620. After that, the sample holder is sealed in a grove box with a special flange.

The sealed sample hoder is transferred to a pass box and taken out into the air. The weight of the holder is then measured three times using GR120. The sample holder is then transferred back to the main box via the pass box and placed in a zip-lock aluminum bag containing the sample as shown in Fig. 3.27(d) is sealed in the air using a heat sealer. The results of the weight measurement of the sample powder at this time are summarized in Table 3.4.

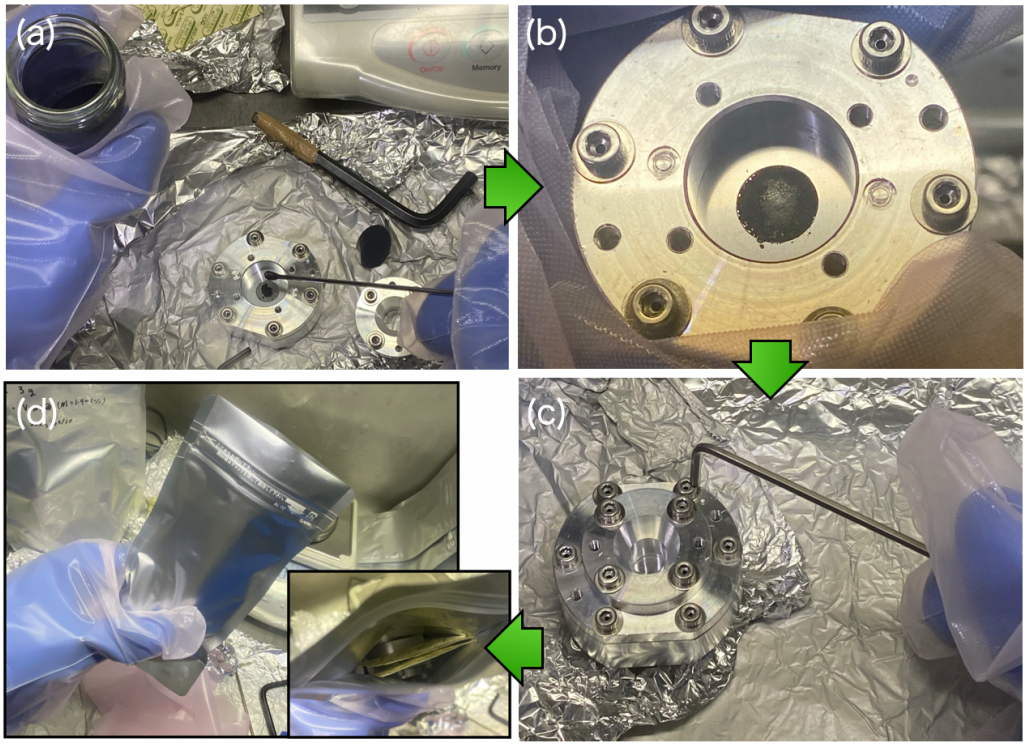

Figure 3.27: Fabrication of V-nano sample cell.(a) Filling the V nanoparticle in the cell, (b) After pressing with window material, (c) Sealed with cover parts, (d) Store in an aluminum bag with an oxygen absorber

Table 3.4: weight of Empty and filled sample holder measured by GR120

	1st time	2nd time	3rd time	Average
Empty cell	95.4563 g	95.4561 g	95.4562 g	95.4562 g
Filled powder	95.4716 g	95.4720 g	95.4718 g	95.4718 g
V nanopowder	-	-	-	15.6 ± 0.1 mg

3.6 Alignment for Measurement

This chapter describes the beam alignment method and setup for scattered and transmitted neutron measurements in SANS measurements. The incident neutron intensity adjustment method is explained in Sec. 3.6.1. The incident and transmitted neutron intensity measurement method is explained in Sec. 3.6.2. The scattered neutron measurement method is also explained in Sec. 3.6.3.

3.6.1 Method of Beam Alingment

To set the beam conditions with low beam divergence without compromising the injected neutron intensity, it is necessary to perform beam alignment for the assembled setup.

As shown in Fig. 3.11, three vertical line-collimators were placed in this SANS experiment. From the upstream side, there is a 2D beam slit, a 1st Cd Collimator, and a 2nd Cd Collimator. The alignment method is to first set the arrangement conditions of the 1st Cd Collimator and the 2D beam slit. The arrangement of the collimators is determined based on the 1st Cd Collimator. The 1st Cd Collimator was placed on the central axis of the low divergence beam port using a laser installed in the BL05 beamline. The 1st Cd Collimator is directly attached to the lead block at the beam port, so its arrangement cannot be adjusted. Instead, the 2D beam slit was adjusted to set the conditions for the two passes. The most upstream 2D beam slit is a four-quadrant variable slit with B4C beam shaping slits as shown in Fig. 3.28, and the vertical and horizontal widths and placement positions can be set by remote control from the BL05 cabin.

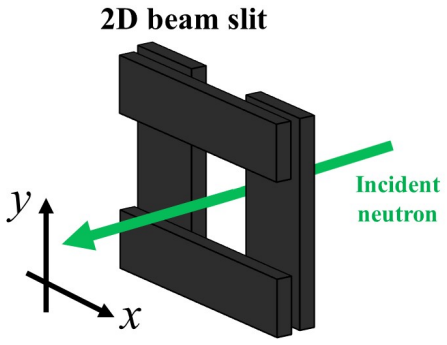

Figure 3.28: Schematic of 2D beam slit(adjust the upper left and right width to collimate the beam)

The collimation size of the 2D beam slit was set to 10 mm(H) × 1 mm(W), and the height and horizontal position of the beam center position were set to 44.000 mm and 21.500 mm, respectively. The 2nd Cd Collimator passes the laser from the most downstream of the chamber and places the center of the collimator hole on the light axis. The placement is then fine-tuned by the slit motor drive mechanism. The slit motor drive mechanism supplies power to the motor at regular intervals by the NIM pulse generator, allowing the slit to be remotely operated in the horizontal direction of the beam axis. The placement conditions were set so that the beam would be less widened and the beam intensity would not be impaired based on the two-dimensional distribution data measured by the actual neutron beam using the FRP detector.

3.6.2 Pile-up Suppression Techniques for the Measurement System

When measuring incident neutrons, counting losses occur when the scintillation light emission time constant or the DAQ circuit measures a large number of neutrons at once. The effect of pile-ups occurring in the FRP detector or DAQ system was studied by a collaborator at MLF/BL05 in 2020[7], reporting a dead time of $12.5 \pm 0.2\,\mu$s. It was also proven that the effect is negligible if the counting rate is less than 3 kcps.

To prevent overcounting in the detector, the 2D beam slit width is divided into five parts to measure the number of incident neutrons. As shown in Fig. 3.29, the width 10 mm in the Y direction is divided into five parts with a size of 2 mm × 1 mm, and measurements are taken while shifting the beam center by 2 mm each time.

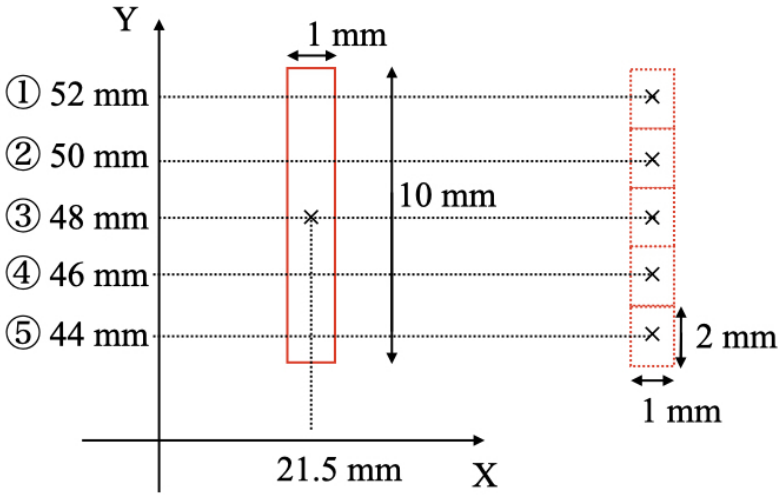

Figure 3.29: 2D beam slit divided into 5 parts for measurement of incident and transmitted neutrons

3.6.3 Method of Measuring Scattered Neutron

When measuring scattered neutrons, a Beam Stopper (BS) as shown in Fig. 3.30 was attached to the center of the detector to prevent incident neutrons from entering. The BS stops the incident neutrons to avoid saturation that occurs with the scintillator's luminescence decay time when measuring high-intensity incident neutrons. The BS is made of Cd with a thickness of 1 mm and a length of 3.5 mm × 53.5 mm. The installation position of the BS was determined from the 2D distribution data after alignment of the incident neutrons.

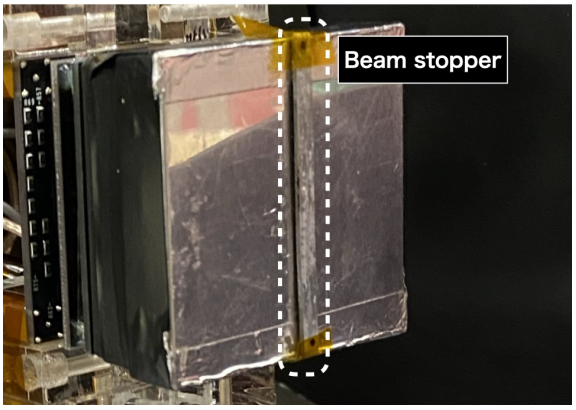

Figure 3.30: Beam Stopper (BS) on FRP detector

3.7 Detection Efficiency of FRP Detector

This chapter explains the detection efficiency of the neutron detector used in the experiment. Section 3.7.1 shows the measurement data of the detection efficiency for each wavelength. Section 3.7.1 shows the difference in detection efficiency for each coordinate of the measured neutrons due to the structure of the FRP detector, and explains how to correct for this difference.

3.7.1 Wavelength Dependence of Neutron Scintillator

The detection efficiency of the FRP detector depends on the absorption cross section of the neutron scintillator (ZnS-LiF). Therefore, the transmittance of ZnS-LiF for each wavelength was measured to obtain the detection efficiency.

The transmittance was measured using the RPMT detector. The RPMT detector uses ZnS-LiF like the FRP detector, and detects neutrons using a neutron absorption reaction. If the absorptance of the ZnS-LiF used in the FRP detector is defined as $\varepsilon_{(\mathrm{frp})}(\lambda)$, and the absorptance of the ZnS-LiF used in the RPMT detector is defined as $\varepsilon_{(\mathrm{rpmt})}(\lambda)$, the detection efficiency $\varepsilon_{(\mathrm{rpmt})}(\lambda)$ of the incident neutrons $I_{\mathrm{in}}(\lambda)$ and the transmitted neutrons $I_{\mathrm{T}}(\lambda)$ of the ZnS-LiF used in the FRP measured by the RPMT contribute in the same way, so the detection efficiency of the FRP detector can be calculated as follows

$$\varepsilon_{(\mathrm{frp})}(\lambda) = \frac{\varepsilon_{(\mathrm{rpmt})}(\lambda) \times I_{\mathrm{in}}(\lambda) - \varepsilon_{(\mathrm{rpmt})}(\lambda) \times I_{\mathrm{T}}(\lambda)}{\varepsilon_{(\mathrm{rpmt})}(\lambda) \times I_{\mathrm{in}}(\lambda)} = 1 - \frac{I_{\mathrm{T}}(\lambda)}{I_{\mathrm{in}}(\lambda)}, \tag{3.4}$$

The measurement was performed in April 2024. The experimental set up is outlined in Fig. 3.31. The RPMT detector is installed in the atmosphere. The most downstream part of the vacuum chamber is covered with an aluminum window. The gap between the aluminum window and the RPMT detector is 5 mm, and the distance from the target to the detector is 1024 mm. The ZnS-LiF used in the FRP detector was fixed to an L-shaped square rod with a hole through which the beam could pass. the TOF of the neutrons that passed through the ZnS-LiF was measured.

Figure 3.32 shows the detection efficiency of this scintillator for each wavelength.The detection efficiency for neutron wavelenghts of 1 nm or longer is nearly 100 %.

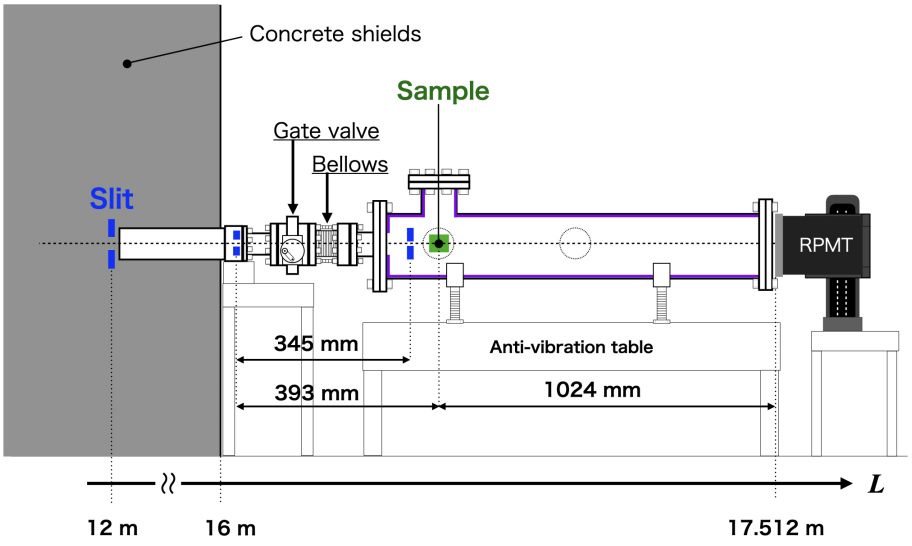

Figure 3.31: SANS setup with RPMT detector

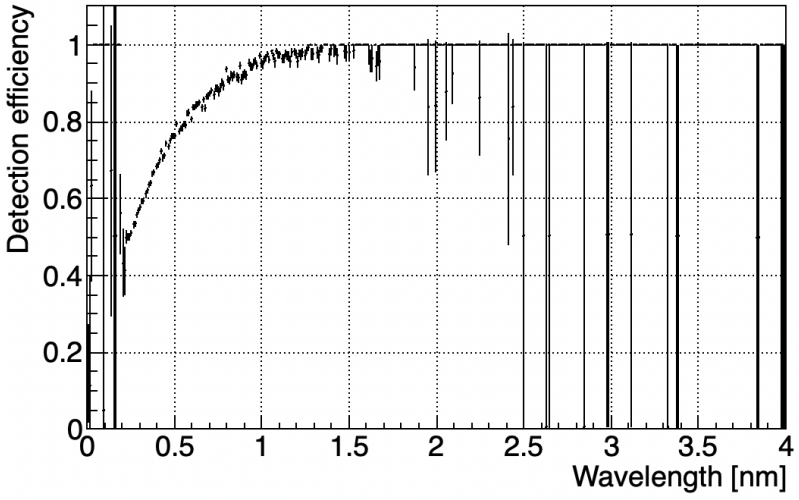

Figure 3.32: Detection efficiency each wavelength from ZnS-^{6}LiF scintillaor

3.7.2 Fluctuations of Detection Position

Figure 3.33 shows the 2D position distribution obtained by measuring isotropic scattering events using the FRP detector. Measurements were performed at J-PARC/MLF/BL05 in December 2023. The target was used 5 mm acrylic plate. The FRP detector was placed away from the incident beam axis and measured. Looking at the position distribution in Fig. 3.33, a periodic pattern was observed that closely resembled the structural arrangement of the $8 \times 8 = 64$ ch MA-PMT (H12700A) in Fig. 3.5. Figure 3.34 is the distribution

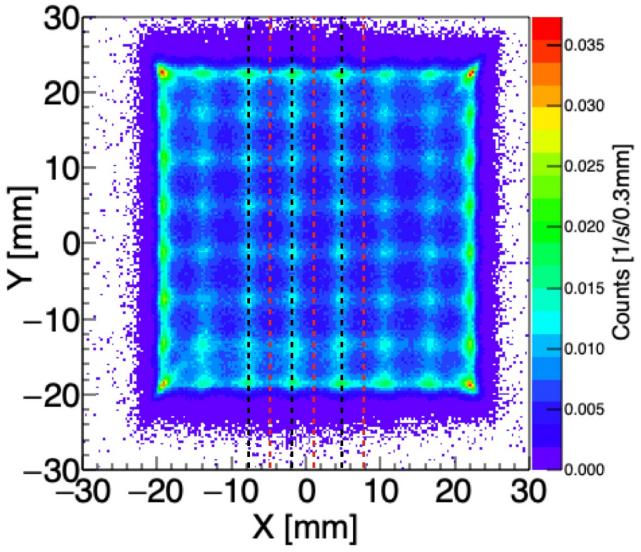

Figure 3.33: Position distribution of isotropic scattering events from an acrylic target measured with an FRP detector.

projected onto the X and Y axes, where each of the eight peak events is thought to correspond to a number of MA-PMT.

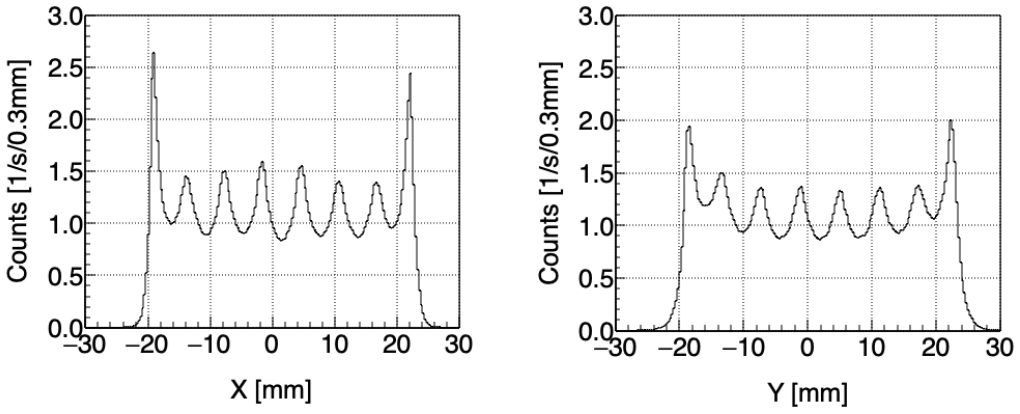

Figure 3.34: Isotropic scattering events.(left) Projected onto the X-axis, (right) Projected onto the Y-axis.

There are two possible reasons why the position distribution of the count rate for istropic scattering events shows periodic peaks and dips.

1) Because the electric field lines existing between the photocathode and the anode are not straight, there is a deviation between the position where the photoelectrons are generated at the photocathode and the center of gravity coordinates of the multiplied secondary electrons.

2) Because of the electrode structure, the correction efficiency of secondary electrons and consequently the electron multiplication factor are position dependent. If the pulse heights of the signals have a position dependence, the counting rates of the logic signals generated by a discriminator circuit operated with a common threshold level will become position dependent.

For **1)**, a performance study using uniformly scattered neutrons with the same type of FRP detector has been conducted [48], and a non-uniformity in the counting rate similar to ours was observed. In the paper, measurements were performed while shifting the irradiation position with a neutron beam collimated to a width of 0.15 mm, the relationship between the coordinates calculated from the data and the coordinates of the irradiation position was obtained, and the half-width of the mutual shift was reported to be 0.50 ± 0.01 mm. On the other hand, for **2)**, we compared the pulse-height distributions of the high and low count-rate parts of the grid to compare the differences in detection efficiency. Figure 3.33 shows the pulse-height distributions of the high count-rate part (black dotted line) and the low count-rate part (red dotted line) of the periodic pattern shown in Fig. 3.35. Here,

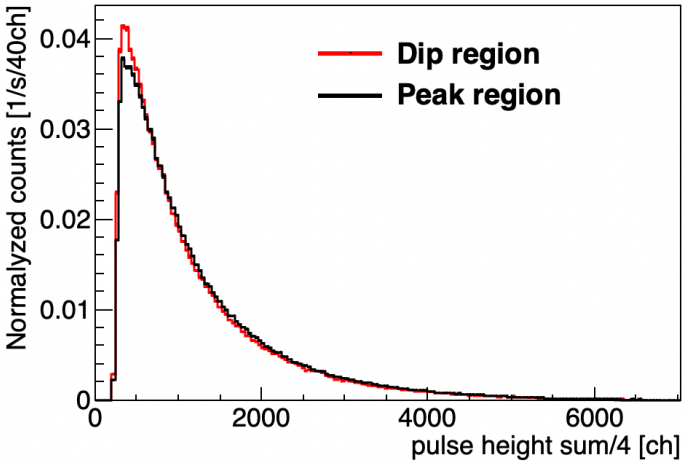

Figure 3.35: Periodic pattern peak and node wave height distribution.

the total counts in each pulse-height distribution are normalized. As can be seen from

this graph, there are more low-height signals in the high-rate region than in the low-rate region.

We assume that the periodic patterns (unevenness in the counting rate) measured by FRP are all generated by the focusing effect of secondary electrons during the electron multiplication process, and use the Monte Carlo method to simulate how the true coordinates focus and diverge according to a certain rule. Figure 3.36 shows a pseudo-periodic pattern.

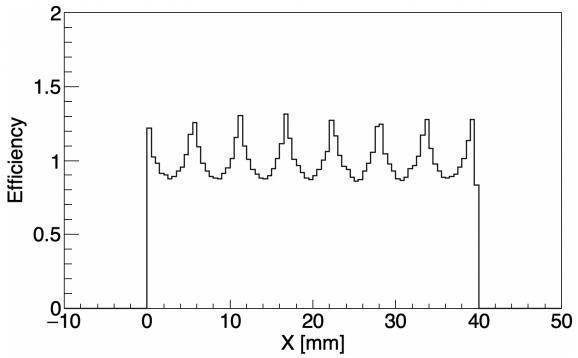

Figure 3.36: Shift in pseudo-uniform scattering

As an example, let us consider the case where the position coordinates of a simulation of a small-angle scattering event are shifted according to the periodic pattern shown in Fig. 3.36. The position distributions before and after the shift are shown in 3.37.

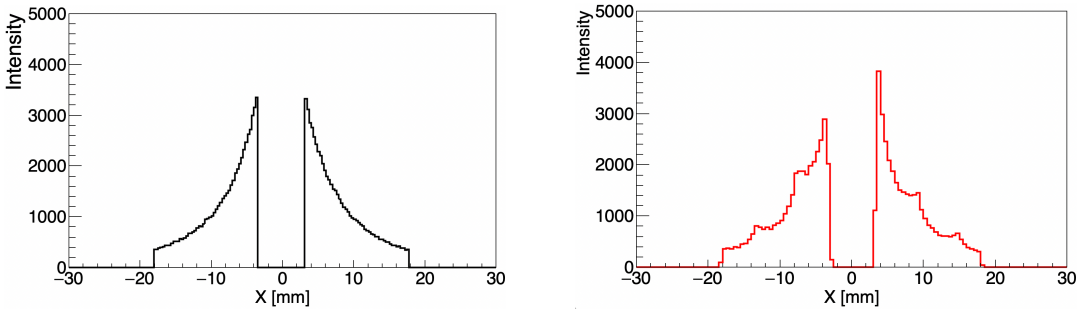

Figure 3.37: Small angle scattering events. (left) Simulated SANS event from nanoparticles, (right) The result of the position coordinate shift caused by Fig. 3.36.

Figure 3.38 is the comparison of the original (before applying the position shifting) position distribution and the one with the correction using the response to uniform event (Fig. 3.36) to the distribution after applying the position shifting. The histogram divided by the response function obtained for uniformly distributied events and the original distribution before modulation are consistent with the reduced chi-square of 1.11. This result shows that the division with the response function obtained from the measurement of

istropic scattering events is a good correction for the distortion effect due to the property of the PMT.

In addition, in the performance verification of the same type of FRP detector conducted at J-PARC/MLF/BL16/SOFIA, there is an example of a correction to the original position distribution by correcting the inverse of the uniform scattering data of polyethylene as the detection efficiency to calibrate the periodic pattern of the position distribution derived from a similar structure [48].

Therefore, all position distribution data measured in this experiment is corrected to have the correct angular distribution by dividing the measured data of isotropic scattering. The correction is also normalized so that the scattering intensity itself does not change.

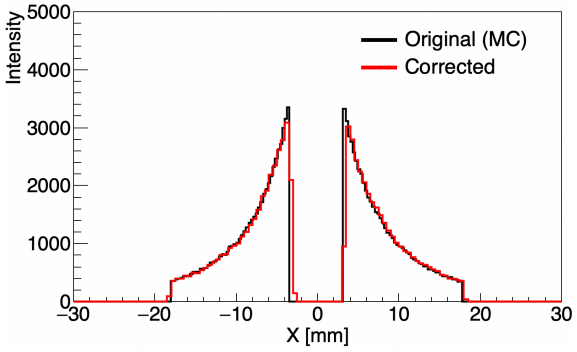

Figure 3.38: Results when correcting for position distribution using the inverse of uniform scattering data as detection efficiency

Chapter 4

Data Analysis

The signal of the unknown short-range interaction is extracted from the deviation of the experimentally measured q distribution spectrum from the spectrum calculated for nuclear scattering alone.

In the following, we first explain the procedure for obtaining the experimental spectrum in Sec. 4.1 and Sec. 4.2. In Sec. 4.3, we explain the density fluctuation and effective density of the V nanopowder in the sample cell, and compare it with neutron transmission data. Next, in Sec. 4.4, we provide details on the calculation of the nuclear scattering spectrum using the Monte Carlo method. In Sec. 4.4.2 and Sec. 4.4.5, we explain the effects of powder agglomeration and the systematic errors of each parameter used in the simulation. Finally, in Sec. 4.4.7, we present the results of comparing the momentum transfer distributions.

4.1 Profile of Incident Neutron

The incident neutrons are measured by removing the BS attached to the FRP detector. Since measuring high-intensity incident neutrons at once may cause counting errors, the most upstream two-dimensional beam slit was changed from $10\,\mathrm{mm} \times 1\,\mathrm{mm}$ to $2\,\mathrm{mm} \times 1\,\mathrm{mm}$ to reduce the intensity of the incident neutrons. The measurement results of the incident neutrons are shown in Table 4.1.

The total count rate is normalized by the number of proton pulses between the timing of the detector signal and the kicker pulse corresponding to real time zero. Five points were measured by shifting the center position by 2 mm. The summed spectrum of those five data was found to well reproduce the neutron intensity in the 2D beam slit area of the vanadium sample. The intensity of the incident neutrons was $14.185 \pm 0.004\,\mathrm{kcps}$.

Table 4.1: Summary of incident neutron measurement

Data	2D slit center	cps	kicker pulse	Timing pulse
IN1	(X,Y) = (52.000,21.500)	1615.32±1.34	22373	25000
IN2	(X,Y) = (50.000,21.500)	2271.80±1.53	24212	25000
IN3	(X,Y) = (48.000,21.500)	3192.49±1.82	24213	24997
IN4	(X,Y) = (46.000,21.500)	3556.64±1.92	24194	24999
IN5	(X,Y) = (44.000,21.500)	3550.56±2.01	22052	25000
INsum	-	14186.8±3.9	-	-

The difference between the numbers of the kicker pulse and the timing pulse in Table 4.1 is due to the difference in the number of pulses caused by the proton beam being sent to the MR during the measurement, or due to the time the beam operation was stopped due to an operational problem of the accelerator.

4.1.1 Flight time of Incident Neutron

The flight time of neutron was measured as the time difference between the neutron detector signal of each event and the most recent kicker pulse delivered by the J-PARC booster synchrotron. Figures 4.1 shows the respective time-of-flight distributions measured at a pulse period of 25 Hz for the incident neutron data shown in Table 4.1.

As explained in Sec. 3.1, the TOF in Fig. 4.1 is defined as the difference in the time of flight between the detector signal and the most recent kicker pulse, so neutrons that arrive at the detector later than 40 ms will be included in the next pulse time $0 \sim 40$ ms.

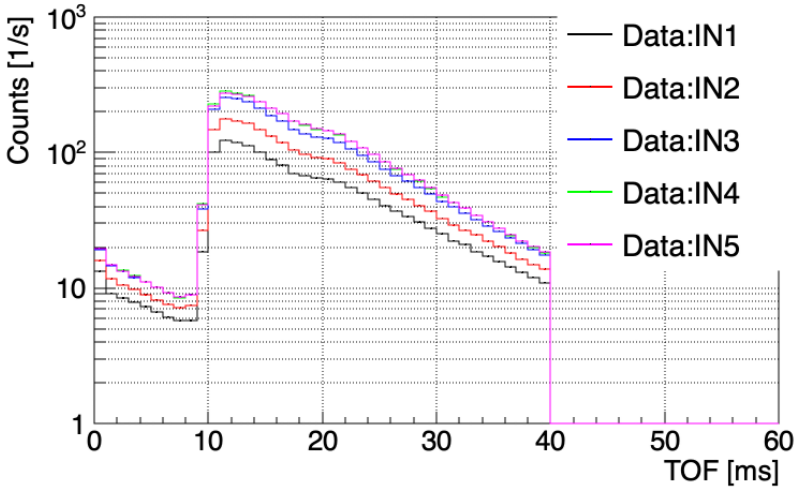

Figure 4.1: Flight time of incident neutron by 25 Hz frequency.

This effect is called the "flame overlap (FOL)" effect.

Next, the TOF data in Fig. 4.2, which corresponds to the energy of the actual incoming

neutrons, is obtained by analyzing the data on the timing when the proton pulse from the booster synchrotron was sent to the MR (Main Ring) instead of the mercury target. During this time, the proton beam does not reach the MLF and no kicker pulse signal is generated. Therefore, the time information is not reset and the TOF of the neutrons

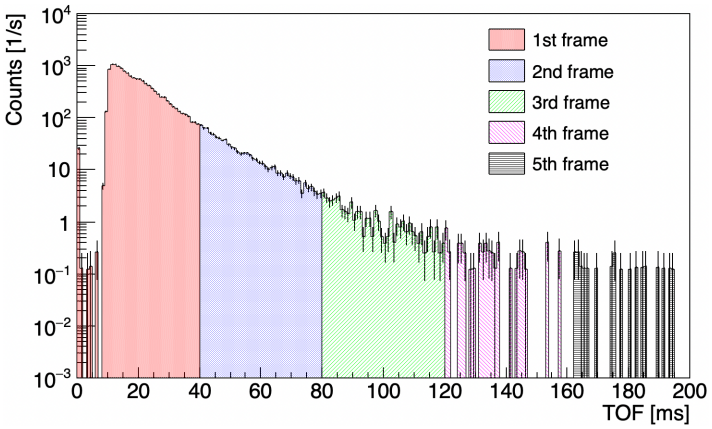

Figure 4.2: TOF spectrum of incident neutrons from actual neutron velocity

can be measured. In the operating status of the accelerator as of June 2023 when the experiment was conducted, the timing pulse diagram in Fig. 4.3 shows that the proton pulse is sent to the MR once every 130 pulses, and the intensity of the incident neutrons is attenuated.

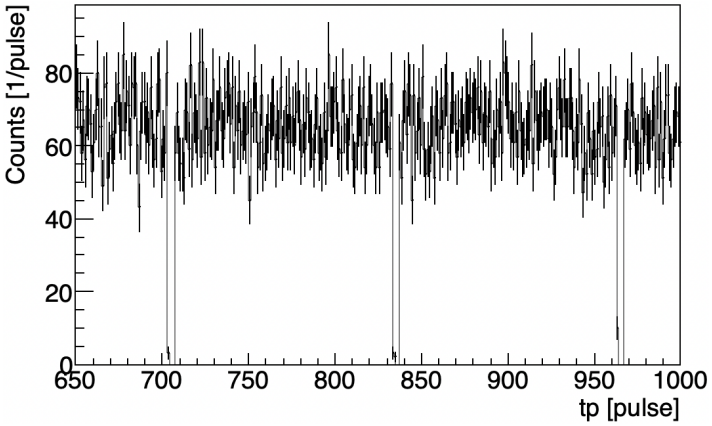

Figure 4.3: Timing pulse signal of incident neutrons (for example, a signal between $650 \sim 1000$ pulse).

Figure 4.4 shows the timing pulse signal as a remainder of 130 pulses, and can measure the TOF from 4 pulses from the 2nd frame to the 5th frame, that is, from 40 ms to 200 ms. In addition, the first pulse (1st frame) when the proton pulse is injected into the MLF is an event that includes only 0 ms to 40 ms as the actual TOF. During this time, the flight time between 0 ms and 200 ms is properly measured, and the next kicker pulse does not

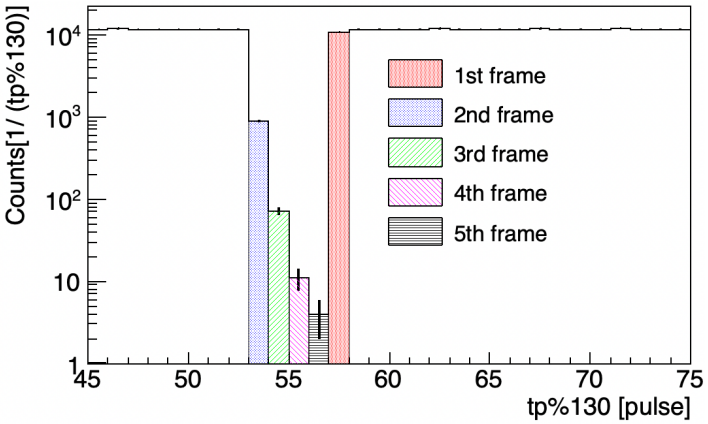

Figure 4.4: Timing pulses expressed as residual of 130 pulses. (2nd to 5th frame: timing when the proton pulse is injected into the MR, 1st frame: timing when the proton pulse is injected again into the MLF)

arrive until the next proton pulse is delivered to the mercury target, so the actual flight time distribution can be obtained. Figure 4.2 shows that the actual neutrons are those with TOF between 10 ms and 200 ms. Here, the events seen at TOF = 1 ms are gamma flashes that occur when neutrons are generated and peaks caused by neutrons that are not decelerated and enter the system.

Next, we explain the relationship between Fig. 4.1 and Fig. 4.2. The FOL data measured at 25 Hz frequency can be compared by calculating the actual TOF data as residual 40 ms. Figure 4.5 shows the FOL data and the actual TOF spectrum as residual 40 ms. The events measured between 1 ms and 9 ms in the FOL data were allocated to the time region between 41 ms and 49 ms in the actual TOF spectrum. In the MC calculation for the FOL data, this correction was performed according to the ratio of the FOL and non-FOL data.

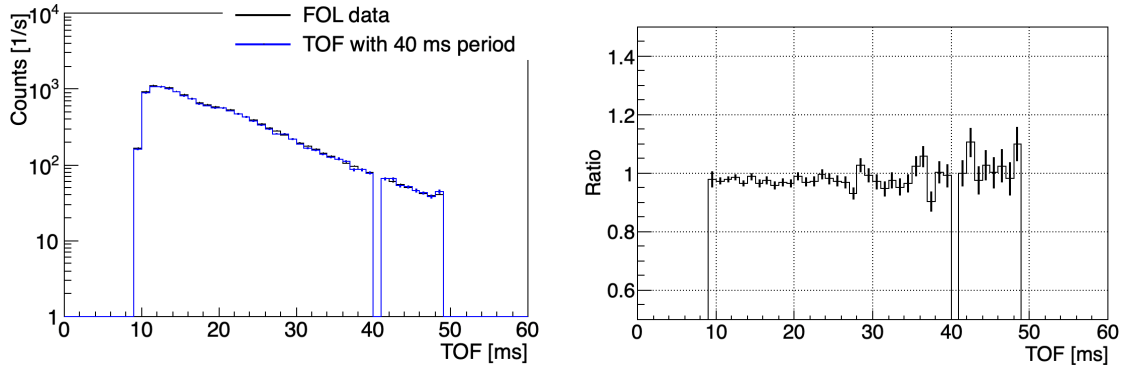

Figure 4.5: Comparison of FOL and TOF data.(left) TOF calculated with the remainder of 25 Hz period, (right) ratio to FOL data.

4.1.2 Definition of the Coordinates

Next, Fig. 4.6 shows the spatial distribution of the intensity of the incident neutron beam.

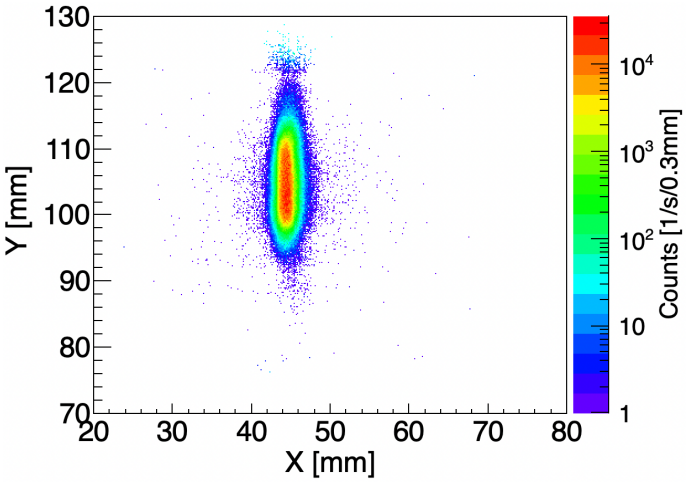

Figure 4.6: Spatial distribution of the intensity of the incident neutron beam.

The incident neutron intensity shows a wide distribution in the Y direction because a line collimator is used. The origin of the scattering angle is corrected by setting the center position of the incident neutron intensity distribution as the origin of the X and Y axes. The correction was determined from the mean value determined by fitting the distribution projected onto the X and Y axes shown in Fig. 4.7 with a Gaussian function. The respective means for the X and Y axes obtained from the fit were 44.4595 ± 0.0005 mm and 105.064 ± 0.002 mm.

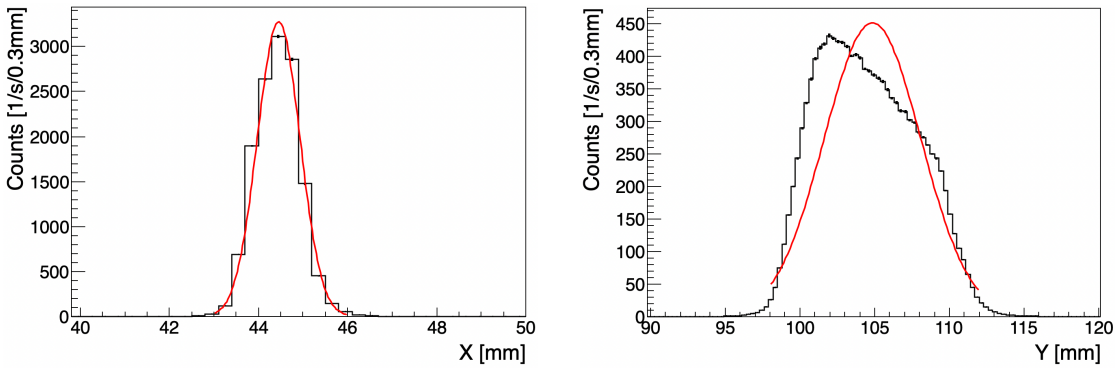

Figure 4.7: Gaussian fit of peak position of incident beam. (left) Projected onto X-axis, (right) Projected onto Y-axis.

4.2 Analysis of the Scattered Neutron

The q-distribution spectrum is basically obtained by counting the number of events for each value of the momentum transfer q. Since q is given by Eq. (4.1),

$$q = 2k \sin\left(\frac{\theta}{2}\right), \tag{4.1}$$

where k and θ are the wave number and the scattering angle of a neutron, and thus it can be related to the data of the detected position x and the flight time t of neutrons as

$$\theta = \arctan\left(\frac{x}{L}\right) \tag{4.2}$$

$$k = \frac{2\pi}{\lambda} = 2\pi\left(\frac{395.6}{v}\right)^{-1} = 2\pi\left(395.6\frac{t}{L}\right)^{-1} \tag{4.3}$$

where λ, v and L represent the wavelength, velocity and flight path length of neutron, respectively. The de Broglie wavelength λ of a neutron is given in unit of nm using the conversion coefficient $395.6 = h/(m_n c^{-2})$. Here, h is the Planck constant and m_n is the rest mass of a neutron. The angular distribution is defined only in the X direction because we constructed a setup in which the incident beam is collimated only in the horizontal direction as shown in Fig. 3.10.

In this section, the method for processing the position and time information of the scattered neutrons for each sample measured with the FRP detector is described. When measuring scattered neutrons, a BS is attached to the FRP detector to avoid dead time due to very high intensity of direct incident neutrons. This is to prevent the effects of detector counting losses and to distinguish between incident neutrons and scattered events. Table 4.2 shows a summary of the scattering measurements for each sample. In the scattering measurements, the upstream 2D slit was changed to $10 \times 1\,\mathrm{mm}^2$.

Table 4.2: Summary of scattered neutron measurement

Data	2D slit center	cps	kicker pulse	Timing pulse
Sample cell	(X,Y) = (48.000,21.500)	17.110±0.012	3136177.0	3553532.0
Empty cell	(X,Y) = (48.000,21.500)	1.064±0.008	440816.0	523250.0

4.2.1 Position Distribution

First, we show the spatial distribution in the x (horizontal) and y (vertical) directions of the sample with V nanoparticles and the empty cell of scattered neutron by SANS measurement in Figure 4.8.

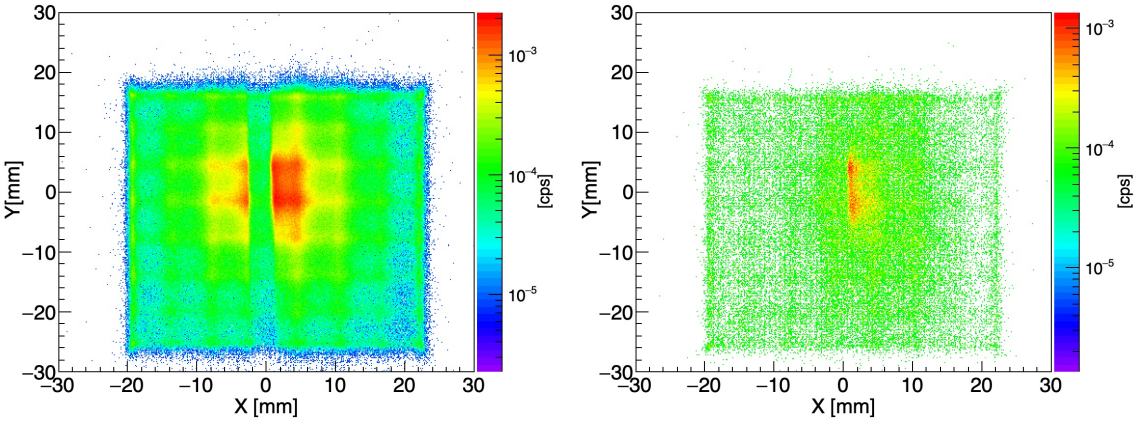

Figure 4.8: Two-dimensional distribution of scattered neutrons. (left) sample cell and (right) empty cell. The attenuation of the intensity distribution at the center of each distribution is due to the presence of a beam stopper to suppress the incoming neutrons.

The origin of the position distribution was determined from the peak position of the incident neutrons shown in Fig. 4.7. Fig. 4.9 shows the distribution projected onto the x- and y-directions.

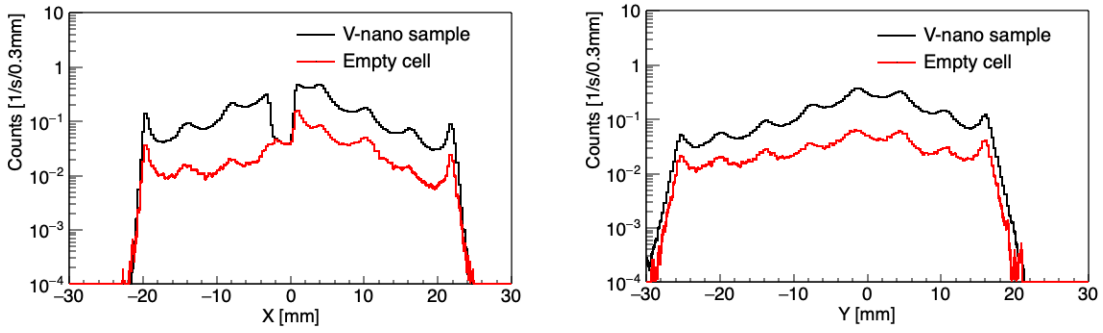

Figure 4.9: Position distribution of scattered neutrons from the sample cell and empty cell. (left) projected on the X-axis, (right) projected on the Y-axis.

As explained in Sec. 3.7.2, the multiplied electrons tend to concentrate at the center of each pad of the multi-anode photomultiplier tube in the FRP detector, leading to non-uniformity of sensitivity as a function of position. To correct for this effect, the position

distribution for real sample was divided with the one for isotropic scattering. The corrected distribution of scattered neutrons in the x and y directions is shown in Figs. 4.10 and 4.11. The analysis ranges were set in the range of ±18 mm for the X coordinate and ±15 mm for the Y coordinate to utilize the sensitive area of the FRP detector. In addition, since BS was installed at the position not exactly at the center of the incident neutrons, the range of ±3.3 mm in the X coordinate has been deleted to maintain symmetry.

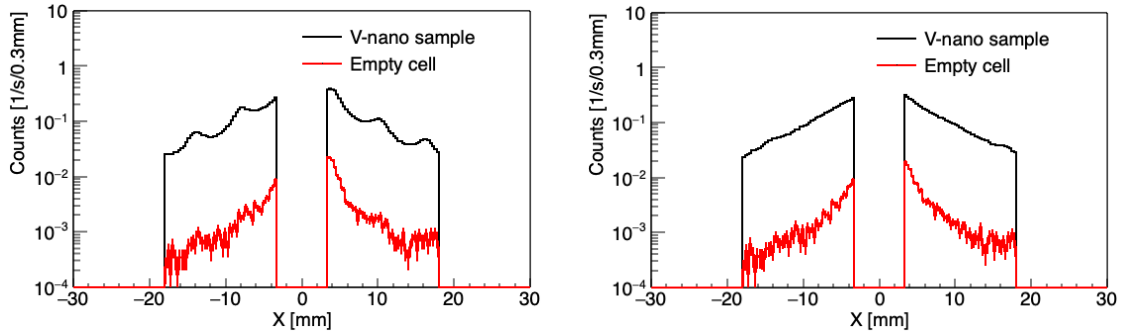

Figure 4.10: Position correction of X-distribution.
(left) before correction, (right) after correction.

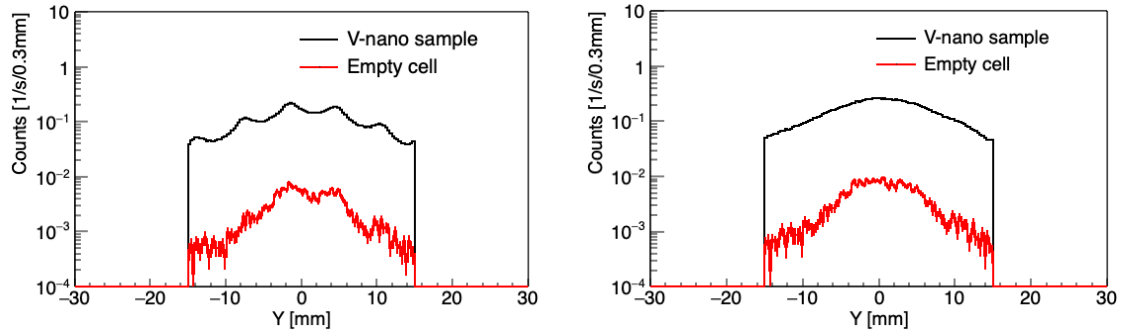

Figure 4.11: Position correction of Y-distribution.
(left) before correction, (right) after correction.

4.2.2 Neutron Wavelength

The TOF spectrum of scattered neutron is shown in Fig. 4.12. The wavelength of neutron is defined by the distance from the MLF moderator to the detector, which is 17.512 m, based on the TOF information measured by the FRP detector. This data is obtained from the data while the proton beam is being transported to the MR, as explained in Sec. 4.1.1. The analysis range for each sample is the same as in Figs. 4.10 and 4.11.

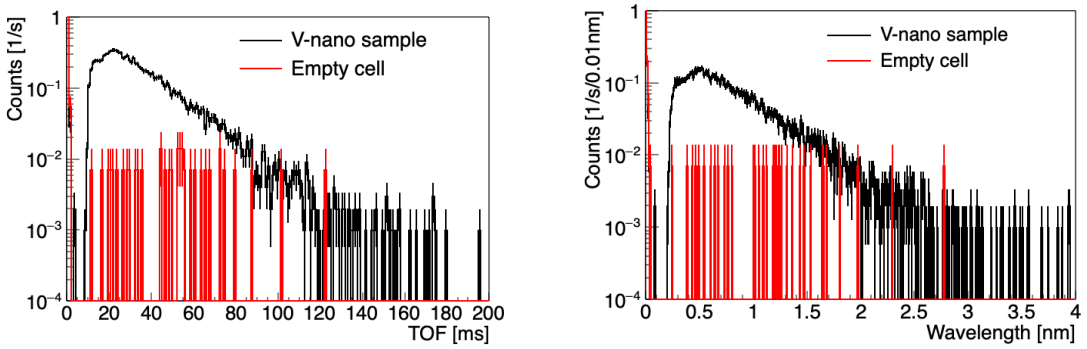

Figure 4.12: TOF and wavelength data of scattered neutron.(left) TOF spectrum, (right) Wavelength spectrum calculated by the TOF.

The peak at TOF < 2 ms for each sample is an event of gamma flash generated from the neutron source or neutrons that entered without being decelerated, so it has the same intensity regardless of the sample. This event is excluded when analyzing momentum transfer because it becomes BG. Next, the TOF distribution of scattered neutrons measured at a pulse frequency of MLF of 25 Hz is shown in Fig. 4.13. The FOL data was compared with the actual TOF data from Fig. 4.12 and treated appropriately. Namely, the events with T0F < 9 ms were considered as the ones with T0F > 40 ms. Events with T0F < 2 ms are also rejected due to events such as gamma flashes.

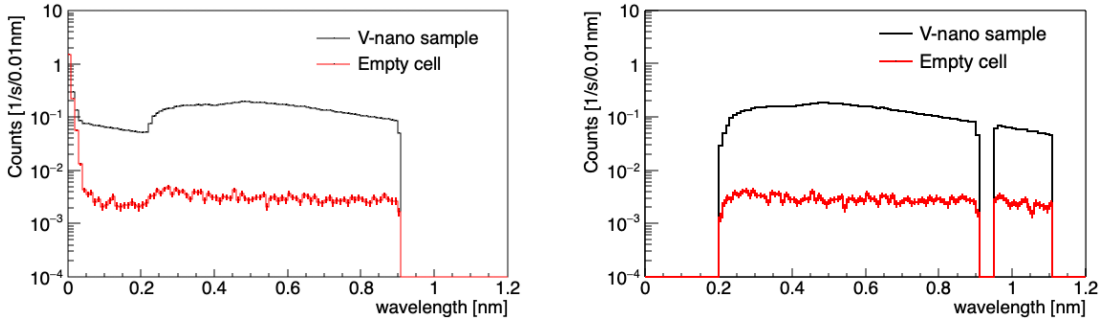

Figure 4.13: Neutron wavelength of scattered neutrons from the FOL data.(left) The repetition rate of the MLF proton beam was 25 Hz and (right) the one after shifting wavelength from $0 \sim 0.2$ nm to $0.9 \sim 1.1$ nm

4.3 Transmittance of Sample Cell

The scattering intensity of neutrons is attenuated by the absorption effect when passing through the window material of the sample cell and the nanoparticle target. To investigate these effects, transmittance measurements were performed. The transmittance was calculated as the ratio of the intensity of the incident beam to the intensity of the transmitted beam. The measurements were performed by removing the BS attached to the FRP detector, changing the upstream 2D beam slit width to (1 mm × 2 mm), and scanning the actual incident beam width (1 mm × 10 mm). The measurement summary for each sample is shown in Table 4.3.

Table 4.3: Summary of neutron transmission measurements for each sample

Data	2D slit center	cps	kicker pulse	Timing pulse
C1	(X,Y) = (52.000,21.500)	1497.94±1.24	24221	25001
C2	(X,Y) = (50.000,21.500)	2120.98±1.48	24214	25000
C3	(X,Y) = (48.000,21.500)	2294.87±1.76	24208	25000
C4	(X,Y) = (46.000,21.500)	3341.69±1.86	24216	25000
C5	(X,Y) = (44.000,21.500)	3324.25±1.85	24203	25000
Esum	-	13279.7±3.7	-	-
S1	(X,Y) = (52.000,21.500)	1469.86±1.23	24218	25000
S2	(X,Y) = (50.000,21.500)	2075.74±1.46	24210	24998
S3	(X,Y) = (48.000,21.500)	2921.00±1.74	24215	25001
S4	(X,Y) = (46.000,21.500)	3251.72±1.83	24210	24999
S5	(X,Y) = (44.000,21.500)	3248.55±1.83	24207	24998
Vsum	-	12966.9±3.7	-	-

The scan data of the transmitted neutrons for each sample were integrated, and the position distribution profile and transmission rate are shown in Figs. 4.14 and 4.15.

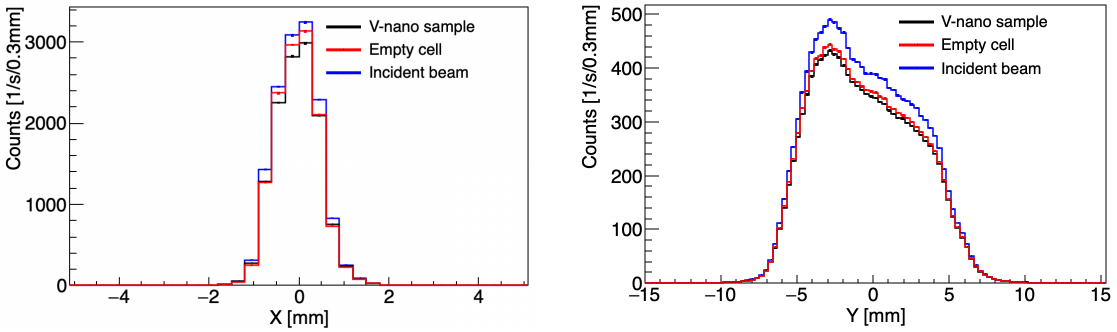

Figure 4.14: Neutron intensity of each sample measured by removing the BS.(left) projected on the X-axis,(right) projected on the Y-axis.

Figure 4.15 shows the transmittance of each cell as a function of the neutron wavelength. Since the number of scattered neutron events is less than 0.1 % compared to the number of transmitted neutrons, all neutrons detected by the FRP detector can be used.

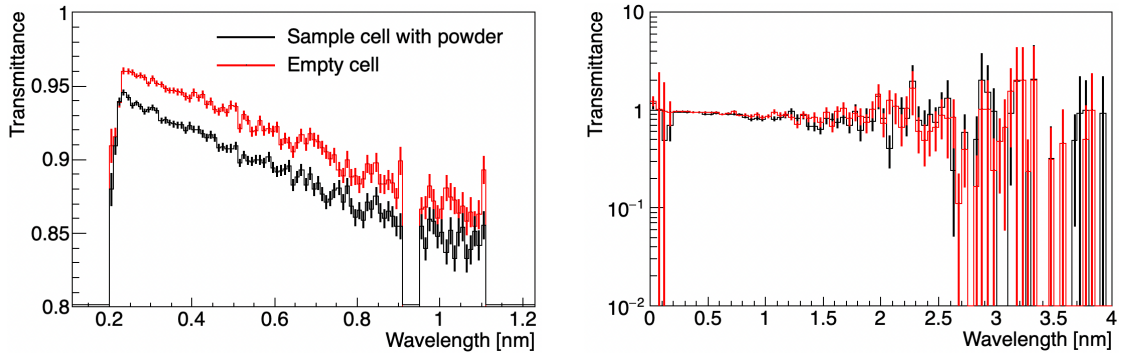

Figure 4.15: Neutron transmittance of each cell.
(left) FOL data with 25 Hz period (right) Actual TOF data.

4.3.1 Density Fluctuations of Sample powder

The V nanopowder were packed in the sample cell with pressure by the window foil Fig. 3.27, which may cause density fluctuations. The density fluctuation of the V nanopowder in the sample cell was observed from the transmitted neutron images measured at each pixel of the FRP detector as shown in Fig. 4.16.

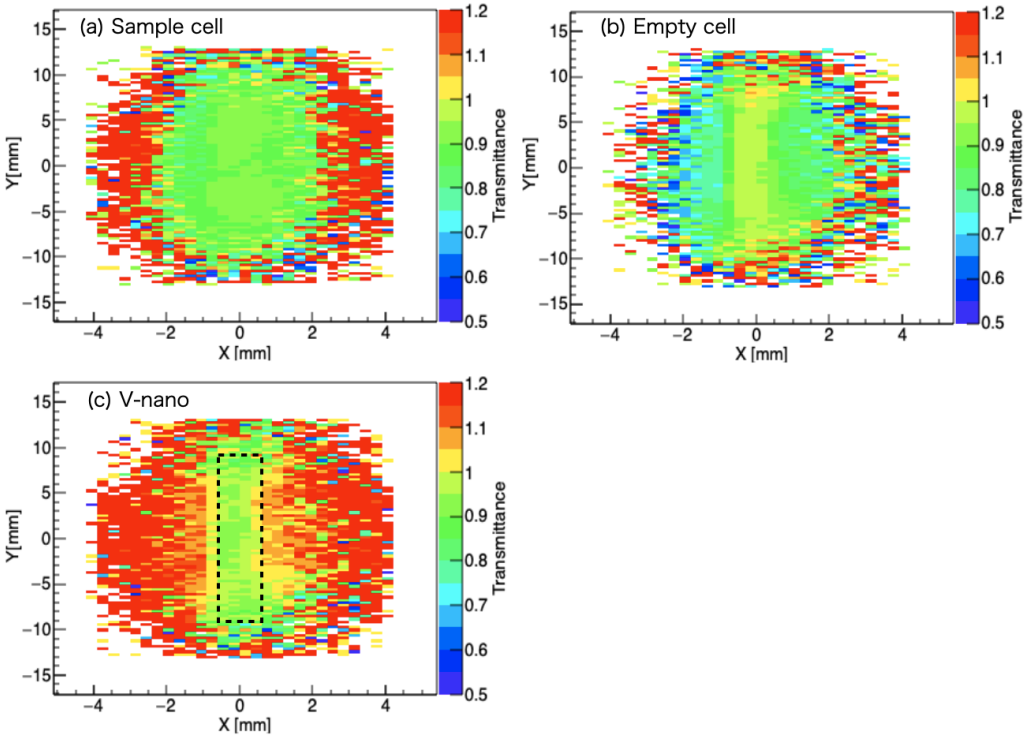

Figure 4.16: Neutron transmission imaging (NTI) of each cell. (a) sample cell, (b) empty cell, (c) vanadium nanoparticles inside the sample cell.

The transmittance from the V nanopowder shown in (Fig. 4.16:(C)) was calculated by correcting the transmittance of the windows of the sample cell, which was determined from the transmittance of the empty cell. The area displayed in neutron transmission imaging (NTI) does not distinguish between scattered neutrons and transmitted neutrons. Therefore, Fig. 4.17 shows the pixel frequency distribution of the area surrounded by the black dotted line ($-9.0\,\mathrm{mm} < \mathrm{Y} < 9.0\,\mathrm{mm}, -0.6\,\mathrm{mm} < \mathrm{X} < 0.6\,\mathrm{mm}$) in the NTI of a V nanopowder (Fig. 4.16:(c)).

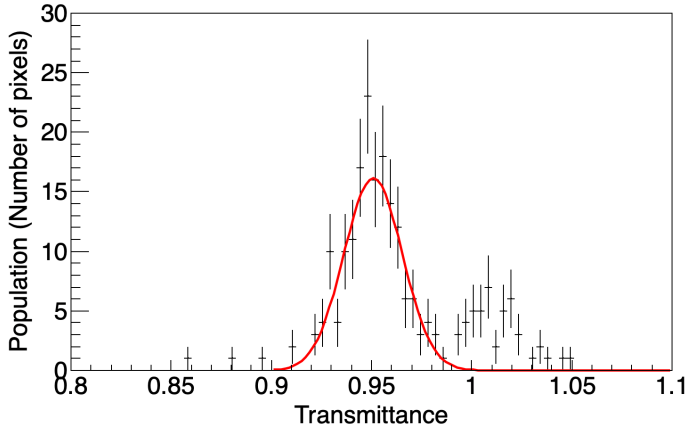

Figure 4.17: Pixel frequency distribution in NTI of V nanopowder.

In the frequency distribution in Fig. 4.17, peaks were observed near the transmittance of 0.95 and 1.0. As a result of fitting the transmittance with a Gaussian in the transmittance range of $0.85 \sim 0.99$, the average transmittance of the V nanopowder obtained was 95 %, with a standard deviation of 1.5 %. Since the transmittance generally depends on the atomic density, the uniformity error was estimated to be 1.5 %. However, the peak in the transmittance of Fig. 4.17 near 1.0 suggests that the powder may not be packed uniformly and may have thin areas. Therefore, the results of limiting the analysis range of the NTI (Fig. 4.16:(C)) of V nanopowder to the edge part are shown in Fig. 4.18.

The analysis range for Fig. 4.18 was set to ($-9.0\,\mathrm{mm} < \mathrm{Y} < 9.0\,\mathrm{mm}, 0.3\,\mathrm{mm} < \mathrm{X} < 0.6\,\mathrm{mm}$) in Fig. 4.16:(C). A Gaussian fit with a transmittance range of $0.85 \sim 1.1$ resulted in an average V nanopowder transmittance of 99 % with a standard deviation of 2.9 % and average statistical error for all 54 pixels used in the analysis within this range is 1.3 % (see Fig. 4.18:(right)). This means that there is a significant density fluctuation of the powder. The range specified in the NTI analysis based on the transmittance obtained from the SANS measurements is not related to the distance from the center of the actual sample cell. Therefore, this analysis does not accurately determine which part of the powder in the sample cell is thin. This is because the incident beam itself diverges due to the distance from the sample to the detector being about 1000 mm. Next, in order to complement

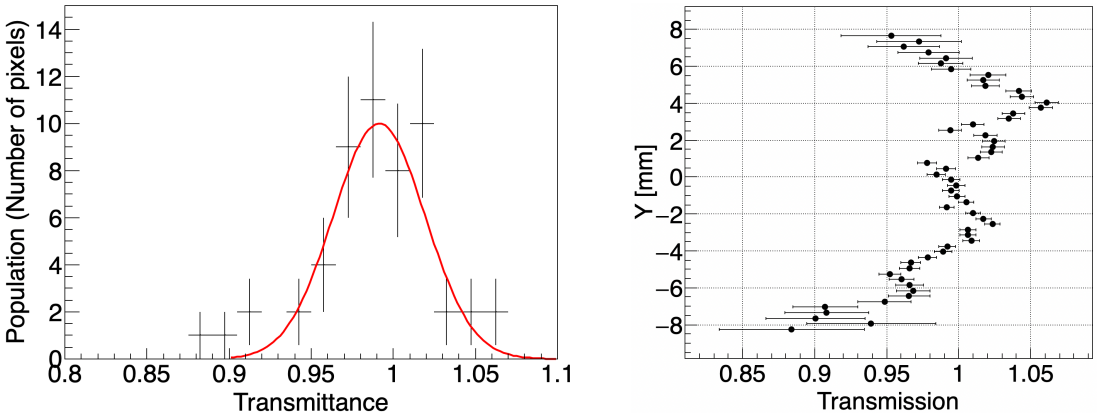

Figure 4.18: NTI of V nanopowder away from the cell center. (left) pixel frequency, (rigth) statistical error of each pixel used in analysis

the neutron data, we will explain the results of the analysis of the density variation of vanadium powder based on the transmittance using gamma rays in the next section.

4.3.2 Gamma-ray Transmittance of Sample Cell

To check the effective thickness of the target material, γ-ray transmittance measurements were performed. The method is as follows: a collimated gamma-ray beam of 59.5 keV was generated from a ^{241}Am check source using a collimator made of a 10 mm thick lead plate with a 2 mm diameter hole. As shown diagrammatically in Fig. 4.19, the target cell was placed 1.5 cm downstream of the gamma-ray beam, and the transmitted gamma rays were measured using a 10 cm × 10 cm × 5 mm NaI(Tl) detector located 15 cm away from the target cell.

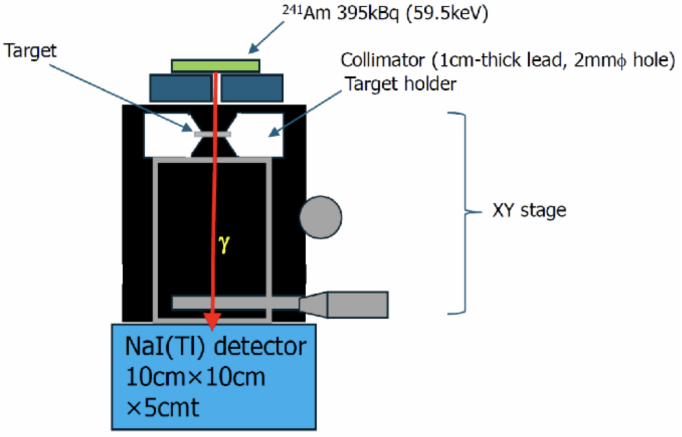

Figure 4.19: Schematic of gamma ray transmission measurement device

The pulse height spectrum of gamma rays from ^{241}Am obtained from this setup is shown in Fig. 4.20.

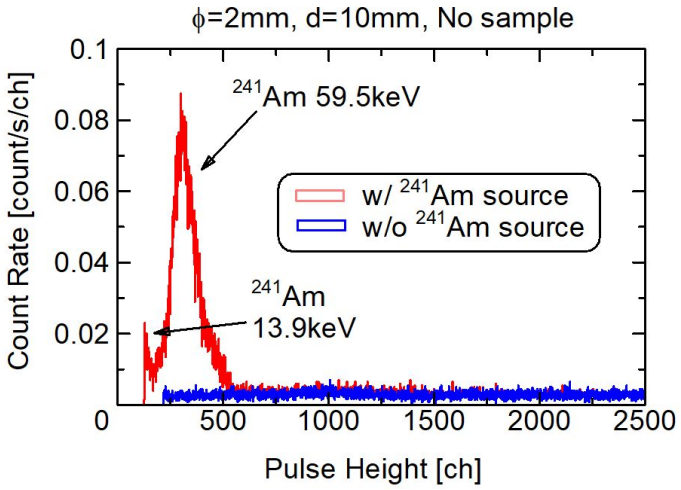

Figure 4.20: Pulse height spectrum of gamma rays from ^{241}Am

First, gamma rays were irradiated onto the surface of the empty cell, and the transmission was determined to be 76.61 ± 0.53 % from the incident gamma ray intensity and the transmitted gamma ray intensity. The window material used for the empty cell is a vanadium alloy containing nickel with a thickness of 4.85 wt%, and the attenuation coefficient available in the NIST database XCOM is 0.8009 cm^2/g (E = 60 KeV). The thickness of the window material is 250 μmt processed foil used on the front and back of the spacer. The effective thickness was calculated from this value based on the measured transmittance, which was $537 \pm 14\,\mu$m.

The surface of the cell containing V nanopowder was then scanned in the x and y directions. Figure 4.21 shows the transmittance as a function of x and y position, respectively. The transmittance is calculated as the transmittance from the V nanopowder, taking into account the attenuation through the empty cell. The left panel of Fig. 4.21 shows the result of the scanning in the Y-direction, which shows the transmittance becomes low at the region of $\mathrm{Y} < -2$ mm or $\mathrm{Y} > +2$ mm. This is because in those regions the collimated γ-ray beam overlaps with the aluminum block part of the cell. Similarly, the result for the X-direction (Fig. 4.21 right) showed that the transmission was extremely low in the region of X <-1mm due to the same reason in the case of the Y-direction.

First, the mass attenuation coefficient, which can be considered from the composition ratio, was calculated to be 0.729 cm^2/g ($E = 60$ KeV) using XCOM. Since 15.6 mg of the V nanoparticles was packed into a volume of 10 mm $\times$ 0.3 mmt, the nominal density is calculated to be 0.6642 $\mathrm{g/cm}^3$. At this time, the transmittance of gamma rays is 98.6 %

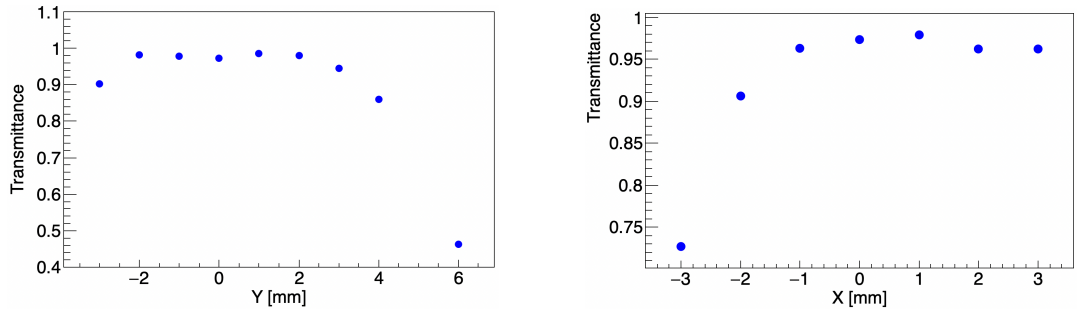

Figure 4.21: Transmittance of sample cell with gamma rays. The horizontal axis is set to 0 at the initial position where the cell was placed.

when the powder is uniformly dispersed. The effective thickness compared to the nominal value is confirmed as shown in Fig. 4.22.

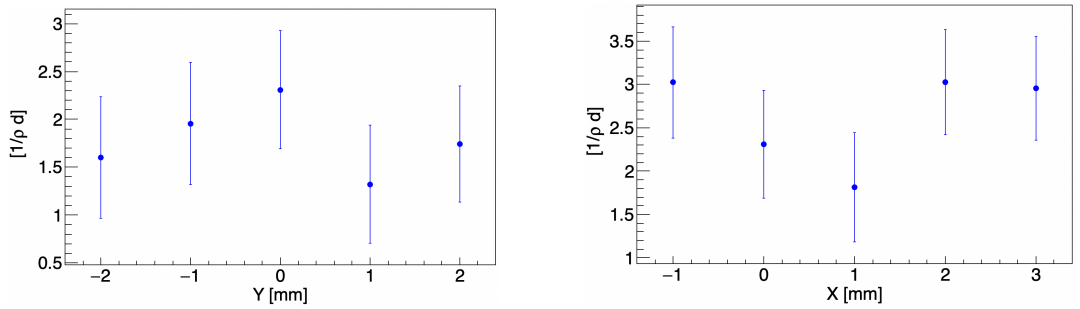

Figure 4.22: The density multiplier compared to the transmittance when vanadium nanopowder is uniformly dispersed.

The average transmittance of V nanoparticles measured by gamma ray transmission scan was 96.9 ± 0.8 %, which is worse than the transmittance when V nanopowder is uniformly dispersed in the cell. This is calculated as 2.17 ± 0.57 times the density when the powder is uniformly dispersed in the cell. The transmittance measured by SANS near the center of the sample cell is calculated to be 96.7 ± 0.9 %, and the density compression rate is calculated to be 2.31 ± 0.62 times higher. This increase in density can be understood by assuming the presence of some voids around the edges of the volume containing the powder, as discussed in Sec. 4.3.1.

The effective density is determined by comparing the measured data with Monte Carlo simulations of nuclear force scattering calculated using the average powder density in the sample cell, as described in Sec. 4.4.3.

4.3.3 Fit Analysis of Effective Density of Neutron Transmission

In this section, the effective density of sample powder in the cell is determined from the wavelength dependence of neutron transmittance. From the results of gamma-ray measurements in Sec. 4.3.2, it is predicted that the density of the powder in the cell is about 2 to 3 times higher than the nominal density in the center on average. Therefore, the ratio from the average density was used as the fit parameter for the analysis. The fitting function is shown in Eq. (4.4).

$$f(\lambda) = \exp\Big(-\rho d(\sigma_{\mathrm{abs}}(\lambda) + \sigma_{\mathrm{coh}}(\lambda) + \sigma_{\mathrm{inc+diff}})P_0\Big) \tag{4.4}$$

$$\sigma_{\mathrm{abs}}(\lambda) = \sigma_{abs}\left(\frac{2200}{395.6}\lambda\right) \tag{4.5}$$

$$\sigma_{\mathrm{coh}}(\lambda) = 11.09\lambda^{2.001}\exp(-6.225\times10^{-3}\lambda) \tag{4.6}$$

$$\sigma_{\mathrm{inc+diff}} = \sigma_{\mathrm{inc}} + \sigma_{\mathrm{diff}} = 4.08 + 0.83 \tag{4.7}$$

Here, ρ is the average powder density estimated from the volume of the sample cell, d, the thickness of the powder volume, is 300 μm and P_0 is a fitting parameter. $\sigma_{\mathrm{abs}}(\lambda)$, $\sigma_{\mathrm{coh}}(\lambda)$ and σ_{inc} are the absorption cross section, the coherent scattering cross section and the incoherent scattering cross section, respectively. $\sigma_{\mathrm{abs}}(\lambda)$ is 4.64 b, calculated from the results of composition analysis in Table 2.10. $\sigma_{\mathrm{coh}}(\lambda)$ is taken into account using the SAXS particle size distribution obtained in Fig. 2.21. Equation (4.5) is expressed as a function that depends on the wavelength from the 1/v law for thermal neutrons (2200 m/s). The wavelength dependence of $\sigma_{\mathrm{coh}}(\lambda)$ is shown in Fig. 4.23. This term, which depends on momentum transfer, is the result of calculating the cross section when integrated over the entire solid angle.

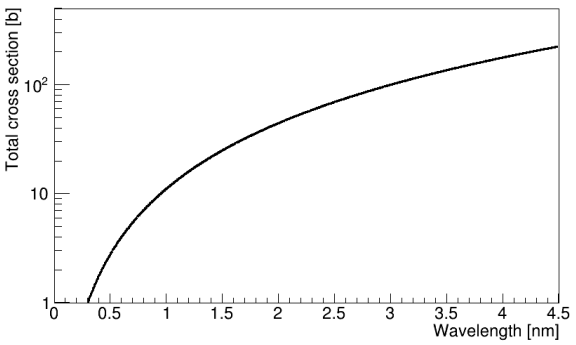

Figure 4.23: Wavelength dependence of $\sigma_{\mathrm{coh}}(\lambda)$.

Fig. 4.23 is the plot of Eq. (4.6). Equation (4.7) is the angle-independent cross section consisting of the diffuse scattering cross section 0.83 b and incoherent scattering cross section $\sigma_{\mathrm{inc}} = 4.08$ b shown in Table 2.10.

The fitting results for Eq. (4.4) are shown in Fig. 4.24. For the transmitted neutron data, the frame overlap data from Fig. 4.15, which is statistically superior, was used. The transmittance of the V nanopowder filled in the sample cell was calculated by dividing the attenuation of the neutrons transmitted from the empty cell by the transmittance of the sample cell.

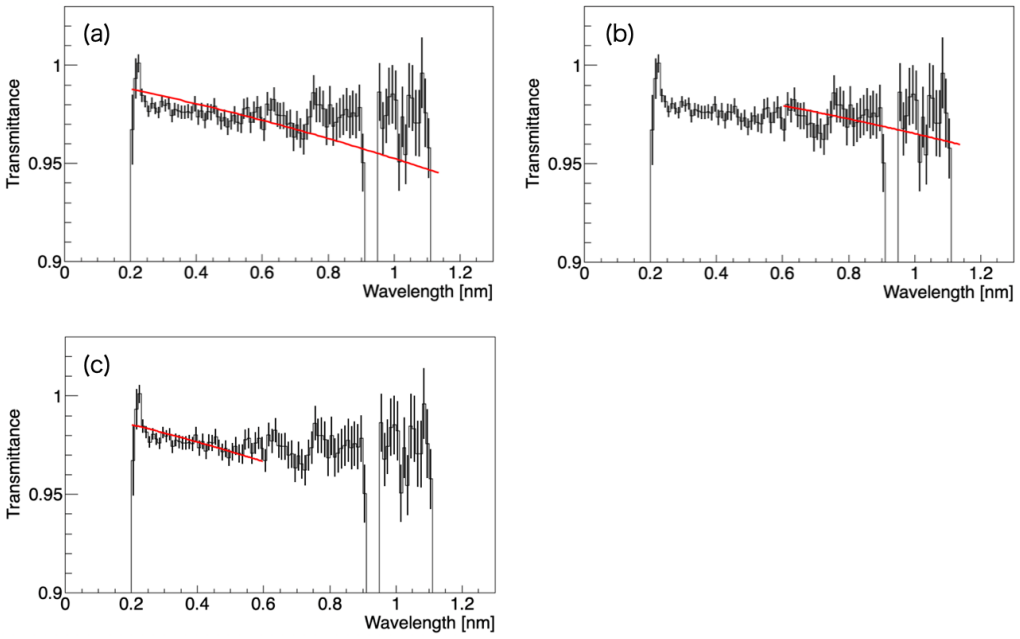

Figure 4.24: Fitting results for the neutron transmission data of V nanopowder in the cell. (a) Fit range: $\lambda : 0.2 \sim 1.14$ nm, (b) Fit range: $\lambda : 0.6 \sim 1.14$ nm, (c) Fit range: $\lambda : 0.2 \sim 0.6$ nm.

Figure 4.24 did not match the wavelength dependence predicted by the cross section at wavelengths less than $\lambda = 0.6$ nm. The fitting results for the effective density differ between $0.2 \sim 0.6$ nm and $0.6 \sim 1.14$ nm. The chi-squared value is best in the range of $0.6 \sim 1.14$ nm, and the estimated effective density is 2.931 ± 0.154 times in Table 4.4.

Table 4.4: Magnification from the average density obtained as a result of fitting.P_0 is the ratio from the average density.

	P_0	fit range [nm]	χ^2/ndf
Fit (a)	4.045 ± 0.100	$0.2 \sim 1.14$	179/86
Fit (b)	2.931 ± 0.154	$0.6 \sim 1.14$	40.39/46
Fit (c)	4.835 ± 0.132	$0.2 \sim 0.6$	50.87/39

To investigate the cause, there was no significant difference between the measured transmittance of the empty cell shown in Fig. 4.25 and the transmittance calculated from the window thickness obtained by gamma ray measurement.

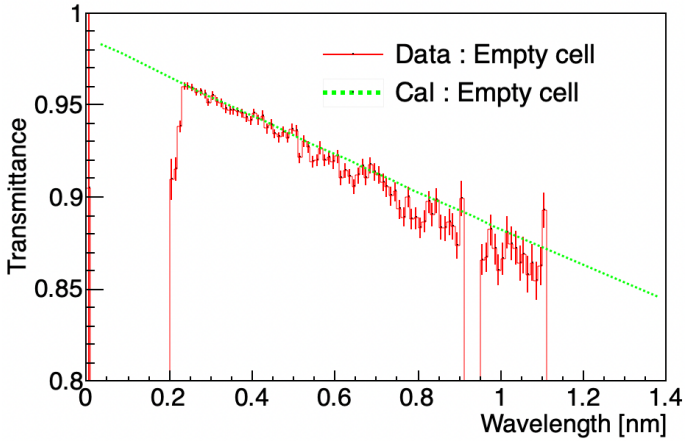

Figure 4.25: Transmittance spectrum of an empty cell. (red line) measured value, (green line) calculation results based on the thickness of the V-Ni window

Since there is currently no accuracy in extracting density fluctuations from the transmittance, the multiplication factor from the average density is evaluated from the scattering intensity obtained from the simulation explained in the following Sec. 4.4.3.

4.4 Analysis of Momentum Transfer

In this chapter, the details of the analysis of the SANS data, the MC simulations, and the method to extract the results on the coupling constant of the unknown interaction will be explained.

The momentum transfer of V-nanopowder is calculated from the measured position distribution and wavelength of the scattered neutrons explained in Sec. 4.2. Figure 4.26 shows the momentum transfer distribution, and Fig. 4.27 shows the results calculated with the TOF distribution of the FOL data.

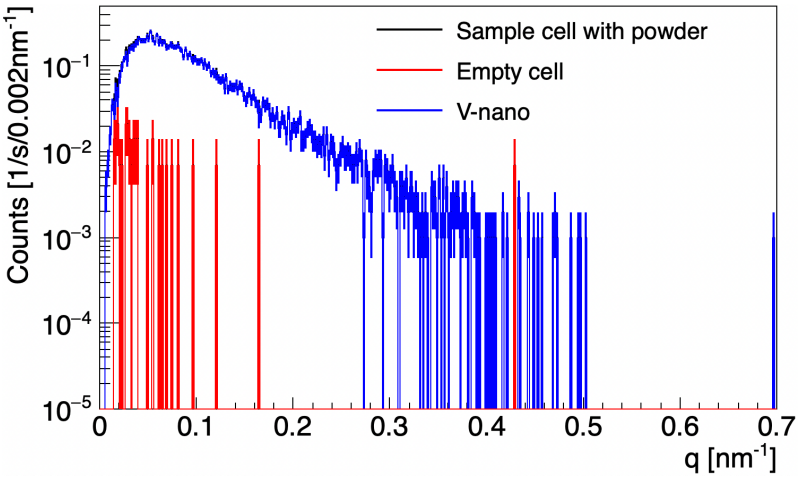

Figure 4.26: Momentum transfer distribution of each sample.

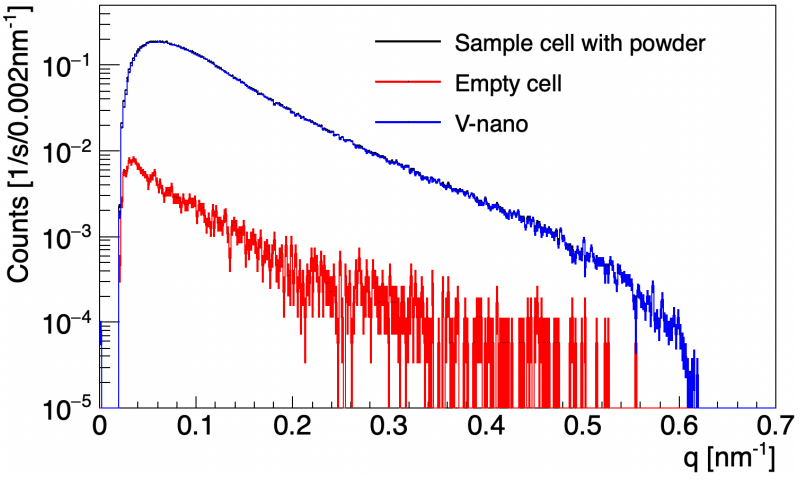

Figure 4.27: Momentum transfer distribution calculated with the TOF distribution of the FOL data.

The momentum transfer distribution for the sample cell and empty cell data shown in Figs. 4.26 and 4.27 are given by Eqs. (4.8) and (4.9), respectively.

$$I_{\mathrm{S+C}}(q,\lambda,\Omega) = C_{\mathrm{EXP}}(\Omega)T_{\mathrm{S+C}}(\lambda)\left[\frac{d\Sigma^{\mathrm{S+C}}(q)}{d\Omega} + \frac{d\Sigma^{\mathrm{C}}(q)}{d\Omega}\right]d\epsilon(\lambda)I_{\mathrm{in}}(\lambda) \tag{4.8}$$

$$I_{\mathrm{C}}(q,\lambda,\Omega) = C_{\mathrm{EXP}}(\Omega)T_{\mathrm{C}}(\lambda)\frac{d\Sigma^{\mathrm{C}}(q)}{d\Omega}d\epsilon(\lambda)I_{\mathrm{in}}(\lambda) \tag{4.9}$$

Here, $I_{\mathrm{S+C}}(q,\lambda,\Omega)$ and $I_{\mathrm{C}}(q,\lambda,\Omega)$ are the neutron intensities as a function of q, λ, and detector solid angle Ω, with sample and cell and with cell only, respectively. $C_{\mathrm{EXP}}(\Omega)$ is the solid angle of the detector from the target, $T_{\mathrm{S+C}}(\lambda)$ and $T_{\mathrm{C}}(\lambda)$ are the transmittances of the sample cell and empty cell, respectively. $d\Sigma^{\mathrm{S+C}}(q)/d\Omega$ and $d\Sigma^{\mathrm{C}}(q)/d\Omega$ are the differential macroscopic cross sections (differential cross sections per unit volume: [b/m^3/sr]) of the sample and the cell, and the cell only, respectively. d is the thickness of the sample cell, $\epsilon(\lambda)$ is the detector efficiency, and $I_{\mathrm{in}}(\lambda)$ is the incident neutron intensity. Here, the events from scattering only from V nanoparticles can be obtained by correcting the number of scattering events from the sample cell and the empty cell by the transmittance. In this case, the correction is made using the following Eq. (4.10).

$$I_{\mathrm{S}}(q) = \frac{I_{\mathrm{S+C}}(q)}{T_{\mathrm{S+C}}(\lambda)} - \frac{I_{\mathrm{C}}(q)}{T_{\mathrm{C}}(\lambda)} \tag{4.10}$$

$I_{\mathrm{S}}(q)$ is the scattering intensity from the V nanoparticle.

To evaluate the q dependence due to the Yukawa interaction, all the terms that depend on the angle and wavelength that define the momentum transfer must be corrected. The effect of the solid angle $C_{\mathrm{EXP}}(\Omega)$ is difficult to solve analytically because the scattering measurements were performed with an incident neutron beam using a line collimator. Therefore, we use MC simulation to calculate the position distribution of scattered neutrons in the experiment using incident neutrons collimated by a line slit. The momentum transfer calculation using the frame overlap data is not strictly correct because it includes events with T0F $>$ 50 ms. On the other hand, this data has 130 times better statistics than the data shown in Fig. 4.12, which shows the timing of the proton beam transport to the MR measured with a period of 130 pulses = 5.2 sec. By dividing the TOF in the MC simulation by the pulse interval 40 ms of MLF proton beam, the TOF distribution and the momentum transfer distribution were obtained and compared with the ones obtained from the experimental FOL data.

4.4.1 Monte Carlo Simulation of the SANS Experiment

As mentioned in the beginning of this section, the q-distribution expected from only the nuclear scattering is necessary to extract the evidence of unknown interaction from the measured spectrum. The expected spectrum was generated by means of the Monte Carlo method based on the formula of the differential cross section discussed in Chapter 2 and the known parameters of the experimental condition together with available data of the neutron scattering lengths for the elements contained in target materials.

The basic structure of the Monte Carlo simulation is based on a program developed by collaborator Haddock, which was used in the analysis of our previous noble gas experiment [24]. We employd a calculation code [7] modified by Dr. Nakabe from JAEA so as to take into account the differential cross sections of nanoparticles, the slit conditions, and target conditions used in this experiment. Furthermore, I built the MC simulation by incorporating additional information on the size distribution, cross section, and slit conditions of the V nanoparticles. The parameters used in this MC simulation are shown in Table 4.5.

Table 4.5: Summary of physical parameters used in MC simulation

	value	reference
Intensity of incident neutron	14.186±0.004 kcps	Fig. 4.2
Form Factor and Particle size	Spherical particle	Fig. 2.21
Coherent scattering length	0.719 ± 0.023 fm	Table 2.10
Absorption cross secion	4.64 ± 0.87 fm	""
Incoherent scattering cross section	4.08 ± 0.02 b	""
Diffuse scattering cross section	0.83 b	""
Amount of V nanopowder	15.6 ± 0.1 mg	Table 3.4
Target thickness	300 μm	-

The calculation procedure followed the flowchart shown in Fig. 4.28. The TOF of the incident neutron used in the simulation uses the experimental data from this experiment, and the velocity of the incident neutron is calculated from the TOF information. Based on Fig. 3.11, the initial position (x_0, y_0) of the incident neutron is randomly determined from the width of the most upstream 2D slit, and then the coordinates (x_1, y_1) at the position of the 1st Cd collimator and the coordinates (x_2, y_2) at the position of the 2nd Cd collimator are determined to determine the path of the incident neutron. Then, the interaction with the sample is determined by the mean free path based on each cross section. The absorption probability depends on the wavelength of the incident neutron and is determined from the measured data for each neutron velocity. In addition, the coherent scattering cross section based on momentum transfer is determined by the cross

section integrated over the total solid angle, and the reaction probability is determined by the wavelength of the incident neutron. Finally, the position and time information of the scattered and transmitted neutrons are calculated taking into account the detection area and position resolution of the FRP detector at the most downstream. These steps were repeated many times (10^9 times in typical) to obtain sufficient statistics.

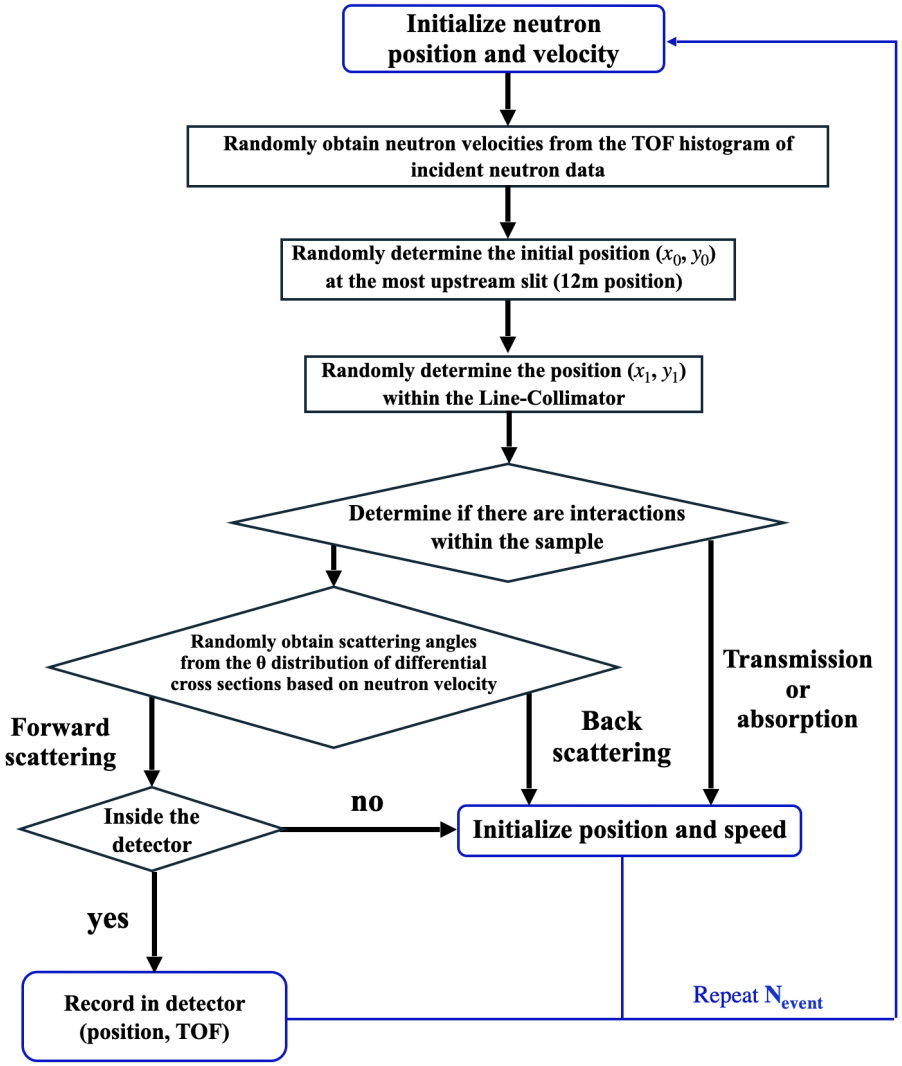

Figure 4.28: the flowchart of the MC simulation calculation [7]

To discuss the absolute intensity of the simulation, it can be seen that the transmission of the sample powder in the sample cell is more than twice the average density as discussed in Sec. 4.3.3. In the next Sec. 4.4.2, the process of determining the effective density of V-nanopowder is explained.

4.4.2 Effects Two-body Correlation Due to Aggregation

Before comparing the intensities of momentum transfer distributions simulated from SAXS particle size distributions, we consider the momentum transfer region where the effects of powder agglomeration can be seen.

The particle size distribution used in the simulation was obtained from a SAXS measurement in which the nanopowder sample was packed with a very small tension through the window of the sample cell, as shown in Fig. 2.15. This is expected to be significantly different from the size distribution of the real sample used in the SANS measurement in which the powder was packed with a non-small tension through the window of the cell, as shown in Fig. 3.27. Therefore, in the present case, it is necessary to consider the effect of the aggregation onto the momentum transfer when the powders are in close proximity to each other in order to compare it with the momentum transfer obtained in the SANS experiment.

The simplest aggregation model is the one that the effect of two-particle correlation is taken into account using the Percus-Yevick function [49, 50, 51]. This model is commonly used for analyzing small-angle neutron scattering (SANS) spectra from interacting colloids containing a continuous distribution of particle sizes in a liquid dispersion. A conceptual diagram of the effect of aggregation is shown in Fig. 4.29.

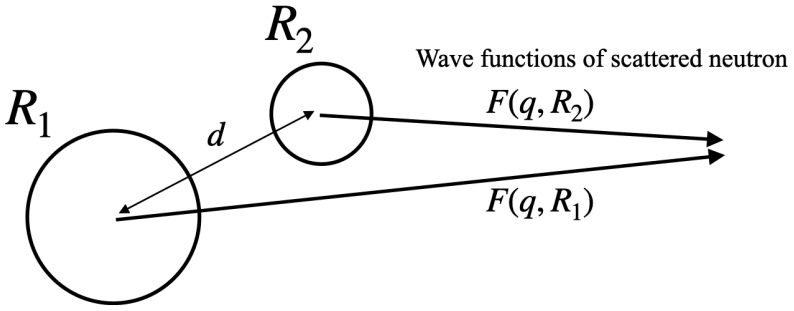

Figure 4.29: Effect of two-particle correlation due to nearby particles

Here, R_1 and R_2 are the radii of different particles, and d represents the distance between the particles. When two-particle correlation exists, the spatial distribution of particles is no longer random, and the interference of scattered waves changes due to interactions between particles. When the density of nanoparticles packed in a cell is high, it is necessary to consider the effect of interference of scattered waves between nearby particles. This is basically derived following the method explained in [49]. In this model, we consider N_P particles dispersed in a homogeneous solvent. First, we describe the effect of the structure factor using the differential cross section of coherent scattering. In the following discussion,

we assume that the size and prientation of the particles are independent of their position. In this case,

$$\frac{d\Sigma}{d\Omega}(\bar{Q}) = V^{-1}\left\langle \sum_{i=1}^{N_p}\sum_{i'=1}^{N_p}\langle F_i(\bar{Q})F_{i'}{}^*(\bar{Q})\rangle \times \exp[i\bar{Q}\cdot(\bar{R}_i - \bar{R}'_i)]\right\rangle, \tag{4.11}$$

$\langle F_i(\bar{Q})F_{i'}{}^*(\bar{Q})\rangle$ in Eq. (4.11) represents the average weighted by the distribution of the particle size and orientation.

$$\langle F_i(\bar{Q})F_{i'}{}^*(\bar{Q})\rangle = [\langle|F(\bar{Q})|^2\rangle - |\langle F(\bar{Q})\rangle|^2]\delta_{ii'} + |\langle F(\bar{Q})\rangle|^2. \tag{4.12}$$

And then, Eq. (4.11) is expressed as follow,

$$\frac{d\Sigma}{d\Omega}(\bar{Q}) = n_p[\langle|F(\bar{Q})|^2\rangle - |\langle F(\bar{Q})\rangle|^2]\delta_{ii'} + n_p S(\bar{Q}), \tag{4.13}$$

Here, $n_p = N_p/V$ is average number density of particle in the cell. $S(\bar{Q})$ is structure factor of two-body correlation as defined as follows,

$$S(\bar{Q}) = N_p^{-1}\left\langle \sum_{i=1}^{N_p}\sum_{i'=1}^{N_p}\exp[i\bar{Q}\cdot(\bar{R}_i - \bar{R}_{i'})]\right\rangle \tag{4.14}$$

To make easier to understand, Eq. (4.13) is transformed as follows:

$$\frac{d\Sigma}{d\Omega}(\bar{Q}) = n_p P(\bar{Q})S'(\bar{Q}), \tag{4.15}$$

Each term in the Eq. (4.15) are defined as follows,

$$P(\bar{Q}) = \langle|F(\bar{Q})|^2\rangle \tag{4.16}$$

$$S'(\bar{Q}) = 1 + \beta(\bar{Q})[S(\bar{Q}) - 1], \tag{4.17}$$

$$\beta(\bar{Q}) = |\langle F(\bar{Q})\rangle|^2/\langle|F(\bar{Q})|^2\rangle, \tag{4.18}$$

$S'(Q)$ acts as an apparent interparticle structure factor. $\beta(\bar{Q})$ is a factor between 0 and 1 that depends on Q and suppresses the oscillation of the real structure factor $S(Q)$ in the scattering spectrum of polydisperse or non-spherical particle systems. The effect of particle packing ratio on the structure factor can be defined by the following Eq. (4.19) [52]:

$$S'(q) = 1 + \frac{|\langle F(\bar{q})\rangle|^2}{\langle|F(\bar{q})|^2\rangle}\left[\sum_{i=1}^{N}\left(\frac{n_i S(q, R_i, \eta)}{\sum_i n_i}\right) - 1\right] \tag{4.19}$$

$S'(q)$ is the interparticle structure factor of the Percus-Yevick (PY) hard-sphere mode. n_i, $F(q, R_i)$ and $S(q, R_i, \eta)$ represent the frequency distribution of particle size i, the form factor of spheres and the structure factor in monopartite form, respectively. $|\langle F(\bar{q})\rangle|^2$ and $\langle|F(\bar{q})|^2\rangle$ in Eq. (4.19) are defined as follows: $|\langle F(\bar{q})\rangle|^2$ is expressed as a superposition of coherent scattered waves of different particle sizes.

$$\langle|F(\bar{q})|^2\rangle = \int |F(q,R)|^2 f(R)\,\mathrm{d}R \tag{4.20}$$

$$|\langle F(\bar{q})\rangle|^2 = \sum_i^N f(R_i)F^*(q,R_i)\sum_j^N f(R_j)F(q,R_j) = \left|\int F(q,R)f(R)\,\mathrm{d}R\right|^2 \tag{4.21}$$

Here, $f(R)$ is the number density of nanoparticles of radius R and N is the bin number of V-nanoparticles size distribution. For the simplest model which assumes the particles are hard spheres, $S(q, R_i, \eta)$ is expressed as Eq. (4.22) using the Percus-Yevick approximation.

$$\begin{aligned} S(q) &= 1 + \rho\int_V [g(r)+1]e^{iq\dot{r}}dV \\ &= 1 - \frac{1}{1-c(q,\sigma,\eta)} \end{aligned} \tag{4.22}$$

$$\begin{aligned} c(q,\sigma,\eta) = -\frac{24\eta}{(1-\eta^4)(q\sigma)^3}\Bigg[&(1+2\eta)^2(\sin(q\sigma)-q\sigma\cos(q\sigma)) \\ &- 6\eta\left(1+\frac{\eta}{2}\right)^2\left[2\sin(q\sigma)-q\sigma\cos(q\sigma)-\frac{2(1-\cos(q\sigma))}{q\sigma}\right] \\ &+ \frac{1}{2}\eta(1+2\eta)^2\Bigg[\left(4-\frac{24}{(q\sigma)^2}\sin(q\sigma)\right) \\ &- \left(q\sigma-\frac{12}{q\sigma}\cos(q\sigma)+\frac{24(1-\cos(q\sigma))}{(q\sigma)^3}\right)\Bigg]\Bigg] \end{aligned} \tag{4.23}$$

Here, ρ is the average particle density, $g(r)$ is the two-particle correlation function, $\rho g(r)$ gives the particle number density function, $\sigma = 2R$ is the particle diameter, and η is the particle packing fraction. The filling rate of V nanopowder is 11.4 % from the powder weight and cell volume shown in Table 3.4. The $S'(q)$ function in this case is shown in Fig. 4.30. As shown in Fig. 4.30, the effect of two-particle correlation is maximized when the momentum transfer is $0.1\,\mathrm{nm}^{-1}$, and the effect of aggregation is not observed in the range of $\mathrm{q} > 0.3\,\mathrm{nm}^{-1}$.

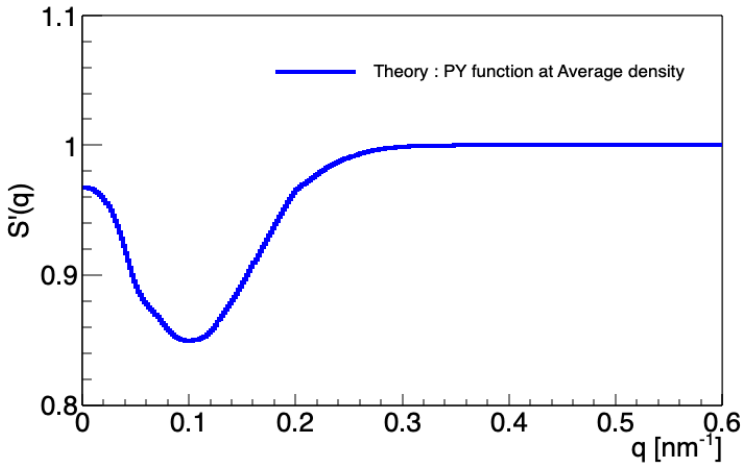

Figure 4.30: q dependence of S'(q) calculated from the average density

4.4.3 Determination of the Effective Density

As discussed in Fig. 4.30, the enhancement in the target density from the nominal value is determined by comparing the scattering intensity of the simulation and the measured data in the region of $q > 0.3\,\mathrm{nm}^{-1}$ where the aggregation effect is negligible small. Figure 4.31 shows the fitting result of the simulated q distribution to the measured data in the region $q > 0.3\,\mathrm{nm}^{-1}$.

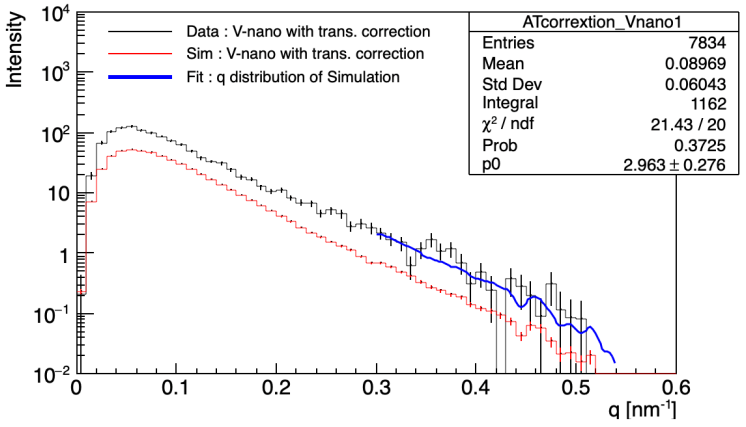

Figure 4.31: Results of fitting for the measured data with the momentum transfer distribution simulated with the average density

The ratio of the effective target density to the nominal density was determined from the fitting results is 2.963 ± 0.276. The standard deviation of the density fluctuation is 9.3 %. It should be noted that the presently obtained value is in good agreement with the one estimated by the analysis of γ-ray and neutron transmittance data.

4.4.4 q-dependence of the Yukawa Interaction

The q-dependence of the Yukawa interaction is calculated based on the particle size distribution of V nanopowder and is shown in Fig. 4.32.

The q-dependence of the Yukawa interaction is not significant for $q > 0.3\,nm^{-1}$. As can be found in Fig. 4.32, the effect of agglomeration and Yukawa interaction is negligibly small in the region of $q > 0.3\,nm^{-1}$, where the effect of aggregation is also negligible as discussed above. Therefore, the multiplication factor of the effective target density is considered to be safely determined by comparing the scattering intensities of the measurement and the MC calculation.

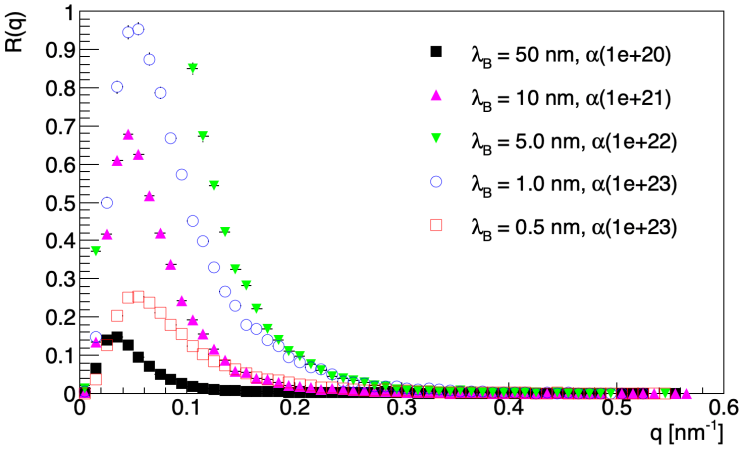

Figure 4.32: The q dependence of the Yukawa interaction at each interaction length λ_B calculated from the particle size distribution of V nanopowder. The vertical axis represents $R(q) = 2b_Y(q)/b_{coh}$.

4.4.5 Simulation Calculation Error

Table 4.6 shows a list of the systematic error of the parameters used in the simulation calculations.

Table 4.6: Summary of errors of physical parameters used in simulation.

	systematic error	reference
Particle size distribution function	0.26 %	Fig. 2.22
Effective target density	9.3 %	Fig. 4.31
Structure factor of PY function	< 2 %	Fig. 4.34
Neutron transmittance	1%	Fig. 4.33
Coh. nuclear scattering length	3.2 %	Table 2.10
Daed time of incident neutron	0.375 %	Sec. 4.1.1 & 3.6.2

Among the errors, the particle size distribution function obtained from the fit of the SAXS data and the effective target density obtained from the fit of the SANS data are determined by the error of the standard deviation of the data following a Gaussian distribution.

In addition, the aggregation model assumed in the simulation is also a function with density as a parameter. Therefore, the aggregation model also needs to consider the variance due to the error of the effective target density. Other errors occur due to the discrepancy between the measured data and the theoretical curve. This effect is explained in Sec. 4.4.6.

Next, Fig. 4.33 shows the neutron transmission through a V-nanopowder sample calculated taking this density change into account, compared with the simulation results. The effective target density and the measured transmission differ by 1 % in the range of $\lambda = 0.2 \sim 0.6$ nm. Since we could not find the reason for this disagreement, we included the difference in the systematic errors.

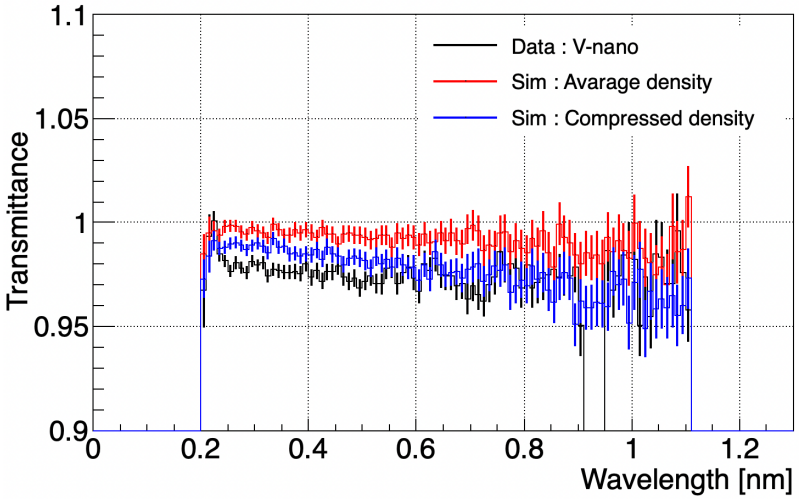

Figure 4.33: Comparison of transmittance calculated from effective density and average density with measured data. (black line) measurement data of V-nanopowder, (red line) simulation results from average density, (blue line) simulation results from effective target density.

The error in the nuclear scattering length of V nanoparticles is determined by the error in elemental analysis, which is determined by performing multiple measurements. On the other hand, the uncertainties of the coherent neutron scattering length of V and O, who are the two major components of the nanoparticles, are systematic errors according to Refs.[39, 53].

As mentioned above, the parameters used in the simulation calculations in this study contain systematic errors. In order to obtain the limit of 95 % confidence level (C.L.) after

taking these into consideration, when deriving the fitting function Eq. (5.3) for evaluating the Yukawa interaction described from Eq. (5.4), the parameters including systematic errors are set to arbitrary values (determined by random numbers) within the error range. The limit with 95% C.L. was determined from the probability distribution of α which was obtained via the fitting for the experimental SANS spectrum with the spectrum generated by the MC simulation using the effective target density ρ as a fitting parameter.

The errors of the parameters used to calculate the MC simulation discussed in the previous section are only those that can be treated as statistical errors, and the upper limit of 1σ is evaluated. To consider the systematic error, the experimental spectrum was fitted with many fitting spectra generated by the simulation calculations with different parameters having distributions corresponding to those systematic errors. Through those fittings, a probability distribution for α was produced, and from that the upper limits for 95 % C.L. were determined for various values of λ_B.

Finally, regarding the effect of the dead time of the incident neutrons, as shown in Sec. 3.6.2, the dead time is 12.5 μs/event. Since the maximum count rate of the divided measurement data shown in Fig. 4.1 is approximately 300 cps, the counting loss rate is $300 \times (12.5 \times 10^{-6}) = 0.375\%$. This is sufficiently smaller than the relative accuracy of 1%, which is the correction standard in this analysis, so dead time correction is considered unnecessary.

4.4.6 Effect of effective density on aggregation

How the structure factor function calculated by Eq. (4.19) varies from the effective target density and its standard deviation is shown in Fig. 4.34.

Figure 4.34 shows that the density fluctuations are maximum in the region $q = 0.1\,\mathrm{nm}^{-1}$. As a result, the scattering intensity in this region varies by 2 % due to the uncertainty in the effective target density. The structure factor $S'(q,\rho)$ depends on the effective density ρ. To take into account this correlation, we took the first-order term in the Taylor expansion of $S'(q,\rho)$ as shown in Eq. (4.24).

$$\begin{aligned} S'(q,\rho') &= S'(q,\rho) + \frac{\partial S'(q,\rho)}{\partial \rho}(\rho' - \rho) \\ \delta S'(q,\rho') &= S'(q,\rho') - S'(q,\rho) = \frac{\partial S'(q,\rho)}{\partial \rho}(\rho' - \rho) \end{aligned} \tag{4.24}$$

Here, ρ is the central value of the density and ρ' is the parameter of the density. Next, regarding $\partial S'(q,\rho)/\partial\rho$,

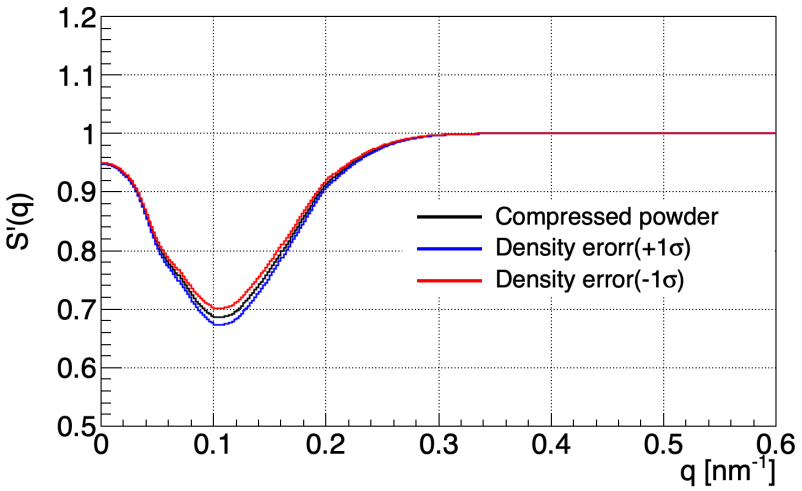

Figure 4.34: Fluctuations of the structure factor S′(q) calculated from the fitting results shown in Fig. 4.31. (black line) S′(q) function obtained with the target density of 2.963 times the nominal density, (red and blue line) $\pm 1\sigma$ shift of S'(q) due to density error.

$$\frac{\delta S'(q,\rho)}{\delta \rho} = \frac{\partial S'(q,\rho)}{\partial \rho} \tag{4.25}$$

Therefore,

$$\left(\frac{\frac{\delta S'(q,\rho)}{S'(q,\rho)}}{\frac{\delta \rho}{\rho}} \right) = \frac{\partial S'(q,\rho)}{\partial \rho} \frac{\rho}{S'(q,\rho)} \tag{4.26}$$

Here, $\delta S'(q,\rho) = |S'(q,\rho \pm 0.093\rho) - S'(q,\rho)|$ and $\delta\rho = |\rho' - \rho| = 0.093\rho$ (error of effective density : 9.3 %),

$$\frac{\partial S'(q,\rho)}{\partial \rho} = \frac{|S'(q,\rho \pm 0.093\rho) - S'(q,\rho)|}{0.093} \frac{1}{\rho} \tag{4.27}$$

Substituting the obtained Eq. (4.28) into $\partial S'(q,\rho)/\partial\rho$ in Eq. (4.25),

$$\delta S'(q,\rho') = \frac{|S'(q,\rho \pm 0.093\rho) - S'(q,\rho)|}{0.093} \left(\frac{\rho'}{\rho} - 1 \right) \tag{4.28}$$

Where, $S'(q,\rho \pm 0.093\rho)$ is the value with density error $\pm 1\sigma$ shown in Fig. 4.34. The variation in the structure factor due to $\delta S'(q,\rho')$ is treated as a systematic error, and will be verified in the next chapter using Gaussian random numbers from the error in the effective density.

4.4.7 Comparison of Nuclear Scattering Simulation with SANS Data

In this section, the experimental neutron scattering spectrum was compared with the calculated ones using parameters given in Table 4.5. In this calculation the effective target density determined in Sec. 4.4.3 was employed, and the aggregation effect was considered using the model described in Sec. 4.4.6.

First, Fig. 4.35 shows the experimental momentum-transfer distribution of the scattered neutron intensity from the non-FOL data together with the result of the simulation. Here the simulation included only the statistical error. As can be found in 4.35, the effect of the aggregation is quite significant, and it should be taken into account to analyze the experimental data.

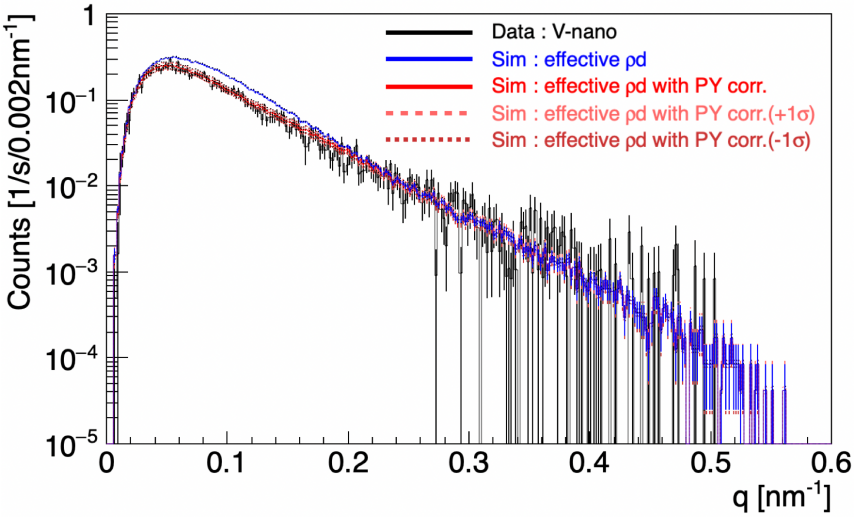

Figure 4.35: Comparison of SANS data and simulation for momentum transfer of V nanoparticles.(black line) SANS data, (red and blue line) simulations with and without correction for aggregation effect.

Figure 4.36 and 4.37 are the comparisons of the experimental and simulated distributions of the wavelength and the detected position of scattered neutrons, respectively.

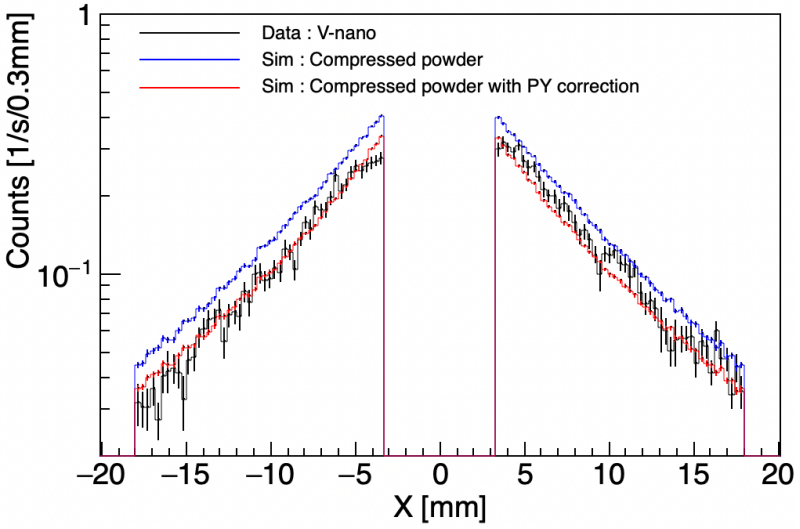

Figure 4.36: Position distributions used to calculate the q-distribution in Fig. 4.35.

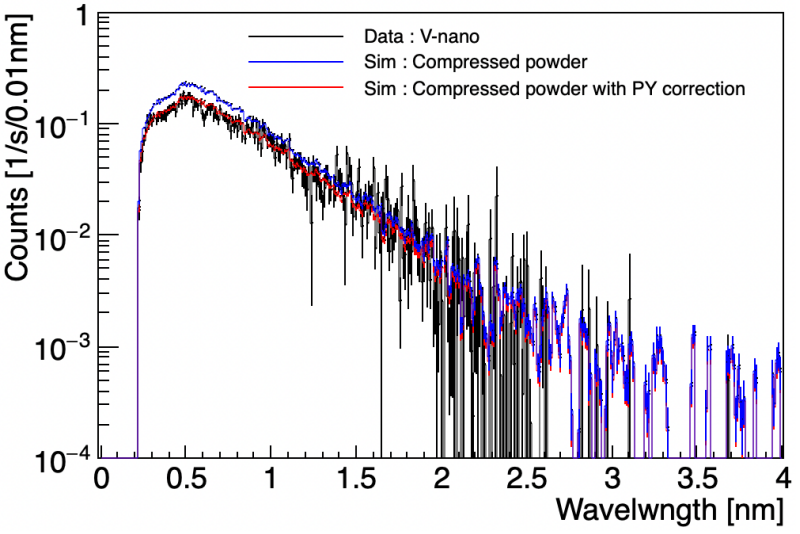

Figure 4.37: Wavelength distributions of scattered neutron used to calculate the q-distribution in Fig. 4.35.

Simulations for FOL data

Since the FOL data contains about 130 times larger number of events than the non-FOL data, it is expected to give more better sensitivity to the unknown interaction.

To analyze the FOL data, it is necessary to compare with the MC simulation. Basically only the difference between the non-FOL data and the FOL data is that in the former the measured TOF value is the real TOF, on the other hand, in the latter the measured TOF value is the remainder of the real TOF divided by 40 ms which is the time interval between proton pulses of the MLF. Therefore, the MC simulation for the FOL data is performed in almost same manner to the non-FOL case and finally the TOF value is changed event-by-event to the remainder of the division by 40 ms. All the wavelength-dependent effects such as attenuation in the target and aggregation were taken into calculation using the real wavelength which corresponds to the real TOF before making the conversion from the real TOF to the one in the FOL case. The wavelength calculated using this FOL data is hereafter defined as λ_{FOL}. Figure 4.38 compares the q-distribution of the FOL data (black) and the result of the MC simulation with (red) and without (blue) the aggregation effect.

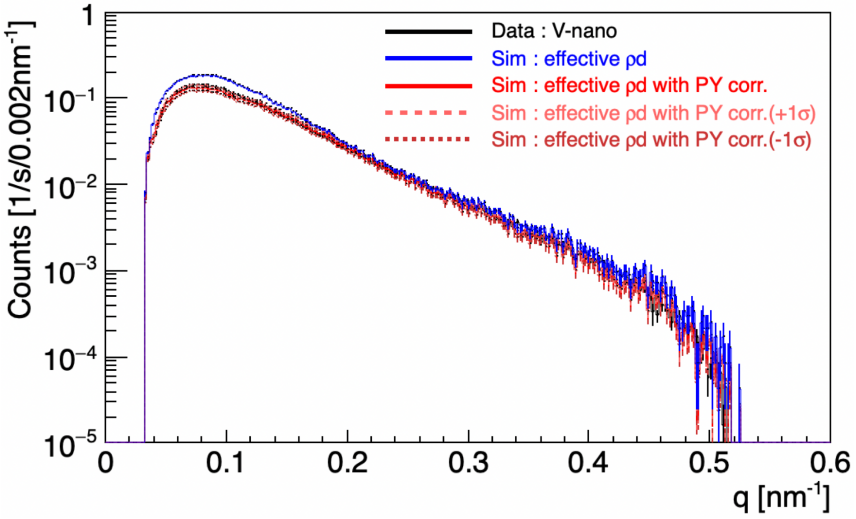

Figure 4.38: Comparison of the q distribution from the FOL data. (black line) SANS data, (red and blue line) simulations for FOL cases with and without correction for aggregation effect.

To check the reliability of the present MC simulation, the position and wavelength distributions of the scattered neutrons from the FOL data and the MC simulation were compared as shown in Figs. 4.39 and 4.40, respectively.

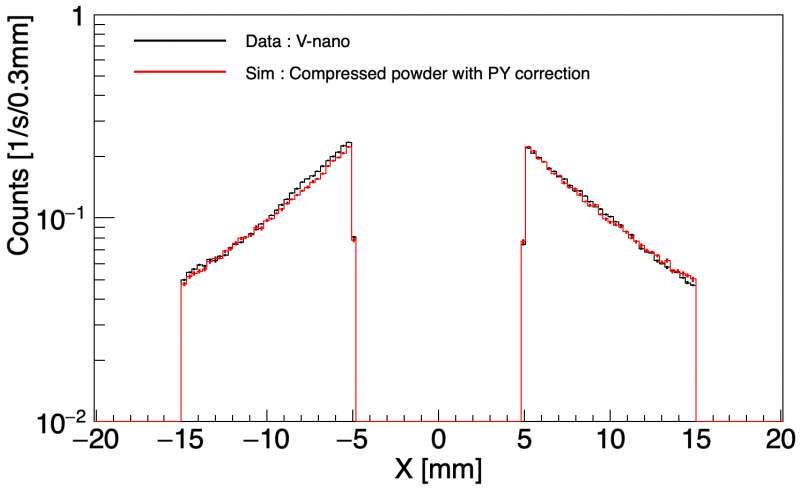

Figure 4.39: The position distribution used to calculate the q-distribution of Fig. 4.38.

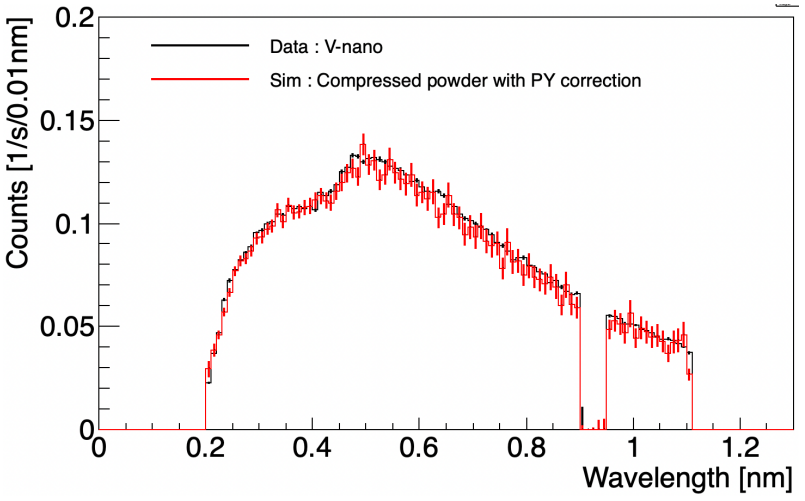

Figure 4.40: Wavelength distributions of scattered neutron used to calculate the q-distribution in Fig. 4.38.

Chapter 5

Results and Discussion

This chapter discusses how to evaluate unknown interactions from measured data and the challenges of increasing the sensitivity of this method.

In Sec. 5.1.1, the q dependence of unknown interactions evaluated from the ratio of measured data to nuclear scattering simulations will be presented. Also, method for determining α is explained. Furthermore, as explained in Sec. 5.1.2 and Sec. 5.1.3, it should be noted that when comparing measured data with simulations, there remains q dependence that cannot be explained by the systematic errors considered and the q dependence of unknown interactions. The upper limit evaluated as a benchmark result is presented in Sec. 5.2. Finally, in Sec. 5.2.1, the methods for improving the present experimental sensitivity are discussed based on the origins of systematic errors studied in the present work.

5.1 Results

In this section, a method for evaluating the q dependence due to the Yukawa interaction from the momentum transfer distribution calculated in the previous Sec. 4.4.6 is explained.

5.1.1 Evaluation Method of the Yukawa Interaction

The scattering intensities $I_{\mathrm{Data}}(\Omega, R, q)$ from measurements which may include the effects of unknown interactions, and $I_{\mathrm{Sim}}(\Omega, R, q)$ from Monte Carlo calculations of nuclear

scattering only, are given by Eqs. (5.1) and (5.2).

$$\begin{aligned} I_{\mathrm{Data}}(\Omega,\lambda,q) =& C_{\mathrm{Data}}(\Omega)\cdot T(\lambda)\cdot \rho_{\mathrm{powder}}\cdot d \\ & \left[S'(q)\cdot \int_R n(R)\frac{\left[V(R)\cdot \rho_{atom}(b_{\mathrm{coh}}+b_{\mathrm{EM}}(q)+b_{\mathrm{Y}}(q))\right]^2}{N_{\mathrm{atom}}(R)} F(q,R)^2 dR \right. \\ & \left. + \sigma_{\mathrm{inc}}+\sigma_{\mathrm{diff}} \right] \varepsilon(\lambda)\cdot I_{\mathrm{in}}(\lambda) + \mathrm{BG}(\lambda) \end{aligned} \tag{5.1}$$

$$\begin{aligned} I_{\mathrm{Sim}}(\Omega,\lambda,q) =& C_{\mathrm{Sim}}(\Omega)\cdot T(\lambda)\cdot \rho_{\mathrm{powder}}\cdot d \\ & \left[S'(q)\cdot \int_R n(R)\frac{\left[V(R)\cdot \rho_{\mathrm{atoms}}\cdot b_{\mathrm{coh}}\right]^2}{N_{\mathrm{atom}}(R)} F(q,R)^2 dR + \sigma_{\mathrm{inc}}+\sigma_{\mathrm{diff}} \right] \varepsilon(\lambda)\cdot I_{\mathrm{in}}(\lambda) \end{aligned} \tag{5.2}$$

where, $C_{\mathrm{Data}}(\Omega)$ and $C_{\mathrm{Sim}}(\Omega)$ are coefficients that consider the solid angle of the detector's receiving section, ρ_{powder} is the number density of atoms in the sample cell, $n(R)$ is the size distribution of nanoparticles as a function of radius R, $V(R)$ is the volume of V nanoparticles with radius R, and ρ_{atoms} is the atomic number density of V nanoparticles. b_{coh}, b_{EM}, $b_{\mathrm{Y}}(q)$, and are the coherent nuclear scattering length, coherent electron scattering length, and coherent scattering length due to unknown interactions, respectively. σ_{inc} and σ_{diff} represent the cross sections for incoherent and diffuse nuclear scattering. $\epsilon(\lambda)$ and $I_{\mathrm{in}}(\lambda)$ are the detector efficiency and the incident beam intensity for the neutron wavelength λ, respectively. $\mathrm{BG}(\lambda)$ represents the background spectrum as a function of λ. Taking the ratio of these equations, we obtain Eq. (4.23) when $\sigma_{\mathrm{coh}}(q) >> \sigma_{\mathrm{inc}}+\sigma_{\mathrm{diff}}$ and $\sigma_{\mathrm{coh,nuclear}} >> \sigma_{\mathrm{EM,coh}}$.

$$\begin{aligned} R(q) &= \frac{I_{\mathrm{Data}}(\Omega,R,q)}{I_{\mathrm{Sim}}(\Omega,R,q)} \\ &\approx \left[1+\frac{b_{\mathrm{Y}}(q)}{b_{\mathrm{coh(N)}}}\right]^2 \frac{C_{\mathrm{Data}}(\Omega)}{C_{\mathrm{Sim}}(\Omega)}\frac{\rho_{\mathrm{powder}}d}{\rho_{\mathrm{powder}}d}\frac{T(\lambda)}{T(\lambda)}\frac{n(R)}{n(R)}\left(\frac{F(q,R)}{F(q,R)}\right)^2\frac{S'(q,R,\rho)}{S'(q,R,\rho)}\frac{I_{\mathrm{in}}(\lambda)}{I_{\mathrm{in}}(\lambda)} \\ &\approx \left[1+\frac{2b_{\mathrm{Y}}(q)}{b_{\mathrm{coh}}}\right]\times P_{\mathrm{sys}}(q) \end{aligned} \tag{5.3}$$

It should be noted that the ratios according to $C_{\mathrm{Data}}(\Omega)/C_{\mathrm{Sim}}(\Omega)$ do not depend on the effects of unknown interactions, but only on the experimental conditions. Thus, these ratios are constant for a given experimental condition, and by examining only the q dependence of the ratio $R(q)$, one can find evidence of unknown interactions, without depending on

the accuracy of other experimental parameters.

The last term in Eq. (5.3) is approximated, since $b_{\mathrm{Y}}(q)$ is expected to be much smaller than b_{coh}. $P_{\mathrm{sys}}(q)$ is a coefficient that does not depend on unknown interactions, and is a term that includes the errors of each parameter used in the simulations shown in Table 4.6. Next, the q dependence of the Yukawa interaction in parentheses for R(q) in Eq. (5.3) is fitted with Eq. (5.4).

$$f(q) = 1 + P_{\alpha}\frac{2b_{\mathrm{Y}}(q)}{b_{\mathrm{coh}}} \tag{5.4}$$

P_{α} represents the relative strength of the effect of the unknown interaction. The second term in the brackets in Eq. (5.4) is the q-dependent term of the unknown interaction contained in the R(q) distribution. The coefficient $2b_{\mathrm{Y}}(q)/b_{\mathrm{coh}}$ is pre-calculated by setting appropriate λ_B and α. The most probable value of P_{α} was determined by fitting R(q) with Eq. (5.4) for various values of λ_B. Figure 5.1 is $2b_{\mathrm{Y}}(q)/b_{\mathrm{coh}}$ when the Yukawa interaction length λ_B is divided into 5 parts in the range from 50 nm to 0.5 nm and changed.

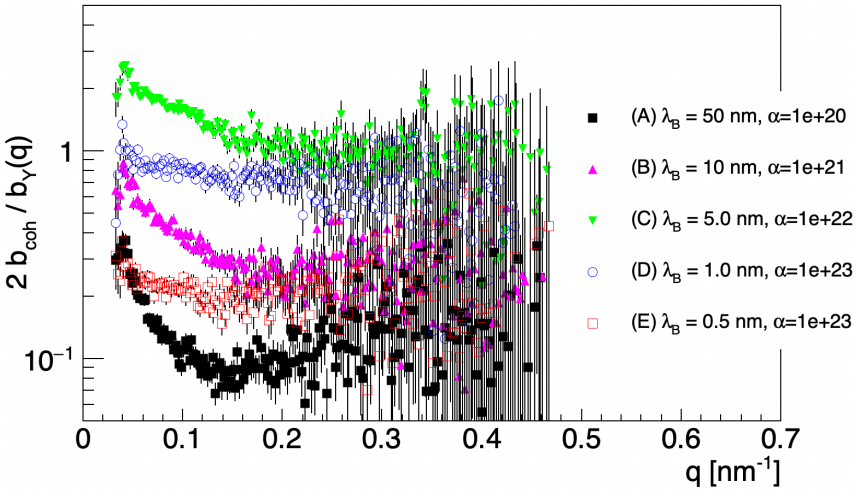

Figure 5.1: The q dependence of $2b_{\mathrm{Y}}(q)/b_{\mathrm{coh(N)}}$ for each λ_B.

5.1.2 Systematic Error of q dependence

Figure 5.2 is the calculation result of Eq. (5.3). Figure 5.2 is analyzed using the measured data of 25 Hz pulse shown in Fig. 4.38. In this case, $R(q)$ shown in Fig. 5.2 includes only

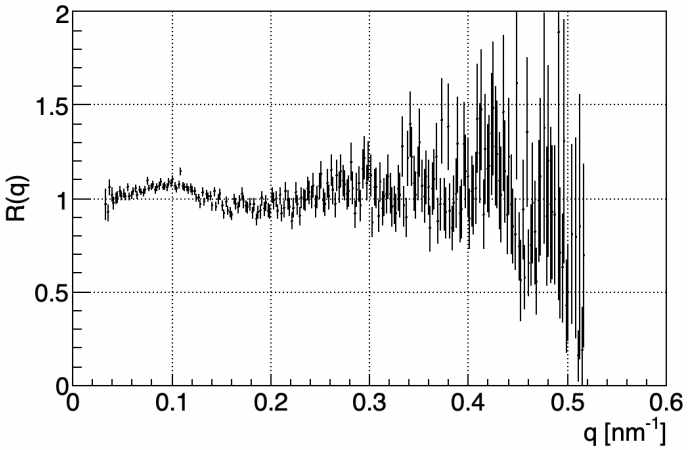

Figure 5.2: The q dependence of R(q) calculated with FOL data.

statistical error. Therefore, P_{alpha} obtained by fitting Eq. (5.4) is evaluated by reduced chi-square to obtain the standard deviation σ with 68 % confidence. However, it is important to take into account that the fit results for $P_{\mathrm{sys}}(q)$ contained in Eq. (5.3) may change due to systematic errors contained in the parameters of the simulation calculation.

The distribution around q = 0.1 nm^{-1} seen in Fig. 5.2 shows that the ratio value deviates from 1 beyond statistical error. This q-dependent variation of about 9 % cannot currently be explained by the model including the systematic errors listed in Table 4.6, and is also different from the q-dependence of unknown interactions. But it is considered to be not the origin of the q-dependence of R(q), because the change of the effective density changes not the q-dependence but the overall strength.

This q-dependence of R(q) has not yet been understood and is to be solved in future study. Among the parameters listed in Table 4.6, intensity of incident neutron, form factor and particle size, and absorption cross section can induce the q-dependence. The neutron intensity is considered to be not the matter, because the experimentally measured intensity distribution was used in the simulation, and therefore its influence is canceled out in the ratio R(q). Form factor and particle size were determined from the experimental data of the SAXS measurement, in which the tension of the windows of the target holder were very much different from the one in the SANS measurement. And therefore it may not be taken into account properly and may result in incomplete correction for the aggregation effect. To improve that, it will be useful to make a SAXS measurement using the real

target used in the SANS experiment. A hint for the origin of the q-dependence can also be found from the comparison of the ratios obtained from the data in the wavelength regions of $\lambda_{\mathrm{FOL}} = 0.2 \sim 0.9\,\mathrm{nm}$ (Fig. 5.4, left) and $\lambda_{\mathrm{FOL}} = 0.9 \sim 1.14\,\mathrm{nm}$ (Fig. 5.4, right) shown in Fig. 4.40. As shown in those figures, the q-dependence found in Fig. 5.2 is due to the events with shorter wavelength. The wavelength distribution of transmitted neutrons shown in Fig. 4.33 also shows a discrepancy at shorter wavelengths, but the origin of this behavior is not clear at this time.

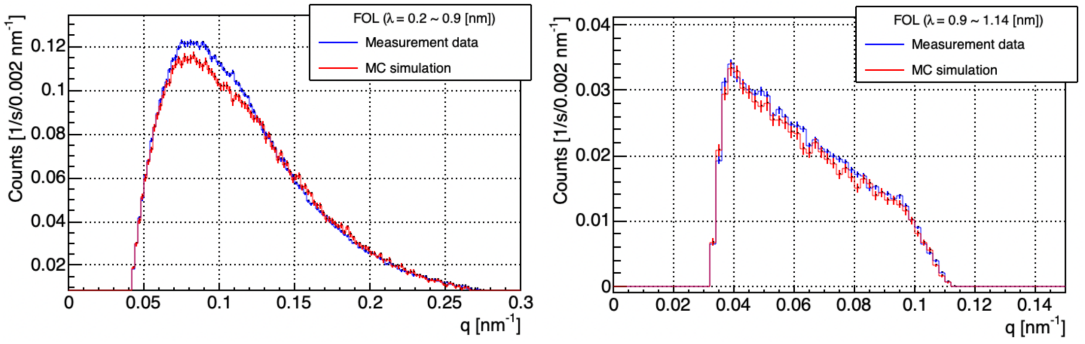

Figure 5.3: Comparison of the q distribution calculated each wavelength of data and simulation.(left) $\lambda_{\mathrm{FOL}} = 0.2 \sim 0.9\,\mathrm{nm}$, (right) $\lambda_{\mathrm{FOL}} = 0.9 \sim 1.14\,\mathrm{nm}$.

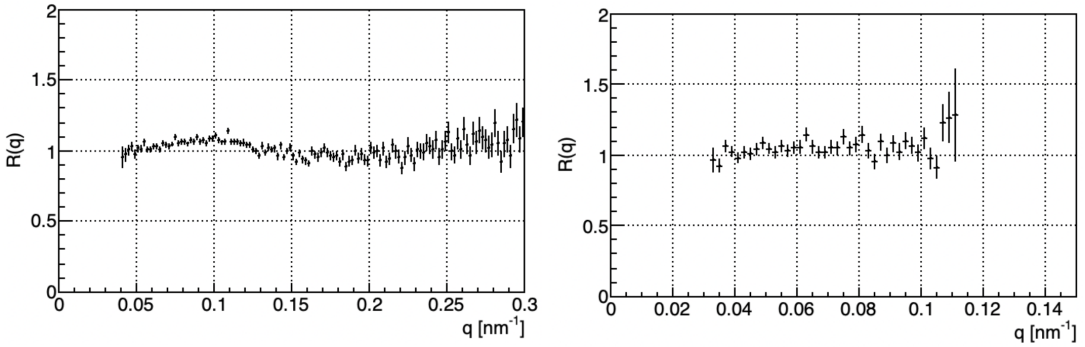

Figure 5.4: Comparison of the R(q) distribution using the each wavelength data. (left) $\lambda_{\mathrm{FOL}} = 0.2 \sim 0.9\,\mathrm{nm}$, (right) $\lambda_{\mathrm{FOL}} = 0.9 \sim 1.14\,\mathrm{nm}$.

5.1.3 Evaluation of 95% CL Including Systematic Errors

Among the parameters used in the simulation, the b_{coh}, neutron transmittance of V nanoparticles shown in Table 4.6, effective density of V nanoparticle in the SANS cell show in Fig. 4.31 and fluctuation of structure factor due to effective density error shown in Fig. 4.34 are taken into consideration. The b_{coh} of V nanoparticles: $0.719 \pm 0.023\,\mathrm{fm}$ is calculated based on the content of each element and the nuclear scattering length. The error of the published nuclear scattering length data list is determined from the systematic error in the paper. Next, as shown in Fig. 4.33, the neutron transmittance of V nanoparticles calculated from the effective density shows a deviation of $\sim 1\,\%$ which is larger than the statistical error in the range of $0.2 \sim 0.6\,\mathrm{nm}$. This difference means that in the present analysis the correction for the attenuation of the incident and scattered neutrons may be incorrect with $1\,\%$ level.

Calculation procedure

(1) Determine b_{coh} of each element using uniform random numbers within the systematic error of data.

(2) Determine the concentration of each element using normal distribution random numbers within the statistical error of data.

(3) Calculate the composite b_{coh} using the parameters selected in (1) and (2).

(4) determine the transmittance ratio value using uniform random > numbers with the mean value of 1.0 and the standard deviation of 0.01 which corresponds to the systematic error of the transmittance.

(5) The effective density was determined according to the Gaussian random number with the standard deviation of $9.3\,\%$, and the structure factor for the aggregation effect was determined using Eq. (4.27).

(6) Determine the absolute value of the calculated scattering intensity using the parameters selected in (3), (4) and (5).

(7) The ratio R(q) of the experimental intensity to the calculated one with including only the nuclear scattering was fitted with the fitting function containing the above determined parameters to obtain a chi-square distribution as a function of the multiplication factor P_α in Eq. (5.4). The fitting is performed in the range $q < 0.3\,\mathrm{nm}$, which is not used in the analysis of the effective density.

(8) Find P_α and σ that give the minimum chi-square value. Repeat the above steps (1) $\sim$ (8) for 100 million times.

(9) Produce the superposition of 100 million Gaussian distributions with 100 million sets of P_α and σ to obtain the probability distribution function of P_α as shown in Fig. 5.5.

(10) From the area of the probability distribution function of the normalized P_α obtained in (9), the P_α that gives a 95 % probability is the upper limit of the 95 % C.L. .

Figure 5.5 is a probability distribution created for each λ_B shown in Fig. 5.1.

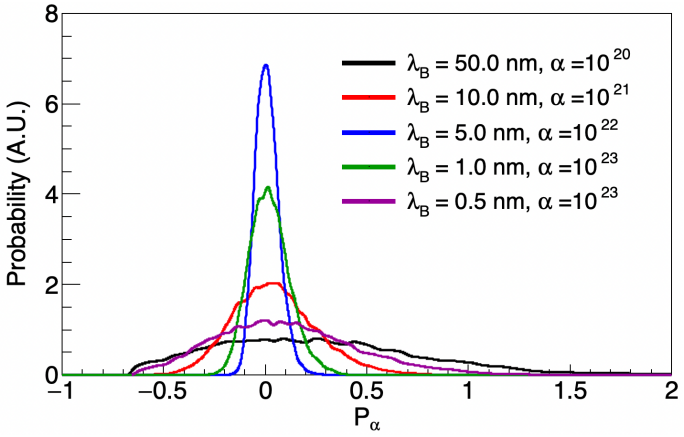

Figure 5.5: Upper limit of α with 95 % C.L. evaluated from the cumulative probability density of P_α. R(q) was evaluated using $\lambda_B = 50\,\mathrm{nm}$

From the area of each probability distribution of Fig. 5.5, we can estimate the upper limit of P_α at 95 % C.L.. This gives us a 95 % confidence interval that includes systematic error . When the cumulative probability is 0.5, P_α is the most probable value. And when it is 2.5 % and 97.5 %, it represents the lower and upper limits of the 95 % C.L. of P_α.

Figure 5.6 shows the results evaluated from the CDF (cumulative distribution function) when λ_B is changed. From Fig. 5.6, when $\lambda_B = 50\,\mathrm{nm}$ is evaluated at 95 % C.L., the upper limit is $P_\alpha = 0.1541$, so $\alpha = P_\alpha \times 10^{20} = 1.54 \times 10^{20}$.

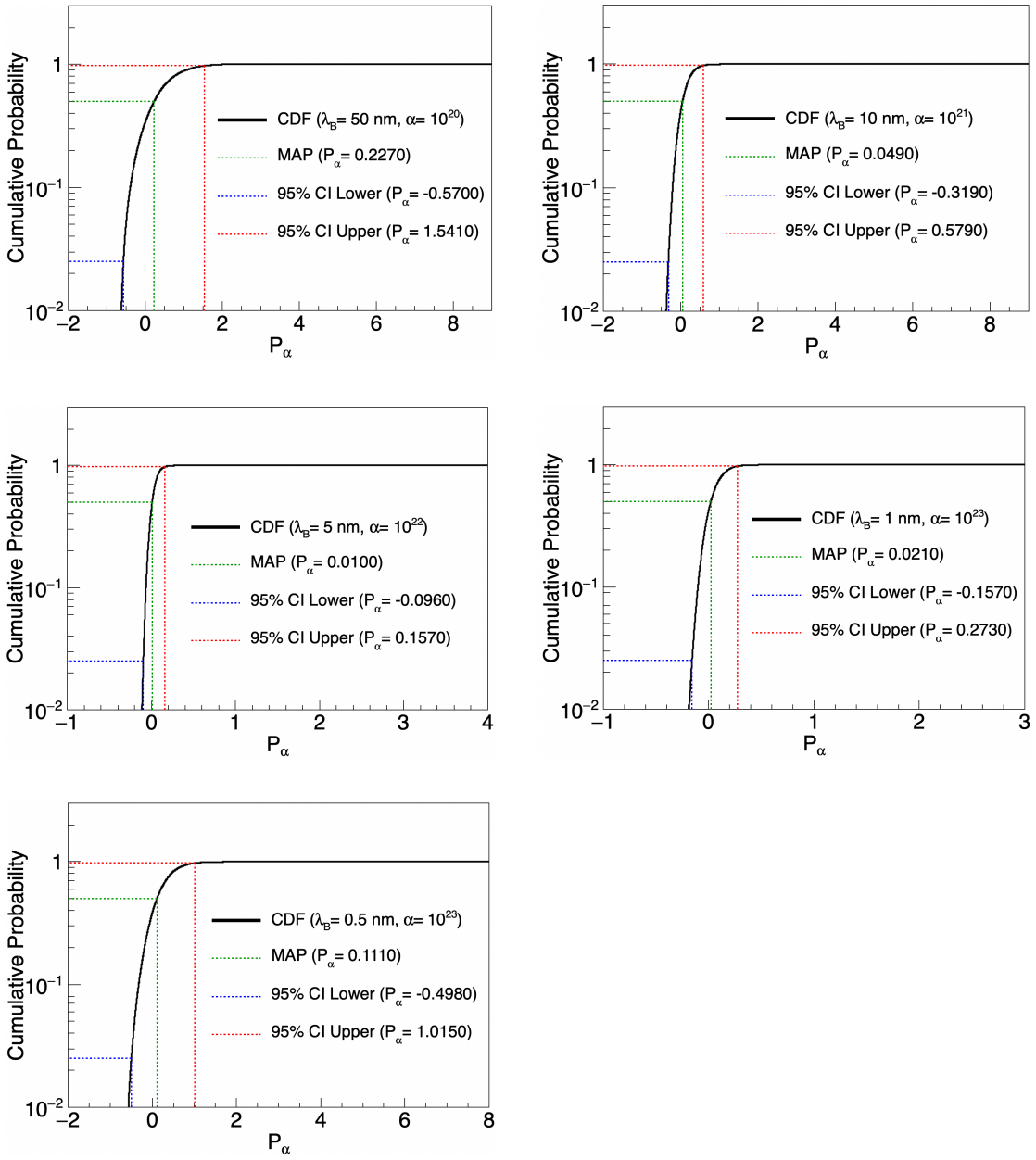

Figure 5.6: Upper limit of α with 95 % C.L. evaluated from the cumulative probability density of P_α. R(q) was evaluated using $\lambda_B = 0.5 \sim 50\,\mathrm{nm}$ in Fig. 5.1 (A) $\sim$ (E).

5.2 Discussion

5.2.1 Upper Limit on α

Figure 5.7 shows the $\lambda_B - \alpha$ two-dimensional plot obtained in Sec. 5.1.2 together with the existing results. As can be found in Fig. 5.7, the present result did not exceed the upper limit determined by Heacock et al.[23]. This is mainly due to low statistics of the MC simulation and a rather large statistical error in the effective target density (9.3 %).

The statistics of the MC will be improved by spending more CPU times. The effective target density will be more accurately determined if we make combined analysis including the effective target density and the correction factor for the aggregation effect in lower q region where much more statistics of the scattered neutron is available. With those additional analysis, the upper limit on α in this work is expected to be more improved in the near future. In addition, a SAXS measurement for the real sample with the same condition with the SANS experiment is scheduled to study and make a model-independent correction for the effect of the aggregation as mentioned bellow.

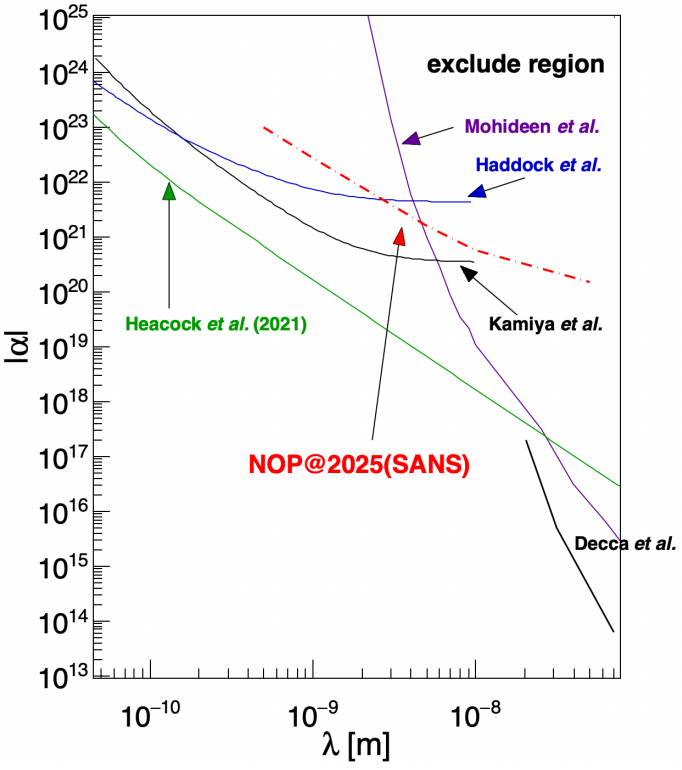

Figure 5.7: λ_B-α plot obtained from SANS experiments using V nanoparticles. (Red line) NOP@2025 (SANS) is the result of the present analysis for FOL data with a confidence level of 95 %.

The analysis result of Fig. 5.7 is the expected value obtained by assuming the aggregation model. Therefore, the result is preliminary.

5.2.2 Future Prospect

As discussed in Sec. 5.1.2, future prospects include investigation of the unexplained q-dependence of R(q). As discussed in Sec. 5.1.2, this q-dependence may be due to insufficient correction for the aggregation effect which was taken into account by assuming the most commonly used theoretical model which is not necessarily suitable for the present case. In stead of assuming a model, the effect can be directly studied by making the SAXS measurement of the real target used in the SANS measurement. Since the window of the SANS target is made of V-Ni alloy with total (upstream and downstream) thickness of 0.5 mm, a higher-energy X-ray beam or thinner window are required.

To penetrate the window material (0.5 mm thick V-Ni plate) used in SANS cells, a higher-energy X-ray beam is required. We anticipate that using an aluminum window approximately 0.1 mm thick would achieve approximately 80 % transmittance at the BL19B2 beamline at SPring-8, where an 18 keV X-ray beam is available, and we plan to submit a proposal for such measurements.

In addition, the V nanoparticles used as the target for SANS measurements have a positive value of the total coherent scattering length scattering length of 0.719 ± 0.023 fm due to residual oxygen (6.15 wt.%).

Since vanadium is known as the hydrogen-absorbing metal, by making absorption of hydrogen ($b_{coh} = -3.7390$ fm), it may be possible to compensate the effect of the oxygen contamination and reduce nuclear scattering.

Another possible method is to create alloy nanoparticles using Ti ($b_{coh} = -3.438$ fm) as a candidate for a prototype material using RF thermal plasma. Compared to vanadium, the coherent nuclear scattering length of Ti is about one order of magnitude more negative, so there is a margin for the contamination of oxygen. In addition, since Ti is one of the hydrogen storage metals, it may be possible to cancel the negative coherent nuclear scattering length of Ti by using deuterium ($b_{coh} = 6.671$ fm).

Chapter 6

Conclution and Summary

In this work, hypothetical gravity-like interaction was explored by means of the small-angle neutron scattering. Since the upper limit for the coupling constant of the interaction relative to the gravitational constant was many orders of magnitude worth than the predicted regions by some theoretical models, it was necessary to improve the experimental sensitivity. The limitation in the sensitivities of the previous experiments is partly due to the smallness of the weight of the target particle. To solve this problem, a target made of particle having the size similar to the range of unknown interaction to be explored, namely nanoparticles in the present case. By using nanoparticle as a target, the intensity of the scattering is enhanced thanks to the effect of the coherent scattering, with a factor of more than millions which corresponds to the number of atoms contained in a nanoparticle. Since the intensity background due to nuclear scattering is also enhanced with the same factor, it is necessary to suppress the nuclear coherent scattering. To meet the above requirements, nanoparticle samples made of very small coherent scattering length were developed. In fact, a nanopowder sample made of pure vanadium and V-Ni null-matrix alloy were successfully produced for the first time by means of the RF thermal plasma method. Unfortunately, the coherent scattering length was found to be not so close to zero due to the contamination of oxygen, but the developed vanadium sample is the nanopowder with the world-smallest coherent nuclear scattering cross section. Using this sample as the target, the small-angle neutron scattering (SANS) experiment was performed. Through the transmission measurement, the effective thickness of the target was found to be larger than the nominal value calculated from the measured weight of the sample material and the volume of the container, and it was confirmed with the independent measurement of the γ-ray transmission. Taking into account those experimental condition and through the comparison between the experimental q-dependence spectrum and the simulated one

calculated using the newly developed Monte Carlo code, a new upper limit on unknown interaction was obtained. The preliminary result on the upper limit of the unknown interaction in the region of $\lambda = 2 \sim 10\,\mathrm{nm}$ suggests the advantage of the present experimental method over our previous experiments which employed a single-atom target. As mentioned above, the sensitivity of the present experiment is limited by several factors such as the contamination of oxygen (6.15 wt.%), aggregation effect of nanopowder, and the ambiguity in the effective target density. The influence of the oxygen will be further improved by removing the oxygen in nanoparticles. In fact, my collaborator tested baking of the powder and found significant reduction of oxygen. Then it is interesting to develop baking as the method for removing oxygen. The effect of the aggregation was evaluated in the present work by employing a theoretical model commonly used in the analysis of the SANS measurement, but it will be possible to make a model-independent analysis by measuring the SAXS spectrum of the real sample cell. Since the real cell has thick windows, the available X-ray energy at the Aich-SR is not sufficiently high, but at the SPring-8, the available X-ray energy is 18 keV, which is sufficient to measure our sample. Having momentum-transfer data obtained for the real sample, the analysis can be made without introducing model for aggregation, and in principle systematic error should be reduced. The SAXS measurement at the SPring-8 will also provide the data of the transmission, which is useful to determine the effective target density with much better accuracy, leading to improve the limit for unknown interactions.

Appendix A

Theoretical Background

A.1 ADD model

In a new model based on the Kaluza-Klein theory published in 1998, it was pointed out that the size of the extra dimensions is larger than the plank scale considered in string theory and may extend to the millimeter range. This is called the "large extra dimension" model, and one of the most famous models is called the ADD model, named after the three authors who published the paper, N. Arkani Hamed, S. Dimopoulos, and G. Dvali [54, 32, 31]. The idea of extra dimensions is as follows. Newton's law and the Coulomb force observed in three-dimensional space both have distance dependence $F \propto 1/r^2$. These ISLs are derived as spherically symmetric solutions of Laplace's equation. As an example, consider Gauss's law for a point charge,

$$\Phi = \oint \vec{E} \cdot d\vec{A} = \frac{Q_{\text{enc}}}{\epsilon_0} \tag{A.1}$$

with, Φ is an electric flux, $\vec{E}$ is an electric field, $d\vec{A}$ is the differential area element with the surface normal to a Gaussian surface of area A and Q_{exc} denotes the amount of charge trapped within the surface. If we further generalize Gauss's law to n-spatial dimensions,

$$\oint \cdot d\vec{A} = A_n \propto r^{n-1} \tag{A.2}$$

where, the electric field is isotropic and we have assumed an n-dimensional sphere for the Gaussian surface. For three-dimensional space, Eqs. (A.1) and (A.2) lead to the inverse

square law known as Coulomb's law. The idea of assuming such an extra dimension originates from the Kaluza-Klein theory. In 1921; Theodor Kaluza pointed out that if general relativity theory is extended to five-dimensional space-time, the equations can be separated into the usual four-dimensional space-time and the extra dimension [55]. This dimension is equivalent to adding an extra scalar field known as the dilaton to Maxwell's equations for the electromagnetic field. In this framework, it was shown that gravity and electromagnetism can be unified by adding one extra dimension. Also in 1926, Oskar Klein proposed to add to Kaluza's assumption that the dimensions of the extra space are rounded into a circle with a radius of about the Planck length [56].

One interesting prediction made in the ADD model is that the fundamental scale at which gravity is thought to be comparable in strength to the gauge interaction is assumed to be the electroweak scale ($m_{ew} \approx 1\,\mathrm{TeV}$) rather than the Planck scale ($m_{\mathrm{pl}} \approx 10^{16}\,\mathrm{TeV}$). This proposal has attracted attention because it shows the possibility of resolving the large disparity between the energy scales of the electroweak symmetry breaking the Planck energy. In SM, the fields must be localized in a four-dimensional manifold called a brane, and only gravitons can travel through the (4+n)-dimensional bulk. Since m_{ew} is assumed to be the only short-distance scale in theory, our brane should have a "thickness"m_{ew}^{-1} in the extra n-dimension. The potential of normal gravity acting on an n-dimensional space compactified to a radius R is shown below. If the distance between two objects is r, the gravitational potential between masses m_1 and m_2 of matter placed in the region of $(r \ll R)$ is given as

$$V(r) = -\frac{m_1 m_2}{M_{pl(4+n)}^{n+2}} \frac{1}{r^{n+1}}, \qquad (r \ll R) \tag{A.3}$$

here, $\hbar = c = 1$, $M_{pl(n+4)}$ is plank scale of $(4+n)$ dimension. For masses placed a $(r \gg R)$ part, their gravitational flux lines do not penetrate the extra dimensions. From the Gauss's law, one obtains

$$V(r) = -\frac{m_1 m_2}{M_{\mathrm{pl(4+n)}}^{n+2} R^n} \frac{1}{r}, \qquad (r \gg R) \tag{A.4}$$

The relationship between the fundamental unified scale $M_{\mathrm{pl(n+4)}}$ in Eq. (A.4) and M_{pl} in our four-dimensional world is

$$M_{pl}^2 = M_{(n+4)}^2 R^n. \tag{A.5}$$

If we set the condition that the fundamental scale $M_{\mathrm{pl}} \approx m_{\mathrm{ew}}$ assumed in the ADD model and require that R reproduces the observed Planck mass, we get

$$R\,[\mathrm{cm}] \approx 10^{\frac{30}{n}-17} \times \left(\frac{1\,\mathrm{TeV}}{m_{\mathrm{ew}}}\right)^2 \tag{A.6}$$

Assuming $m_{\mathrm{ew}} \approx 1\,\mathrm{TeV}$, this can account for the hierarchy problem and explain the predicted size of the extra dimension. The case of $n = 1$ implies a deviation from Newtonian gravity over the distance of the solar system ($R = 10^{13}\,\mathrm{m}$), but this has already been excluded by previous observations. For $n \geq 2$, experimental searches for violation of ISL at short distances where ($R \leq 100\,\mu\mathrm{m}$) are still ongoing.

Appendix B

Theory of Low Energy Neutron Scattering

This section provides an overview of the theory of neutron scattering. First, in Sec. B.1.1, scattering kinematics for small-angle neutron scattering experiments are explained. In Sec. B.1.2, an expression for the scattering amplitude is shown from a general quantum mechanical perspective using the Born approximation of the scattering potential. In Sec. B.1.3, the general form of the differential cross section for low-energy neutron scattering is shown, and it is explained that the scattering amplitude can be obtained as a quantity called the scattering length. In Sec. B.1.4, the scattering system in a multi-particle system is explained, and the cross sections called coherent scattering and incoherent scattering caused by the structure of the scatterer are explained.

B.1 Differential Cross Seciton

B.1.1 Scattering Kinematics

For an explanation of scattering theory, we follow references [57] and [58]. Small angle scattering (SAS) is a method for measuring scattering phenomena in the scattering angle range of $\theta < 5°$. In the measurement, a scattering device is constructed with slits to narrow the beam and form a parallel beam to distinguish small-angle scattering events from the incident beam. Here, a general scattering event is described in Fig. B.1.

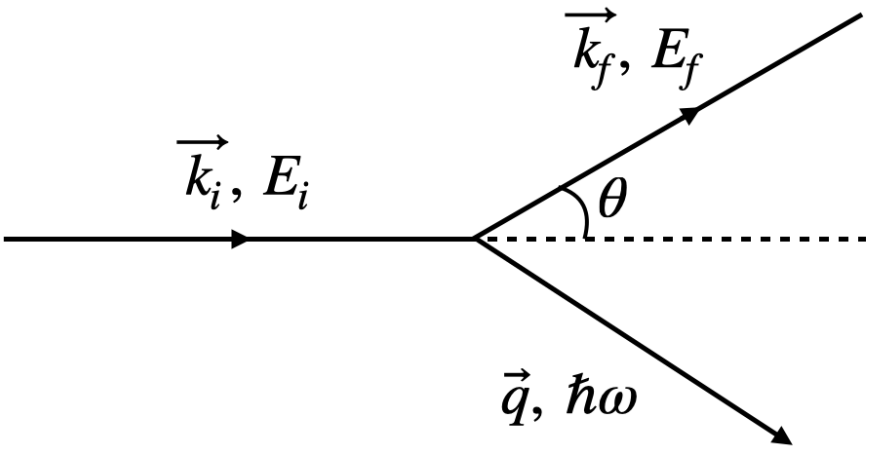

Figure B.1: Representation of a scattering event.

Consider the process in which a particle with incident wave vector $\vec{k_i}$ and energy E_i is scattered with an angle θ by the interaction potential V, and becomes a final state with wave vector $\vec{k_f}$ and energy E_f. In this case, the initial state and the final state of the sample are A and A', respectively. Considering the law of conservation of energy before and after scattering, the energy transfer of the particle $\hbar\omega = E_f - E_i = \hbar^2(|\vec{k_f}|^2 - |\vec{k_i}|^2)/2m$ and the energy of the sample are related by the following equation.

$$\hbar\omega = E_{\mathrm{A}'} - E_{\mathrm{A}} \tag{B.1}$$

Here, $\vec{q}$ (momentum transfer) represents the difference in the wave vectors of the particle before and after scattering.

$$-\vec{q} = \vec{k_f} - \vec{k_i} \tag{B.2}$$

The scattering process is elastic when $E_i = E_f$ (the neutron energy does not change) and inelastic when $E_i \neq E_f$. In the case of elastic scattering, from the cosine law for the scattering vector and Eq. (B.2)

$$q^2 = |\vec{k_f} - \vec{k_i}|^2 = k_i^2 - k_f^2 - 2k_i k_f cos(\theta) \tag{B.3}$$

Where q is defined as follows based on the relationship of $k_i = k_f = k$.

$$q = 2k\sin(\theta/2) = \frac{4\pi}{\lambda}\sin(\theta/2) \tag{B.4}$$

Where λ represents the wavelength of the incident particle. When the incident particle is a neutron, the wavelength is defined by the de Broglie's relation $\lambda = \frac{h}{m_{\mathrm{n}}v}$ using the neutron's mass m_n and velocity v. The neutron velocity v can be expressed as $v = (\frac{3k_{\mathrm{B}}T}{m})^2$ using the temperature T of the neutron source (such as a nuclear reactor) and the Boltzmann constant k_B. From these relationships, the kinetic energy can be expressed in terms of wavelength and temperature as follows:

$$E = \frac{1}{2}m_{\mathrm{n}}v^2 = \frac{3}{2}k_{\mathrm{B}}T \tag{B.5}$$

$$E = 0.08617T = 5.227v^2 = 81.81\frac{1}{\lambda^2} = 2.072k^2 \tag{B.6}$$

Table B.1: Approximate values for neutron energy, temperature, and wavelength ranges [9].

Source	Energy [meV]	Temperature [K]	Wavelength [Å]
Cold-neutron	0.1 - 10	1-120	30-3
Thermal-neutron	5 - 100	60-1000	4-1
Hot-neutron	100 - 500	1000-6000	1-0.4

In addition, the types of the neutron beams are classified as shown in Table B.1 based on the relationship between the corresponding energy and temperature. When the incident particle is a low-energy neutron such as a thermal neutron as shown in Table B.1, the elastic scattering phenomenon occurs without changing the internal energy of the nucleus. In the case of low energy neutrons, since those wavelengths are much larger (10^{-14} [m] to 10^{-15} [m] in case of thermal neutrons) than the range of nuclear forces from atomic nuclei, scattering is dominated by the s-wave scattering which shows spherically symmetric angular distribution. Therefore, it results in an isotropic distribution of the scattered wave. In that case, the wave function of a neutron scattered at point r can be written in the form:

$$\phi_{\mathrm{sca}} = -\frac{b}{r}\exp(ikr) \tag{B.7}$$

where b is an angle-independent constant called the scattering length. In the next Sec. B.1.2, we explain how to write the scattering length and differential cross section in terms of the wave nature of the neutron.

B.1.2 Wave Functions of Scattering States and Scattering Amplitudes

Next, we explain the scattering amplitude to describe the scattering cross section quantum mechanically. As shown in Fig. B.1, we consider the scattering phenomenon when a neutron with kinetic energy E and wave number k enters from the negative direction of the z axis and is scattered at the origin by the nuclear potential $V(\boldsymbol{r})$. The scattering state is treated as a stationary state. In this case, the Hamiltonian of the entire system is $H = H_0 + V(r)$, and the Hamiltonian of the free particle is $H_0 = -\frac{\hbar^2}{2m}\Delta$. The Schrödinger equation for the entire system is

$$\left[-\frac{\hbar^2}{2m}\Delta + V(\boldsymbol{r})\right]\psi(\boldsymbol{r}) = E\psi(\boldsymbol{r}) \tag{B.8}$$

For Eq. (B.8) to satisfy the boundary condition ($r \to \infty$, $V(\boldsymbol{r}) = 0$), $\psi(\boldsymbol{r})$ is as follows.

$$\psi(\boldsymbol{r}) = \exp(ikz) + f(\theta)\frac{\exp(ikr)}{r} \tag{B.9}$$

, where the first term in Eq. (B.9) is the plane wave of the incident wave obtained from the free particle equation $H_0\phi_{in} = E\phi_{in}$. The second term represents the spherical wave of the scattered wave, and $f(\theta)$ represents the scattering amplitude. To calculate the scattering amplitude, we express Eq. (B.9) using the Green's function $G(\boldsymbol{r})$ as

$$(\Delta + k^2)\psi(\boldsymbol{r}) = U(r)\psi(\boldsymbol{r}) \tag{B.10}$$

$$(\Delta + k^2)G(\boldsymbol{r}) = \delta(\boldsymbol{r}) \tag{B.11}$$

In the Eq. (B.10), using the reduced mass μ and $V(\boldsymbol{r}) = V(r)$, we set $k^2 = \frac{2\mu E}{\hbar^2}$ and $U(r) = \frac{2\mu V(r)}{\hbar^2}$. Furthermore, in order to satisfy the boundary condition Eq. (B.9), this reduces to solving the following equation:

$$\psi(\boldsymbol{r}) = \exp(ikz) + \int d^3r' G(\boldsymbol{r} - \boldsymbol{r'})U(r')\psi(\boldsymbol{r}) \tag{B.12}$$

The solution of Green function is given by,

$$G_{\pm}(\boldsymbol{r}) = -\frac{1}{4\pi}\frac{\exp(\pm ikr)}{r} \tag{B.13}$$

In Eq. (B.13), $G_{+}(\boldsymbol{r})$ and $G_{-}(\boldsymbol{r})$ represent outward and inward spherical waves, as shown in Fig. B.2.

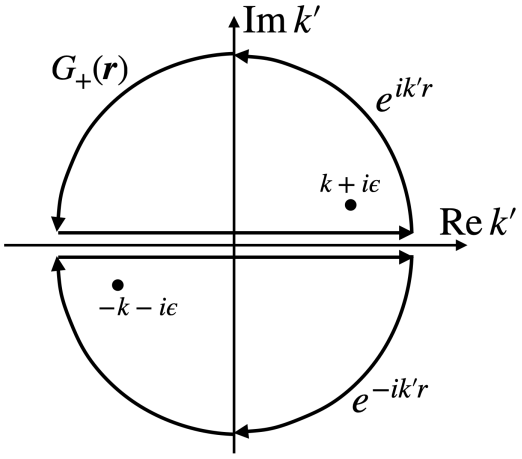

Figure B.2: The integral path of Eq. (B.12). It can be found by the residue theorem.

Now, expressing Eq. (B.12) as an integral equation using Eq. (B.13),

$$\psi_{\pm}(\boldsymbol{r}) = \phi(\boldsymbol{r}) + \lim_{\epsilon\to+0}\frac{1}{E - H_0 \pm \epsilon}V(r)\psi_{\pm}(\boldsymbol{r}) \tag{B.14}$$

This is known as the Lippmann-Schwinger equation in the quantum scattering theory. In Eq. (B.14), the relationship $\langle \boldsymbol{r}|\frac{1}{E-\hat{H}_0\pm\epsilon}|\boldsymbol{r'}\rangle = \frac{2\mu}{\hbar^2}G_{\pm}(\boldsymbol{r}-\boldsymbol{r'})$ was used. where $\phi(\boldsymbol{r})$ is $\exp(ikz)$. To satisfy the asymptotic form Eq. (B.8), an outward spherical wave is chosen. When the potential $V(\boldsymbol{r})$ is sufficiently small, the scattering amplitude of Eq. (B.14) can be expressed as follows using the Born approximation.

$$f(\theta) \simeq -\frac{m}{2\pi\hbar^2}\langle\phi_{k'}|V(r)|\phi_k\rangle \tag{B.15}$$

B.1.3 General Expression for Differential Cross Section

Next, we derive the relationship between the scattering amplitude and the differential cross section. The basic derivation for describing low-energy neutron scattering follows

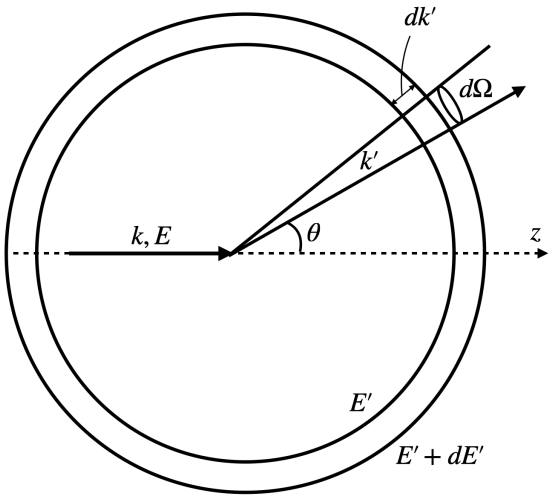

Figure B.3: Neutron and nucleus scattering system.

that given in the literature [57]. In this discussion, we ignore the neutron spin and let the neutron state be determined only by the wave vector. Also, N is the number of nuclei in the scattering body, R_j is the position vector of the i_{th} nucleus, and r is the position vector of the neutron. First, we consider the differential cross section $d\sigma/d\Omega dE$, which represents the sum of all processes in which the state of the scattering system changes from A to A' due to the nuclear potential $V(r)$ and the state of the neutron changes from k to k', as shown in Fig. B.3. Then, by the definition of the $d\sigma/d\Omega$,

$$\frac{d\sigma}{d\Omega dE'} = (\mathrm{n_s})/\Phi\, d\Omega \tag{B.16}$$

$$\left(\frac{d\sigma}{d\Omega dE'}\right)_{k,\, A\to k',\, A'} = \frac{1}{\Phi}\frac{1}{d\Omega}\sum_{k'} W_{k,A\to k',A'} \tag{B.17}$$

, where n_s denotes the number of neutrons per unit time into a solid angle $d\Omega$ in the direction θ, ϕ and into the energy width between E_0 and $E_0 + dE_0$. In Eq. (B.16), $W_{k,A\to k',A'}$ is the number of transitions per second from state k, A to state k', A' and Φ is the flux of incident neutrons. And the transition probability $W_{k,A\to k',A'}$ is calculated with the Fermi's golden rule.

$$\sum_{k'} W_{k,A\to k',A'} = \frac{2\pi}{\hbar}\rho_{k'}|\langle k'A'|V|kA\rangle|^2\delta(E_A - E_{A'} + E - E') \tag{B.18}$$

, where $\rho_{k'}$ is the number of momentum state in $d\Omega$ per unit energy range for neutrons in the state k'. The matrix element is given explicitly by

$$\langle k'A'|V|kA\rangle = \int \psi^*_{k'}\phi^*_{A'} V \psi_k \phi_A dR \tag{B.19}$$

$$dR = dR_1 dR_2 \ldots dR_N \tag{B.20}$$

In Eq. (B.20) dR_j is an element of volume for the jth nucleus , and dr is an element of volume for neutron. The integral is taken over all space for each of the $N+1$ variables. Then, Φ and $\rho_{k'}$ are considered as the real space density and k-space density of states of neutrons, respectively, which can be written as follows.

$$\Phi = \frac{1}{L^3}\frac{\hbar k}{m} \quad (\text{Real space density} \times \text{Neutron velocity}) \tag{B.21}$$

$$\rho_{k'} = \left(\frac{L}{2\pi}\right)^3 dk' = \left(\frac{L}{2\pi}\right)^3 \frac{mk'}{\hbar^2} d\Omega dE' \tag{B.22}$$

From Eq. (B.18) and (B.19), the differential cross section is obtained as

$$\frac{d\sigma}{d\Omega} = \int_0^\infty \left(\frac{d^2\sigma}{d\Omega dE'} dE'\right) = \frac{k'}{k}\left(\frac{m}{2\pi\hbar^2}\right)^2 |\langle k'A'|V|kA\rangle|^2 \tag{B.23}$$

$$\int \delta(E_A - E_{A'} + E - E')dE' = 1 \tag{B.24}$$

The potential of the entire scattering system is obtained by integrating the potential of each j-th nucleus with respect to r. Here, the potential of all nuclei is given as

$$V = \sum_j V_j(r - R_j) \tag{B.25}$$

$$x_j = r - R_j \tag{B.26}$$

And then,

$$\begin{aligned}\langle k'A'|V|kA\rangle &= \sum_j \int \phi^*_{A'} \exp(-ik'(x_j + R_j)) V_j(x_j) \phi_A \exp(ik(x_j + R_j)) dR dx_j \\ &= \sum_j V_j(k - k') \langle A'| \exp(i(k - k')R_j)|A\rangle\end{aligned} \tag{B.27}$$

, where $V_j(k-k') = \int V_j(x_j)\exp(i(k-k')x_j)dx_j$ and $\langle A'|\exp(i(k-k')R_j)|A\rangle = \int \phi^* \exp(i(k-k')R_j)\phi_A dR$. When the nucleus is fixed at the origin, $R_j = R = 0$ and $A = A'$ and thus

$$\begin{aligned}\langle k'A'|V|kA\rangle &= \int \phi_A^*\phi_A dR \int V(r)\exp(iqr)dr \\ &= \int V(r)\exp(iqr)dr\end{aligned} \tag{B.28}$$

In this expression, as seen in Eq. (B.2), the elastic scattering condition for low-energy neutrons is $k = k'$, so $q = k - k'$. Therefore, the differential cross section of a single nucleus fixed at the origin can be expressed using Eqs. (B.28) and (B.23):

$$\frac{d\sigma}{d\Omega} = \left(\frac{m}{2\pi\hbar^2}\right)^2 \left|\int V(r)\exp(iqr)dr\right|^2 \tag{B.29}$$

As explained in the previous Sec. B.1.1, the nucleus is much smaller than the de Broglie wavelength of a thermal neutron, so the potential $V(r)$ is short-range. Therefore, the interaction between neutrons and atomic nuclei can be explained under the Born approximation by using a three-dimensional Dirac function $\delta(r)$.

$$V(r) = a\delta(r) \tag{B.30}$$

$$\int_{\text{all space}} \delta(r)dr = 1 \tag{B.31}$$

where a is a real constant. Substituting Eq. (B.30) into Eq. (B.29),

$$\frac{d\sigma}{d\Omega} = \left(\frac{m}{2\pi\hbar^2}\right)^2 \left|\int a\delta(r)\exp(iqr)dr\right|^2 = \left(\frac{m}{2\pi\hbar^2}\right)^2 a^2 \tag{B.32}$$

where, the scattering amplitude in the second term of Eq. (B.9) can be approximated as the scattering length b in the case of low-energy neutron scattering such as cold neutrons, resulting in the following relationship.

$$\frac{d\sigma}{d\Omega} = b^2 \tag{B.33}$$

From Eq. (B.32),

$$a = \left(\frac{2\pi\hbar^2}{m}\right) b \tag{B.34}$$

Inserting this value in Eq. (B.30) one obtains

$$V(r) = \frac{2\pi\hbar^2}{m} b\delta(r) \tag{B.35}$$

This potential is known as the "Fermi's pseudopotential". The positive sign in Eq. (B.35) comes from the definition of b in Eq. (B.7) and means that the scattering length of the repulsive potential is positive. All derivations of the cross sections are based on Fermi's golden rule, which is equivalent to the Born approximation for the scattering process. Equation (B.35) shows that a repulsive pseudopotential gives a positive scattering length and an attractive pseudopotential gives a negative scattering length. However, a positive scattering length does not necessarily mean that the actual potential is repulsive; the actual potential is essentially attractive. The details of the shape, depth, and range determine the magnitude and sign of the scattering length. The scattering length defined in Eq. (B.7) is related to a fixed nucleus and is sometimes called the bound scattering length. Also, the imaginary term when expressed as a complex number represents absorption ($\sigma_{abs} = -\frac{4\pi}{k}\mathrm{Im}\, b$).

B.1.4 Coherent and Incoherent Scattering

In the previous Sec. B.1.3, the scattering cross section of a single nucleus was discussed. In this section, we consider scattering systems consisting of many atoms. The value of the scattering length b varies from nucleus to nucleus, depending on the nuclear spin and the presence of isotopes. For a large number of nuclei, the scattering from each nucleus is effectively indistinguishable, because the wavelength of low-energy neutron is much longer than the radii and the separations of nuclei. We expect the scattering to occur randomly within the sample, essentially averaging out the isotopic composition of the sample. In other words, there is no correlation between the position of an atom and the isotope or nuclear spin state at that position. If a real sample is composed of several elements with the total number of atoms N, the total scattering potential $V(r)$ is given as

$$V(r) = \frac{2\pi\hbar^2}{m} \sum_i^N b_i \delta(r - R_i) \tag{B.36}$$

In this case, the differential cross section from the potential of the entire scattering system is given by the following Eq. (B.29) :

$$\frac{d\sigma}{d\Omega} \approx \sum_{i,j} \overline{b_i b_j} \exp\{iq(r_i - r_j)\} \tag{B.37}$$

where b_i and b_j are the scattering lengths of the atoms at positions r_i and r_j. The bars indicate the average of the natural isotopic abundance ratio. Since there is no correlation between sites, the average of the "self" $(i = j)$ and "cross" $(i \neq j)$ terms in the sum can be expressed as

$$\overline{b_i b_j} = \begin{cases} \overline{b_i^2} & (\mathrm{i} = \mathrm{j}) \\ \overline{b}_i\, \overline{b}_j & (\mathrm{i} \neq \mathrm{j}) \end{cases} \tag{B.38}$$

where the mean scattering length and the mean squared scattering length are obtained from the abundance ratio f of each isotope. If m types of isotopes are contained,

$$\begin{aligned} \overline{b_i} = \overline{b} &= \sum_i^m f_i \overline{b_i} \\ \overline{b_i^2} = \overline{b^2} &= \sum_i^m f_i \overline{b_i^2} \end{aligned} \tag{B.39}$$

where f_i is the abundance ratio which is equal to the ratio of the number N_i of nuclei i to the total number N of nuclei.

$$f_i = \frac{N_i}{N} \quad (N = \sum_i^m N_i \text{ and, therefore } \sum_i^m f_i = 1) \tag{B.40}$$

From the relationship of Eq. (B.18), Equation (B.37) is separated into two components of "self" and "cross" term.

$$\begin{aligned} \frac{d\sigma}{d\Omega} &= \sum_{i \neq j} \overline{b_i b_j} \exp\{iq(r_i - r_j)\} + \sum_i \overline{b_i^2} \\ &= \sum_{ij} \overline{b}_i\, \overline{b}_j \exp\{iq(r_i - r_j)\} + \sum_i (\overline{b_i^2} - \overline{b_i}^2) \end{aligned} \tag{B.41}$$

By dividing the cross section by the method of Eq. (B.41), we can define scattered waves in which neutron wave interference occurs due to the regularity of the positions of isotope nuclei due to the structure of a sample composed of many atoms, and random scattering in which no wave interference occurs due to differences in the spin states of the nuclei or isotopes. Substiuting Eq. (B.41) into Eq. (B.39) leads to

$$\frac{d\sigma}{d\Omega} = \left\{ \overline{b^2} \left| \sum_i^N \exp(iq \cdot r_i) \right|^2 + \frac{1}{2} \sum_{j \neq k} f_i f_j (\overline{b_i} - \overline{b_j})^2 + \sum_j^m f_i \left(\overline{b_j^2} - (\overline{b_j})^2 \right) \right\} \tag{B.42}$$

Where $\overline{\mathrm{b_i}} = \overline{\mathrm{b}} = \sum_j^m f_j \overline{b_j}$ and $\overline{\mathrm{b_i^2}} = \overline{\mathrm{b^2}} = \sum_j^m f_j \overline{b_j^2}$. The first term in Eq. (B.42) is defined as the coherent scattering, and the third term as the incoherent scattering. The coherent scattering in the first term contains information about the structure of the sample, and depends on the correlation between the positions of the same atomic nuclei at different times and the correlation between the positions of different atomic nuclei at different times. In other words, it is a term that depends on momentum transfer. Also, since the position of each atomic nucleus cannot be identified from the perspective of the incident neutron, it is defined by the average potential from the scattering length of the elements contained in the sample. On the other hand, the incoherent scattering in the third term does not contain information about the sample structure, regardless of the position correlation of the atoms. This arises from the deviation from the average value when the scattering length differs due to differences in the nuclear spin state of the atomic nuclei or the presence of isotopes. Incoherent scattering does not have an interference effect because it depends only on the correlation between the positions of the atomic nuclei at different times. In other words, the scattering becomes random and does not depend on the momentum transfer. The second term in Eq. (B.42) appears when multiple elements are randomly distributed, and is called diffuse coherent scattering. This term does not depend on momentum transfer and provides information about the structure of the scattering system, i.e., that the atoms are disordered [59].

B.1.5 Scattering amplitude of Unknown interaction

We consider the case where there is a potential of unknown short-range forces such as Eq. (1.2). First, the scattering amplitude of the unknown short-range forces for the case that a single low-energy neutron is scattered by a single atomic nucleus can be expressed as follows from Eq. (B.28).

$$
\begin{aligned}
b_{\mathrm{Y}}(q) &= \frac{m}{2\pi\hbar^2}\int V_5(r)\exp(-i\vec{q}\cdot\vec{r})\boldsymbol{dr} \\
&= \frac{m}{2\pi\hbar^2}\int G\frac{\alpha Mm}{r}\exp(-r/\lambda_B)\exp(i\vec{q}\cdot\vec{r})\boldsymbol{dr} \\
&= \frac{m}{2\pi\hbar^2}\int_0^\infty G\frac{\alpha Mm}{r}\exp(-r/\lambda_B)\exp(i\vec{q}\cdot\vec{r})r^2dr\int_0^\theta\sin\theta d\theta\int_0^{2\pi}d\phi \\
&= \alpha\frac{GMm^2}{2\pi\hbar^2}\int_0^\infty\exp(-r/\lambda_B)\exp(iqr\cos\theta)rdr\int_{-1}^1 d(\cos\theta)\int_0^{2\pi}d\phi \\
&= \alpha\frac{GMm^2}{iq\hbar^2}\int_0^\infty\exp(-r/\lambda_B)\Big[\exp(iqr)-\exp(-iqr)\Big]dr \\
&= \alpha\frac{GMm^2}{iq\hbar^2}\int_0^\infty\exp\left\{-\left(\frac{1}{\lambda_B}-iq\right)r\right\}-\exp\left\{-\left(\frac{1}{\lambda_B}+iq\right)r\right\}dr \\
&= -\alpha\frac{GMm^2}{iq\hbar^2}\left(\frac{1}{1/\lambda_B-iq}-\frac{1}{1/\lambda_B+iq}\right) \\
&= -\alpha\frac{GMm^2}{iq\hbar^2}\left(\frac{2iq}{1/\lambda_B^2+q^2}\right) \\
&= -\alpha\left(\frac{2GMm^2}{\hbar^2}\right)\frac{1}{\lambda_B^{-2}+q^2}
\end{aligned}
\tag{B.43}
$$

Appendix C

Elemental Analysis Methods

C.1 SEM-EDS

The nanopowder were observed and analyzed using the SEM (JSM-F100) of the Institute of Scientific and Industrial Research in Osaka university. The resolution of the JSM-F100 is from 0.9 nm(1 kV) to 1.3 nm(20 kV), the incident voltage is from 0.01 to 30 kV, and the photo magnification is from 10× to 1,000,000×. The electron gun is an in-lens Schottky Plus field emission gun (FEG). The detector is set up with an upper SE detector (UED) above the objective lens and a lower SE detector (SED) below it for observing the reflected electrons from the sample. The UED detects high-angle reflected electrons, and mainly obtains composition information (internal information) of the observed sample. The SED detects low-angle reflected electrons, and obtains information on the unevenness of the observed sample surface. In addition, an SDD (silicon drift detector) is installed for EDS analysis using the characteristic X-rays of the observed sample. The energy resolution of EDS is 135 eV, the detection limit is from 0.1 to 0.2 wt%, and the detectable elements are from B to U. The principle of composition analysis using characteristic X-rays is as follows. When the electrons emitted from the electron gun make inelastic scattering with the specimen, some orbitals become vacant because of ionization and/or excitation, and the vacant orbitals are filled with electrons from other orbits, emitting X-rays whose energies correspond to the energy differences between the states responsible for those transitions. Since each element has unique values of those X-ray energies, the X-rays are called characteristic X-rays. There are several types of characteristic X-rays depending on the difference in orbital energy when an electron transitions, but the X-rays (Kα rays) that are generated when transition from the L shell to the K shell have the highest energy. In the present

case, the energy region of interest is around the energy of the vanadium K_α (4.949 keV), Since the EDS analysis is performed by detecting K_α X-rays, , the terminal voltage was set to 10 kV. This is because it is considered effective to select a ratio of incident electron energy to critical excitation energy of 2 to 3 times in order to efficiently cover the energies of the characteristic X-rays of the elements to be analyzed.

The EDS analysis is a kind of a semi-quantitative analysis, since in which the characteristic X-ray spectrum is corrected for atomic number effects, absorption effects, and fluorescence excitation effects based on the data of a standard sample using the ZAF correction method (corrections for effects of atomic number dependence, absorption, and fluorescence).

As shown in left of Fig. C.1, the observation was performed by attaching the sample powder to Nissin EM's conductive carbon double-sided tape using a toothpick immediately after opening the plastic bag. For EDS analysis, the powder is placed on Au foil as shown in right of Fig. C.1, and measurements are performed so that elements (O and C) derived from the carbon tape are not detected. The conductive carbon double-sided tape uses an acrylic adhesive containing carbon powder as a conductive filler on the surface of the nonwoven fabric base material. For this reason, carbon and oxygen may be detected from Carbon tape too. After the observation sample is attached to the SEM and evacuated to about 10^{-3} Pa by the TMP.

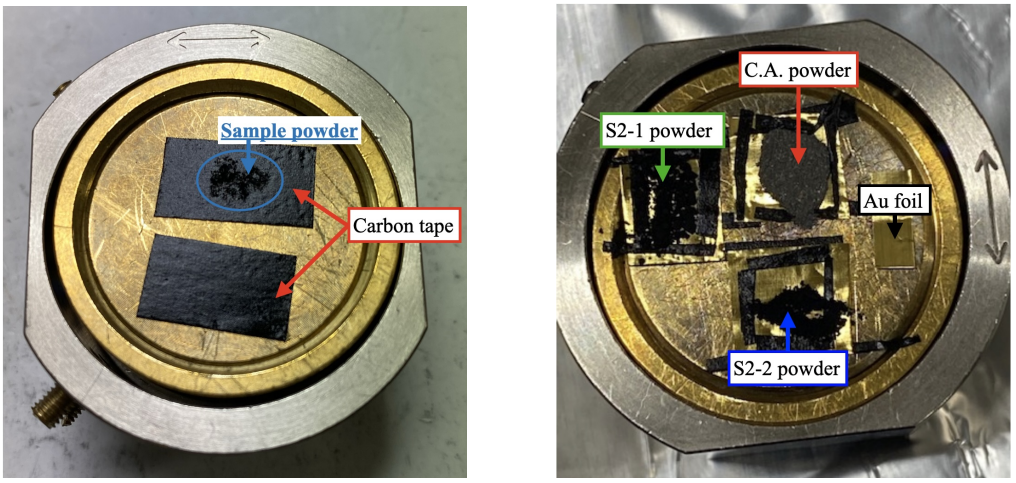

Figure C.1: Fixing powder samples for SEM observation :(left) For particle size observation and EDS analysis, (right) For O and C analysis by EDS.

C.2 ICP-AES

The metal element analysis of the sample powder was asked to the Institute of Scientific and Industrial Research, Osaka University, and was carried out using an inductively coupled plasma atomic emission spectrometer (ICP-AES [ICPS-8100]). The detection principle of ICP-AES is to atomize the sample solution and introduce it into Ar plasma, and spectroscopically analyze the light emitted when the excited elements return to the ground state, and to qualitatively determine the elements from the wavelength and quantitatively determine the elements from the intensity. Regarding the wavelength composition, ICPS-8100 calibrates the wavelength using elements such as C, N, O, and Ar contained in water and plasma. For quantitative analysis, a calibration curve is created using an element standard solution with a known concentration, and quantification is performed using the calibration curve method. ICP-AES is a method that mainly analyzes metals, and cannot measure light elements such as moisture and organic matter attached to the sample surface, oxygen in oxidized metals, and carbon. This is because the sample gasifies and volatilizes during the acid decomposition process in the pretreatment process, and because the ICP plasma is in the atmosphere, background components contained in the atmosphere (e.g., N_2, O_2, CO_2, etc.) cannot be removed. However, quantitative analysis of metal elements in the sample is possible, and although organic elements cannot be identified, they can be quantified as influences from sources other than metals. The pretreatment method was to weigh the sample powder, add aqua regia 8 ml, and heat the sample solution to 230 °C for 20 min using a microwave device (Milestone: Start SYNTH Microwave Synthesis Labstation) to promote decomposition, and then continue heating at 230 °C for another 20 min. The volume was then adjusted to a constant value using a 50 ml measuring flask and diluted 200 times with water. In addition, three types of diluted solutions were prepared for each solution to take into account dilution errors, and the average value was taken.

Vanadium powder and nickel powder were pretreated with aqua regia to prepare solutions, which were then introduced into the device. Because aqua regia is used, sample pretreatment must be performed in the air, and each sample is exposed to air for a short period of time.

The major elements V and Ni were measured three times using samples of approximately 10 mg each from each powder. Trace metal elements were measured three times using samples of approximately 200 mg each from each powder. The measurement error was calculated as the standard deviation from 2 or 3 measurements.

C.3 Infrared absorption method

When analyzing metal powders for oxygen content, the sample must be placed in the analyzer and not released into the air. Since special analytical equipment is required for light element analysis under such non-exposure to the atmosphere, quantitative analysis was performed using an inert gas fusion-non-dispersive infrared analyzer (EMGA-930) of Horiba Techno Service Co., Ltd. The measurement principle of the non-dispersive infrared absorption (NDIR) is that when the molecule to be measured is exposed to infrared rays, it is excited by light of a wavelength corresponding to its inherent vibration and absorbs the light of corresponding wavelength. This means that infrared rays are absorbed only when the molecular dipole moment changes due to the vibration or rotation of the molecule. The components are determined by the position of the absorption band of these molecules, and concentration is measured by measuring the absorption strength of the molecule's inherent infrared spectral line. There are two types of infrared analyzers: dispersive and non-dispersive. The non-dispersive type is further divided into negative filter and positive filter types. The mainly used positive filter detector acts as a filter (wavelength selection device) to detect only specific gas components at the same time as detection. It absorbs only the coupling line of the wavelength specific to the gas to be detected, causing a temperature rise, and the concentration is calculated by measuring this change. Figure C.2 shows an analytical device using EMGA-930. In this device, helium gas is used as a carrier gas, the sample is heated and melted in a graphite crucible, and the oxygen contained in the sample reacts with the carbon in the graphite crucible and is extracted as carbon monoxide. When the oxygen concentration is high, it is detected by a NDIR Non-Dispersive Infrared Detector for carbon monoxide. When the oxygen concentration is low, the extracted carbon monoxide is passed through an oxidizer (copper oxide) to convert it to carbon dioxide and then detected by an NDIR for carbon dioxide. Hydrogen in the sample is extracted as hydrogen, and then passed through an oxidizer to be detected by an NDIR for H_2O. After that, if nitrogen is to be measured, but not used in the analysis, a TCD (Thermal Conductivity Detector) is used.

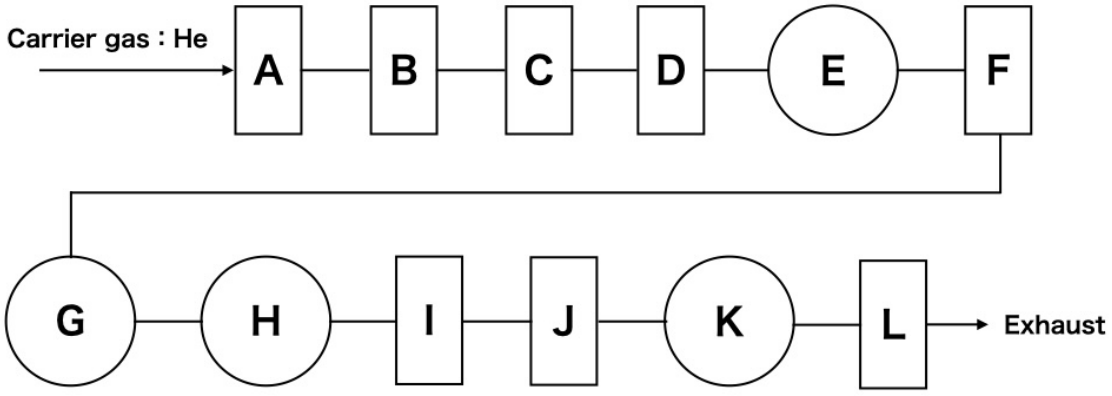

Figure C.2: Diagram of EMGA-930 system for determination of oxygen and hydrogen in the sample powder. A: Carrier gas purifier, B: Extraction funace & graphite crucible, C: Dust filter, D: Flow rate controller, E: NDIR detector CO, F: Oxidizing decaburizer(Copper oxide), G: NDIR detector CO_2 and H_2, H: NDIR detector for H_2O, I: Decarurizer, J: Dehydractor, K: Detector for N_2, L: Flow mator

Bibliography

[1] S. Dimopoulos and A. A. Geraci, "Probing submicron forces by interferometry of bose-einstein condensed atoms," *Phys. Rev. D*, vol. 68, p. 124021, Dec (2003).

[2] B. A. Dobrescu and I. Mocioiu, "Spin-dependent macroscopic forces from new particle exchange," *Journal of High Energy Physics*, vol. 2006, p. 005, nov 2006.

[3] N. Sugimoto, "Aichi-sr wide-angle and small-scale x-ray scattering experiment beamline bl8s3," in *Research Group on Evaluation Technology Development Using Small-Angle X-ray Scattering*, (Science and Technology Collaboration Foundation Research Collaboration Center, Japan), 2017. in Japanese.

[4] A. Allen, F. Zhang, R. Kline, W. Guthrie, and J. Ilavsky, "Nist standard reference material 3600: Absolute intensity calibration standard for small-angle x-ray scattering," 2017-04-01 2017.

[5] H. Photonics, *Flat panel type multianode PMT assembly, H12700Series/H14220 Series(V)*, (2019).

[6] S. Matsumoto, "Verification of the inverse square law of gravity on the nanometer scale using low-energy neutron scattering," Master's thesis, Kyushu University, (2013).

[7] R. Nakabe, "Optimization of experimental setup for exploring unknown short-range forces using coherent neutron scattering," Master's thesis, Nagoya University, (2020).

[8] E. Tiesinga, P. J. Mohr, D. B. Newell, and B. N. Taylor, "Codata recommended values of the fundamental physical constants: 2018," *Rev. Mod. Phys.*, vol. 93, p. 025010, Jun 2021.

[9] A. Alexandru and F. Lee, "Neutron electric polarizability," 11 2009.

[10] "Pilatus 2m detector system." `https://media.dectris.com/Technical_Specification_PILATUS_2M_V1_7.pdf`.

[11] K. Mishima, "J-parc neutron fundamental physics beamline bl05/nop ," *Ripples*, vol. 25, no. 2, pp. 156–160, (2015).

[12] G. Aad, "Observation of a new particle in the search for the standard model higgs boson with the atlas detector at the lhc," *Physics Letters B*, vol. 716, no. 1, pp. 1–29, 2012.

[13] B. P. Abbott and Abbott, "Observation of gravitational waves from a binary black hole merger," *Phys. Rev. Lett.*, vol. 116, p. 061102, Feb 2016.

[14] V. Khachatryan, "Search for new physics in final states with two opposite-sign, same-flavor leptons, jets, and missing transverse momentum in pp collisions at $\sqrt{s} = 13\,\mathrm{TeV}$," *Journal of High Energy Physics*, vol. 2016, Dec. 2016.

[15] M. Bordag, U. Mohideen, and V. Mostepanenko, "New developments in the casimir effect," *Physics Reports*, vol. 353, p. 1–205, Oct. 2001.

[16] J. Jaeckel and A. Ringwald, "The low-energy frontier of particle physics," *Annual Review of Nuclear and Particle Science*, vol. 60, no. Volume 60, 2010, pp. 405–437, 2010.

[17] E. Adelberger *et al.*, "Torsion balance experiments: A low-energy frontier of particle physics," *Progress in Particle and Nuclear Physics*, vol. 62, no. 1, pp. 102–134, 2009.

[18] B. P. Abbott *et al.*, "Gravitational waves and gamma-rays from a binary neutron star merger: Gw170817 and grb 170817a," *The Astrophysical Journal Letters*, vol. 848, p. L13, oct 2017.

[19] A. Frank, P. Van Isacker, and J. Gómez-Camacho, "Probing additional dimensions in the universe with neutron experiments," *Physics Letters B*, vol. 582, p. 15–20, Feb. 2004.

[20] T. Shima *GenshikakuKenkyu*, vol. 49, p. 51.

[21] V. V. Nesvizhevsky, G. Pignol, and K. V. Protasov, "Neutron scattering and extra-short-range interactions," *Phys. Rev. D*, vol. 77, p. 034020, Feb 2008.

[22] H. Yan and W. M. Snow, "New limit on possible long-range parity-odd interactions of the neutron from neutron-spin rotation in liquid ^{4}He," *Phys. Rev. Lett.*, vol. 110, p. 082003, Feb 2013.

[23] B. Heacock, T. Fujiie, R. W. Haun, A. Henins, K. Hirota, T. Hosobata, M. G. Huber, M. Kitaguchi, D. A. Pushin, H. Shimizu, M. Takeda, R. Valdillez, Y. Yamagata, and A. R. Young, "Pendellösung interferometry probes the neutron charge radius, lattice dynamics, and fifth forces," *Science*, vol. 373, 9 2021.

[24] C. C. Haddock, N. Oi, K. Hirota, T. Ino, M. Kitaguchi, S. Matsumoto, K. Mishima, T. Shima, H. M. Shimizu, W. M. Snow, and T. Yoshioka, "Search for deviations from the inverse square law of gravity at nm range using a pulsed neutron beam," *Phys. Rev. D*, vol. 97, p. 062002, Mar 2018.

[25] Y. Kamiya, K. Itagaki, M. Tani, G. N. Kim, and S. Komamiya, "Constraints on new gravitylike forces in the nanometer range," *Phys. Rev. Lett.*, vol. 114, p. 161101, Apr 2015.

[26] N. Arkani–Hamed, S. Dimopoulos, and G. Dvali, "The hierarchy problem and new dimensions at a millimeter," *Physics Letters B*, vol. 429, no. 3, pp. 263–272, 1998.

[27] M. S. Safronova, D. Budker, D. DeMille, D. F. J. Kimball, A. Derevianko, and C. W. Clark, "Search for new physics with atoms and molecules," *Rev. Mod. Phys.*, vol. 90, p. 025008, Jun 2018.

[28] C. Talmadge, J. P. Berthias, R. W. Hellings, and E. M. Standish, "Model-independent constraints on possible modifications of newtonian gravity," *Phys. Rev. Lett.*, vol. 61, pp. 1159–1162, Sep 1988.

[29] Y. Fujii, "Dilaton and possible non-newtonian gravity," *Nature*, vol. 234, pp. 5–7, 1971.

[30] E. Fischbach, D. Sudarsky, A. Szafer, C. Talmadge, and S. H. Aronson, "Reanalysis of the eoumltvös experiment," *Phys. Rev. Lett.*, vol. 56, pp. 3–6, Jan 1986.

[31] N. Arkani-Hamed, S. Dimopoulos, and G. Dvali, "Phenomenology, astrophysics, and cosmology of theories with submillimeter dimensions and tev scale quantum gravity," *Phys. Rev. D*, vol. 59, p. 086004, Mar (1999).

[32] S. Dimopoulos and A. A. Geraci, "Probing submicron forces by interferometry of bose-einstein condensed atoms," *Phys. Rev. D*, vol. 68, p. 124021, Dec 2003.

[33] Z. Bogorad, P. W. Graham, and G. Gratta, "Detecting nanometer-scale new forces with coherent neutron scattering," *Phys. Rev. D*, vol. 108, p. 055005, Sep 2023.

[34] Japan Society for the Promotion of Science, "Exploring unknown interactions through neutron and nanoparticle scattering (KAKENHI Grant Number JP19H01927)." `https://researchmap.jp/led0141215/research_projects/35618260`, 2019. Accessed: 2025-04-13.

[35] T. Okuchi, A. Hoshikawa, and T. Ishigaki, "Forge-hardened tizr null-matrix alloy for neutron scattering under extreme conditions," *Metals*, vol. 5, no. 4, pp. 2340–2350, 2015.

[36] J. H. Smith, E. R. Vance, and D. A. Wheeler, "A null-matrix alloy for neutron diffraction," *Journal of Physics E: Scientific Instruments*, vol. 1, p. 945, sep 1968.

[37] M. He, C. Wang, H. Yang, D.-Y. Wu, J.-J. Lee, F. Wang, M. Avdeev, and W. H. Kan, "A family of v-based null matrix alloys with atomic and mesoscopic homogeneity," *ACS Applied Engineering Materials*, vol. 2, no. 10, pp. 2468–2477, 2024.

[38] W. Bauspiess, U. Bonse, and H. Rauch, "The prototype neutron interferometer at the grenoble high flux reactor," *Nuclear Instruments and Methods*, vol. 157, no. 3, pp. 495–506, 1978.

[39] T. Fujiie, M. Hino, T. Hosobata, G. Ichikawa, M. Kitaguchi, K. Mishima, Y. Seki, H. M. Shimizu, and Y. Yamagata, "Development of neutron interferometer using multilayer mirrors and measurements of neutron-nuclear scattering length with pulsed neutron source," *Phys. Rev. Lett.*, vol. 132, p. 023402, Jan 2024.

[40] Y. P. Vinichenko and E. N. Sidorova, "Synthesis and characterization of nickel hydroxide nanoparticles obtained by chemical deposition method under different precipitation conditions," *Journal of Physics: Conference Series*, vol. 741, p. 012194, aug 2016.

[41] H. Yui, "Bragg peak evaluation of vanadium alloys for neutron scattering experiments," tech. rep., J-PARC/MLF/i-MATERIA/BL20, 2015. Accessed: 2015-05-25.

[42] F. Maekawa *et al.*, "First neutron production utilizing j-parc pulsed spallation neutron source jsns and neutronic performance demonstrated," *Nuclear Instruments and Methods in Physics Research Section A: Accelerators, Spectrometers, Detectors and Associated Equipment*, vol. 620, no. 2, pp. 159–165, (2010).

[43] K. Mishima *et al.*, "Design of neutron beamline for fundamental physics at j-parc bl05," *Nuclear Instruments and Methods in Physics Research Section A: Accelerators, Spectrometers, Detectors and Associated Equipment*, vol. 600, no. 1, pp. 342–345, (2009).

[44] Y. Arimoto *et al.*, "Present status of neutron fundamental physics at J-PARC," *Progress of Theoretical and Experimental Physics*, vol. (2012), p. 02B007, 12 2012.

[45] "Data sheet of a3100." `http://www.riversidetnt.com/Spec_A3100_20071231.pdf`.

[46] *Photomultiplier tubes their fundamentals and applications.* Hamamatsu Photonics Co., Ltd., (2017).

[47] K. Hirota, T. Shinohara, K. Ikeda, K. Mishima, T. Adachi, T. Morishima, S. Satoh, T. Oku, S. Yamada, H. Sasao, J.-i. Suzuki, and H. M. Shimizu, "Development of a neutron detector based on a position-sensitive photomultiplier," *Phys. Chem. Chem. Phys.*, vol. 7, pp. 1836–1838, (2005).

[48] F. Nemoto, N. L. Yamada, and S. Satoh, "Performance of position-sensitive flat-panel and resister type photomultiplier tube detector on neutron reflectometer sofia at j-parc," *Nuclear Instruments and Methods in Physics Research Section A: Accelerators, Spectrometers, Detectors and Associated Equipment*, vol. 1040, p. 166988, 2022.

[49] M. Kotlarchyk and S. Chen, "Analysis of small angle neutron scattering spectra from polydisperse interacting colloids," *The Journal of Chemical Physics*, vol. 79, pp. 2461–2469, 09 1983.

[50] J. K. Percus and G. J. Yevick, "Analysis of classical statistical mechanics by means of collective coordinates," *Phys. Rev.*, vol. 110, pp. 1–13, Apr 1958.

[51] D. J. Kinning and E. L. Thomas, "Hard-sphere interactions between spherical domains in diblock copolymers," *Macromolecules*, vol. 17, pp. 1712–1718, 09 1984.

[52] K. Mishima, "Neutron scattering cross section of diamond nanoparticle," *EPJ Web of Conferences*, vol. 219, pp. 10005–10005, 11 2018.

[53] H. E. Fischer, J. M. Simonson, J. C. Neuefeind, H. Lemmel, H. Rauch, A. Zeidler, and P. S. Salmon, "The bound coherent neutron scattering lengths of the oxygen isotopes," *Journal of Physics: Condensed Matter*, vol. 24, p. 505105, nov 2012.

[54] N. Arkani-Hamed and S. Dimopoulos, "New origin for approximate symmetries from distant breaking in extra dimensions," *Phys. Rev. D*, vol. 65, p. 052003, Jan (2002).

[55] T. KALUZA, "On the unification problem in physics," *International Journal of Modern Physics D*, vol. 27, p. 1870001, Oct. (2018).

[56] O. Klein *Zeitschrift für Physik*, vol. 37, pp. 895–906, Oct. (1926).

[57] G. L. Squires and J. W. Lynn, "Introduction to the theory of thermal neutron scattering," *Physics Today*, vol. 32, 10 1979.

[58] A. T. Boothroyd, *Principles of Neutron Scattering from Condensed Matter*. Oxford University Press, 07 2020.

[59] C. J. Glinka, "Incoherent neutron scattering from multi-element materials," *Journal of Applied Crystallography*, vol. 44, pp. 618–624, Jun 2011.

[60] J. Murata and S. Tanaka, "A review of short-range gravity experiments in the LHC era," *Class. Quant. Grav.*, vol. 32, no. 3, p. 033001, 2015.

[61] M. S. Safronova, D. Budker, D. DeMille, D. F. J. Kimball, A. Derevianko, and C. W. Clark, "Search for new physics with atoms and molecules," *Rev. Mod. Phys.*, vol. 90, p. 025008, Jun 2018.

[62] J.P.Cotton, *Neutron, X-ray and Light Scattering: Introduction to an Investigative Tool for Colloidal and Polymeric Systems*, pp. 29–30. Amsterdam:North Holland., p.lindner, t.zemb ed., (1991).

[63] H. Kunieda, Y. Takashima, T. Okajima, and Y. Takeda, "10 years of aichi synchrotron radiation center impact on industrial and academic research and developments," *Journal of Physics: Conference Series*, vol. 2380, p. 012001, dec 2022.

[64] O. Toshihiro, T. Yoshikazu, and K. Hideyo, "Aichisr: A decade of advanced research and innovation in industry and academia," *Synchrotron Radiation News*, vol. 37, no. 2, pp. 30–35, 2024.

[65] "Technical details, materials and life science experimental facility."

[66] S. Satoh, "Development of an frp system which is a two-dimensional position-sensitive neutron detector," *hamon*, vol. 27, pp. 8–11, 01 2017.